Physical properties of low-dimensional sp^2-based carbon nanostructures

V. Meunier[*]

Department of Physics, Applied Physics, and Astronomy, Rensselaer Polytechnic Institute, Troy, New York 12180, USA

A. G. Souza Filho[†] and E. B. Barros[‡]

Departamento de Física, Universidade Federal do Ceará, 60455-900 Fortaleza, Ceará, Brazil

M. S. Dresselhaus[§]

Departments of Physics and Electrical Engineering & Computer Science, Massachusetts Institute of Technology, Cambridge, Massachusetts 02139, USA

(published 24 May 2016)

The last two decades have witnessed a tremendous growth in the development and understanding of sp^2 carbon-based nanostructures. The impact of this research has led to a number of fundamental discoveries that have played a central role in the understanding of many aspects of materials physics and their applications. Much of this progress has been enabled by the development of new techniques to prepare, modify, and assemble low-dimensional materials into devices. The field has also benefited greatly from much progress in theoretical and computational modeling, as well as from advances in characterization techniques developed to probe and manipulate single atomic layers, nanoribbons, and nanotubes. Some of the most fundamental physical properties of sp^2 carbon-based nanostructures are reviewed and their role as model systems for solid-state physics in one and two dimensions is highlighted. The objective of this review is to provide a thorough account on current understanding of how the details of the atomic structure affect phonons, electrons, and transport in these nanomaterials. The review starts with a description of the behavior of single-layer and few-layer graphene and then expands into the analysis of nanoribbons and nanotubes in terms of their reduced dimensionality and curvature. How the properties can be modified and tailored for specific applications is then discussed. The review concludes with a historical perspective and considers some open questions concerning future directions in the physics of low-dimensional systems and their impact on continued advances in solid-state physics, and also looks beyond carbon nanosystems.

DOI: 10.1103/RevModPhys.88.025005

CONTENTS

[*]meuniv@rpi.edu
[†]agsf@fisica.ufc.br
[‡]ebarros@fisica.ufc.br
[§]millie@mgm.mit.edu

I. INTRODUCTION

Low-dimensional sp^2-based nanocarbons exhibit remarkable properties so that they have been playing a major role in materials science from many different perspectives. In particular, nanocarbons have been very attractive to physicists in the last two decades as fertile ground for the manifestation of novel fundamental physics phenomena. The resulting unique physical properties make nanocarbons ideal building blocks for future nanoscience and nanotechnology development. However, this review will focus more on the physical properties of this class of materials rather than on their applications.

The marvelous world of sp^2 nanocarbon materials comes from the special features presented by carbon, the sixth element of the periodic table. Carbon is one of the most abundant elements in nature and has a special place in the periodic table with six electrons distributed among the atomic orbitals as $1s^2 2s^2 2p^2$. The $1s^2$ electrons are strongly bonded to the nucleus (binding energy of -284 eV), and the interaction with the external world, including their chemical bonding, is made by the remaining four valence electrons. The valence electrons allow carbon in principle to thus present any of the sp^n ($n = 1, 2, 3$) hybridization states. This versatility comes from the combination of some special features of carbon. First, the atomic number of C is such that the energy separation between the s and p orbitals is neither too low nor too high for many important properties and potential applications. Second, the number of electrons is exactly the same as the number of orbitals, such that each electron can occupy one of the four available $s-p$ hybrid orbitals. If we consider boron (nitrogen) for comparison, the $s-p$ energy splitting is lower (larger) than carbon, but the atom has a lower (higher) number of electrons in its outer shell and the chemistry is not as rich as that of carbon due to this lack (or excess) of electrons for filling the hybrid orbitals. Another advantage of carbon compared to other elements which also have four valence electrons is the absence of p electrons in the core; this confers a small atomic radius to carbon, thereby allowing carbon to form very short bonds and a very stable planar structure, such as in graphene, where the carbon atoms have a typical sp^2 hybridization.

Graphene is usually considered as the starting point for discussing other sp^2 nanocarbons, such as carbon nanoribbons and nanotubes. When limiting the graphene sheet to one thin layer, a nanoribbon can be considered as a narrow strip of graphene, where the length is much larger than the width. In addition to the graphene width, the other degree of freedom to be exploited in the graphene nanoribbon (GNR) is the atomic arrangement of the edges, which can be zigzag or armchair for the most symmetrical cases, or a mixture of the two arrangements. By adding curvature to a given ribbon, carbon nanotubes (CNTs) with different (n, m) chiralities can be obtained.

In spite of this logical sequence in conceptually obtaining one-dimensional carbon nanostructures using graphene as the mother structure, carbon nanoscience historically was not developed according to that time line. From the experimental point of view, tubular carbon nanostructures came to the scene first, before flat atomically thin nanostructures. For many practitioners working in the field today, the pioneering theoretical work of Wallace on the electronic band structure of graphene published 70 years ago had a great influence on later scientific developments made on the understanding of graphite and graphite compounds (Wallace, 1947). Another happening with high impact was the organization of the first conference on carbon intercalation compounds held in a castle in La Napoule, France in 1977. This conference brought together for the first time for intense discussion a group of researchers working on this topic. Many of the early developments in the field were summarized in the conference proceedings (Vogel and Herold, 1977) and in a review article on graphite intercalation compounds published in 1981 to help researchers learn about this new research field (Dresselhaus and Dresselhaus, 1981). Later a textbook on carbon fibers (Dresselhaus *et al.*, 1988) was published for students' use. These historical events played a key role in the development of the carbon research that ensued, with the work on carbon nanotubes (Iijima, 1991; Iijima and Ichihashi, 1993; Saito, Dresselhaus, and Dresselhaus, 1998), nanoribbons (Fujita *et al.*, 1996; Nakada *et al.*, 1996), and graphene itself (Novoselov *et al.*, 2004; Geim and Novoselov, 2007; Castro Neto *et al.*, 2009; Katsnelson, 2012).

Many experimental results on nanocarbons soon were interpreted as having graphene as the conceptual basis. By the time carbon nanotube science had become a mature field, graphene had entered the scene as the first two-dimensional nanomaterial to be studied in many laboratories worldwide using different techniques.

Carbon nanostructures have many striking properties coming from carbon sp^2 hybridization and they have become prototype systems for nanoscience and nanotechnology for the following reasons: First, sp^2-hybridized carbon structures are also incredibly small, at least in one dimension (graphene is one atom thick and single-wall carbon nanotubes have diameters of about 1 nm), thus presenting strong quantum confinement effects, which dictate many physical properties not observed in larger systems. Second, the sp^2 bond is the strongest bond in nature thus endowing these systems with unusual mechanical properties, which combine mechanical flexibility and mechanical strength at the same time. Third, it is also unique that these systems have a large exposed surface area, but yet no dangling bonds, thereby making these materials very stable. Fourth, the charge carriers are delocalized π electrons that come from the p_z orbitals and these π electrons are responsible for the unusual electronic and thermal transport properties of these systems. Finally, the simplicity of the structure of these nanomaterials is unique

because they are formed just by one type of chemical element (with few electrons) and the atoms are arranged in a very simple honeycomb hexagonal lattice. It follows that these systems are relatively easy to model, manipulate, and measure in the laboratory. In fact, sp^2-based nanocarbons have provided numerous examples of model systems where theoretical predictions have been made before the experiments were done.

Because of their reduced dimensions, a large portion of the surface area of nanocarbon materials is exposed to the environment, which makes them particularly sensitive to interfacial and environmental effects. This leads to important changes in their intrinsic vibrational, electronic, and optical properties which are determined by macroscopically controlled parameters, such as the material composing the substrate on which the nanocarbon is deposited or the medium on which the nanocarbon is dispersed. Moreover, interface effects are not the only way to control the properties of sp^2 nanocarbons; their small size and the consequent quantum confinement effects make these materials strongly sensitive to departures from their idealized structures. This sensitivity can be exploited to modify and tailor the nanomaterial properties for different practical applications.

In this review article we discuss some fundamental aspects of graphene, graphene nanoribbons, and carbon nanotubes, focusing on the latest developments in advancing our understanding of how dimensionality, curvature, and symmetry in these systems dictate some of their physical properties. Furthermore, we review some of the different ways by which these unique properties can be controllably modified, leading to additional interesting behaviors and prospective technological applications than those of simple graphene. This review is organized as follows. In Sec. II the basic concepts of the fundamental solid-state properties of sp^2-based carbons are presented. This section gives an overview of the properties of sp^2 nanocarbons as stemming from the unique properties of graphene. Section III reviews how the electronic, optical, and vibrational properties of sp^2-based carbon nanostructures are expressed when nanocarbons are placed on various interfaces where the environment plays an important role, with special attention given to lattice vibration (phonons) and to spacial electron excitations (excitons). In Sec. IV emphasis is given to the possible ways of engineering the properties of the sp^2 carbon nanostructures by controlling strain, atomic edges, curvature, and layer stacking. We then discuss the transport properties of sp^2 nanocarbons in Sec. V. These have been widely exploited for practical devices and have been proposed for different technological applications. In Sec. VI, we show the latest developments in studying the interaction between sp^2 and sp nanocarbon systems, such as carbon chains inside carbon nanotubes. Finally, in Sec. VII we present our vision and perspectives for the future of the nanocarbon field, regarding both the research opportunities and the challenges to be faced.

II. BASICS

In this section, we describe the fundamental properties of the ideal structure of nanocarbons: graphene, carbon nanotubes, and graphene nanoribbons. This presentation highlights the similarities and differences between these nanostructures, using dimensionality, curvature, and symmetry arguments, including a presentation of the electronic, vibrational, and electron-phonon properties of these nanocarbons. The use of spectroscopy for investigating these nanomaterials is also emphasized.

A. Structural and symmetry properties

The basic structure of the sp^2 nanocarbons considered in this review article can be derived from the honeycomb lattice of pristine graphene [see Fig. 1(a)], which is characterized by the two lattice vectors

$$\mathbf{a}_1 = \frac{a}{2}(\sqrt{3}, 1), \qquad \mathbf{a}_2 = \frac{a}{2}(\sqrt{3}, -1), \tag{1}$$

where $a = \sqrt{3}a_{cc} = 0.246$ nm is the graphene lattice parameter, with $a_{cc} = 0.142$ nm being the nearest-neighbor carbon-carbon distance. The reciprocal lattice of graphene is described in terms of the reciprocal lattice vectors

$$\mathbf{b}_1 = \frac{2\pi}{\sqrt{3}a}(1, \sqrt{3}), \qquad \mathbf{b}_2 = \frac{2\pi}{\sqrt{3}a}(1, -\sqrt{3}). \tag{2}$$

The reciprocal lattice of graphene is shown in Fig. 1(b) where the first Brillouin zone (BZ) is depicted in gray. Special notice should be taken of the regions near the high symmetry points Γ and K in reciprocal space. There are two inequivalent K points in the Brillouin zone (K and K') of Fig. 1(b), which give rise to a valley degeneracy characteristic of 2D hexagonal lattices, such as graphene, hexagonal boron nitride (h-BN), MoS_2, and other hexagonal 2D materials.

Figure 2 depicts how the structure of graphene nanoribbons and carbon nanotubes can be described in terms of the structure of 2D graphene. The structure of a graphene nanoribbon can be defined by slicing the graphene honeycomb structure along a specific direction. Depending on the chosen direction, the nanoribbon can have either a zigzag edge, an armchair edge, or a chiral edge. The structure of a carbon nanotube can then be described by rolling up a specific nanoribbon along its shortest direction to form a seamless cylindrical shape. It is important to note that when an armchair-edged nanoribbon is rolled up, the resulting

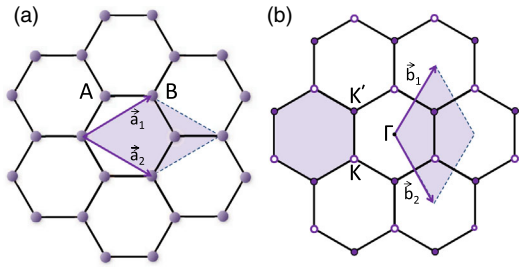

FIG. 1. Graphene (a) real space and (b) reciprocal space lattices. The unit cells in real space and reciprocal space are highlighted, and the unit vectors in real space and reciprocal space are indicated.

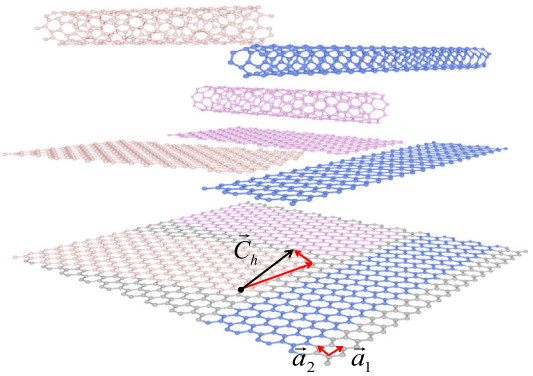

FIG. 2. Structural models for three carbon nanotubes (top), three graphene nanoribbons (middle), compared to their mother structure graphene (bottom). The chiral vector $\mathbf{C}_h$ and in-plane vectors $\mathbf{a}_1$, $\mathbf{a}_2$ are shown.

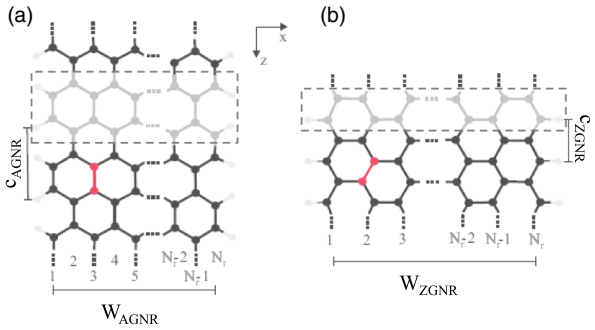

FIG. 3. Structures of (a) a N-AGNR and (b) a N-ZGNR. In each case, one dimer is highlighted. The unit cells are emphasized by a gray box. W_{AGNR} and W_{ZGNR} are the armchair and zigzag nanoribbon widths, respectively, while c_{AGNR} and c_{ZGNR} show the length of the translational vectors for the ribbon unit cells. Adapted from Gillen *et al.*, 2009.

nanotube has a zigzag cross section, whereas the rolling up of a zigzag-edged ribbon leads to an armchair nanotube.

The structures of carbon nanotubes can be uniquely defined by the chiral vector $\mathbf{C}_h = n\mathbf{a}_1 + m\mathbf{a}_2$, with n and m being integers. $\mathbf{C}_h$ is, for example, most often written as $(n, m) = (5, 4)$, where it is understood that the basis $\mathbf{a}_1$, $\mathbf{a}_2$ is employed. When neglecting curvature effects on the C–C bond lengths and angles, the carbon nanotube diameter d_t and chiral angle θ (defined as the angle between $\mathbf{C}_h$ and $\mathbf{a}_2$) are both uniquely determined by (n, m) and are given by

$$d_t = \frac{a}{\pi}\sqrt{n^2 + nm + m^2}, \qquad \theta = \tan^{-1}\left(\frac{\sqrt{3}m}{2n+m}\right), \quad (3)$$

in which a is the graphene lattice parameter. For zigzag nanotubes $m = 0$, while armchair carbon nanotubes are characterized by $m = n$.

Chiral graphene nanoribbons cannot be uniquely defined due to the freedom in choosing the particular shapes of the edges. Different approaches have been used to specify the structure of particular classes of ribbons. For instance, Ezawa proposed an approach using a (p, q) classification similar to that used for carbon nanotubes and which is appropriate for armchair, zigzag, and some mixed-edge nanoribbons (Ezawa, 2007). Alternatively, one can classify the armchair- and zigzag-edged nanoribbons either by the number of honeycombs along the ribbon width W_r (Yamada, Yamakita, and Ohno, 2008) or by their edge type into armchair GNR (AGNR) or zigzag GNR (ZGNR) and giving the number of dimers N_r in the unit cell; see Fig. 3 (Fujita *et al.*, 1996; Gillen *et al.*, 2009). It is important to note that not all possible zigzag- or armchair-edged nanoribbons can be wrapped up to form achiral carbon nanotubes. For instance, only even N_r armchair-edged nanoribbons can be wrapped up to form a $(n, 0)$ zigzag nanotube with $N_r = 2n + 2$. On the other hand, for zigzag-edged ribbons, only the structures with N_r odd can correspond to an (n, n) armchair carbon nanotube $(N_r = 2n + 1)$. The width of the achiral nanoribbons W_r can be obtained in terms of N_r as

$$W_r = \tfrac{1}{2}(N_r - 1)a, \quad \text{armchair nanoribbons}, \quad (4)$$

$$W_r = \frac{\sqrt{3}}{2}(N_r - 1)a, \quad \text{zigzag nanoribbons}. \quad (5)$$

In terms of symmetry, graphene belongs to the $p6/mmm$ space group with a D_{6h} point group (Malard, Guimarães *et al.*, 2009). When the graphene structure is sliced up to form graphene nanoribbons, some of the point group symmetries are removed, thus reducing the symmetry either to the $Pmma$ nonsymmorphic space group for armchair (zigzag) ribbons with even (odd) N_r or to the $Pmmm$ symmorphic space group for odd N_r armchair (even N_r zigzag) ribbons. Both the $Pmma$ and $Pmmm$ space groups are homomorphic to the D_{2h} point group.

For carbon nanotubes, the graphene translational symmetry is partially restored in terms of rototranslations of the nanotube (White, Robertson, and Mintmire, 1993), which make the nanotubes highly symmetric. The symmetry properties of carbon nanotubes are better described in terms of line groups (Damnjanovic *et al.*, 1999). However, it has been shown that the space group of a chiral (n, m) nanotube is homomorphic to a D_{N_t} point group, with $N_t = 2(n^2 + nm + m^2)/d_R$ being the number of hexagons contained in the nanotube unit cell. Here d_R is the greatest common divisor of $2n + m$ and $2m + n$. For achiral $(n, 0)$ and (n, n) nanotubes, the space group is homomorphic to the D_{2nh} point group (Barros *et al.*, 2006).

B. Electronic properties

Although the systematic experimental study of graphene started only after the seminal work of Novoselov *et al.* (2004), the theoretical properties of graphene have been studied for more than 50 years as a basis for understanding the properties of graphite (Wallace, 1947) and other types of sp^2 carbons, such as carbon nanotubes (Mintmire and White, 1998; Saito, Dresselhaus, and Dresselhaus, 1998).

The electronic properties of graphene can be well described in terms of a simple, nonorthogonal tight-binding model considering only the interaction between the nearest-neighbor π (p_z) orbitals. Within this simple model, the energy of the electronic bands of graphene can be written as

$$E_{c,v}(\mathbf{k}) = \frac{\epsilon \pm tw(\mathbf{k})}{1 \pm sw(\mathbf{k})}, \tag{6}$$

with ϵ the orbital energy, t the hopping parameter, s the overlap parameter described below, and

$$w(\mathbf{k}) = |f(\mathbf{k})| = \sqrt{1 + 4\cos\frac{\sqrt{3}k_x a}{2}\cos\frac{k_y a}{2} + 4\cos^2\frac{k_y a}{2}}, \tag{7}$$

in which the function $f(\mathbf{k})$ is written compactly to show its real and imaginary components as

$$f(\mathbf{k}) = \exp\left(i\frac{k_x a}{\sqrt{3}}\right) + \exp\left(-i\frac{k_x a}{2\sqrt{3}} + i\frac{k_y a}{2}\right) + \exp\left(-i\frac{k_x a}{2\sqrt{3}} - i\frac{k_y a}{2}\right), \tag{8}$$

where i is the unit imaginary element.

The $+$ and $-$ signs in Eq. (6) correspond, respectively, to the conduction (c) and valence (v) bands. The zero of energy is usually chosen to be $\epsilon = 0$ as in Fig. 4(b) so that, in this model, the Fermi energy is set at zero. The t and s parameters have been obtained by fitting *ab initio* calculated band structures, leading to values on the order of $t = -3.033$ eV and $s = 0.129$ (Saito, Dresselhaus, and Dresselhaus, 1998). This nearest-neighbor-only approximation successfully captures the main qualitative features of the graphene band structure. A number of other more quantitatively accurate methods based on the tight-binding approximation have been developed, including, for instance, the introduction of a $\sigma - \pi$ Hamiltonian basis (Foa Torres, Roche, and Charlier, 2014) or the inclusion of a third-nearest-neighbor interaction term (Reich *et al.*, 2002; White *et al.*, 2007). The tight-binding approximation has been very broadly used in the literature devoted to carbon nanosystems and, in spite of the availability of supercomputers able to routinely use *ab initio* methods, the tight-binding approximation remains a method of choice that still enjoys a constant stream of new developments for the study of the electronic properties of carbon nanosystems and devices (Liu *et al.*, 2015).

The calculated band structure of graphene is shown in Fig. 4(a) using an orthogonal tight-binding model. It should be noted that close to the two K points, at the edges of the Brillouin zone, the band structure for monolayer graphene takes on the shape of two cones (known as Dirac cones) intersecting precisely at the K or K' point. The presence of these two nonequivalent Dirac cones gives rise to most of the interesting electronic properties of graphene and, consequently, of the other sp^2-based nanocarbons.

A plot of the density of electronic states is shown in Fig. 4(b). It is important to note that near the Fermi energy E_F the density of states vanishes, which characterizes graphene as a zero-gap semiconductor or a semimetal since, in spite of the fact that graphene is *gapless*, monolayer graphene should formally have a zero conductance at charge neutrality and for temperature $T \to 0$. The linear dependence of the electrical conductivity on the gate voltage with vanishing conductivity

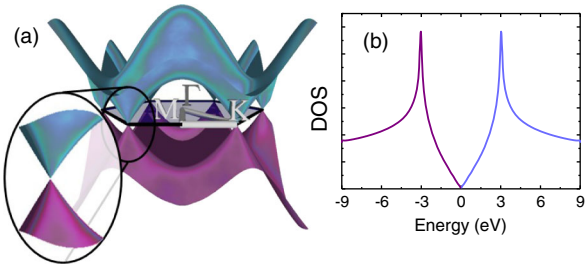

FIG. 4. (a) Electronic band structure calculated using an orthogonal tight-binding model and considering only nearest-neighbor atom interactions. The inset on the lower left highlights the conical energy band dispersion near the Fermi energy. (b) The corresponding energy dependence of the electronic density of states (DOS). For a neutral graphene sample, the Fermi level E_F is located at the Dirac point corresponding to zero energy. From Saito *et al.*, 1992.

at charge neutrality, together with the half-integer quantum Hall effect, are among the characteristic experimental properties of graphene (Novoselov *et al.*, 2004; Zhang *et al.*, 2005; Castro Neto *et al.*, 2009) and these properties have also recently been observed in graphene superlattices by the Columbia group (Wang *et al.*, 2015).

For carbon nanotubes and graphene nanoribbons, the electronic properties can be obtained to a first approximation by taking the graphene electronic structure expressed in single-orbital tight-binding form and imposing proper boundary conditions, as explained below (Saito *et al.*, 1992). For instance, the electronic energy bands of carbon nanotubes, disregarding curvature effects, can be described by enforcing a periodic boundary condition along the nanotube circumferential direction. This boundary condition implies that the electron wave vector in this direction is quantized into integer values of $2/d_t$. This approach is known as the zone-folding scheme (Saito *et al.*, 1992). Graphically, the zone-folding scheme can be understood in terms of cutting lines which slice through the electronic bands of graphene. Each of these lines cuts through both the valence and the conduction bands of graphene, giving rise to two sets (valence and conduction) of carbon nanotube subbands.

The number of inequivalent cutting lines is defined by the number of different graphene two-atom unit cells in the carbon nanotube translational unit cell (N_t) (Saito, Dresselhaus, and Dresselhaus, 1998) and the length of each cutting line is given by $2\pi/T$, where T is the length of the nanotube unit cell (not to be confused with the symbol T used to denote temperature elsewhere in this review). From this simple picture, it can be deduced that carbon nanotubes can be either metallic or semiconducting depending on whether or not one of the cutting lines crosses the K or the K' points. It can be shown that nanotubes for which $\mathrm{mod}(n - m, 3) = 0$ are metallic; thus all armchair nanotubes are metallic, whereas zigzag nanotubes can be either metallic or semiconducting (Saito *et al.*, 1992). Figure 5(a) shows the electronic bands of graphene with cutting lines corresponding to an arbitrary carbon nanotube. In Figs. 5(b) and 5(c) the electronic band structures obtained through a simple zone-folding scheme for the armchair (8,8) and a zigzag (9,0) carbon nanotubes are

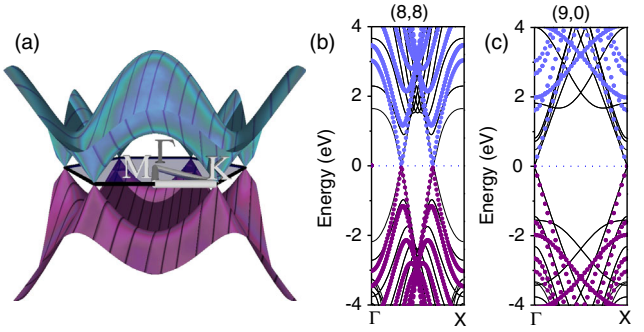

FIG. 5. (a) Electronic band structure of graphene showing the cutting lines corresponding to a nanotube's allowed states in black. Electronic band structure of (b) an (8,8) armchair and (c) a (9,0) zigzag carbon nanotube obtained from both zone-folding (solid circles) and *ab initio* calculations (solid lines).

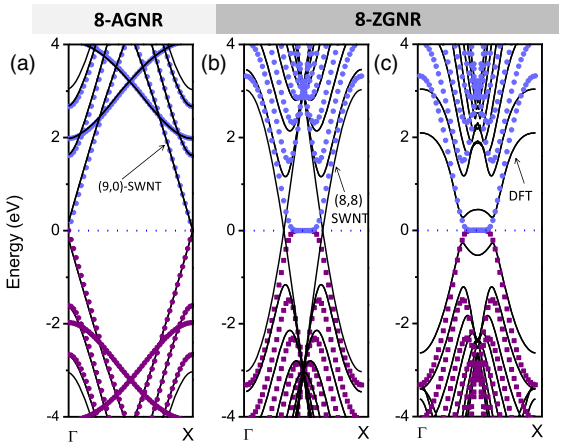

FIG. 6. Electronic band structure of (a) an armchair-edged (8-AGNR) and (b) a zigzag-edged graphene nanoribbon (8-ZGNR) calculated using an orthogonal simple tight-binding model (symbols) compared to the zone-folded bands (solid lines) for the corresponding carbon nanotubes [(9,0) and (8,8), respectively]. (c) Comparison between the electronic bands of a 8-ZGNR obtained by tight-binding (symbols) and by density function theory calculations (solid line), showing the effects of edges on the calculated electronic energy band structure.

shown as solid symbols, while for comparison we also show as solid lines the *ab initio* calculated band structures. It can be seen that near the Fermi energy (depicted as a horizontal dashed line at $E = 0$ eV), the zone-folding scheme can successfully describe the electronic properties. Moving away from the Fermi energy E_F, the contributions of curvature effects and electron-electron interaction effects become more important and the simple zone-folding approach fails to give an accurate description of the carbon nanotube's electronic properties as can be shown using density functional theory, for example, White, Robertson, and Mintmire (1993).

For GNRs, the appropriate boundary condition is that the wave function is confined in the lateral direction of the ribbon. This condition leads to a rather different quantization of the wave vectors than for the infinite nanotubes, which have no edge, unlike finite graphene samples and graphene ribbons. For instance, the electronic structure of the N_r-AGNR is similar (within a zone-folding scheme) to that of the $(n, 0)$ zigzag single-walled nanotube (SWNT) with $N_r = n - 1$ instead of the $N_r = 2n + 1$ nanotube which is the one formed by rolling up that particular ribbon. From this discussion, we conclude that armchair-edged GNRs will be metallic when $\mathrm{mod}(N_r + 1, 3) = 0$ and semiconducting otherwise (Saito *et al.*, 1992). Figure 6(a) shows the comparison between the electronic structure of the (9,0) carbon nanotube obtained by the zone-folding approach (solid symbols) as compared to the electronic structure of a $N_r = 8$ armchair-edged graphene nanoribbon (8-AGNR), solid lines, as calculated by applying the tight-binding approach described for graphene directly to the nanoribbon. The good agreement between the two results indicates that the edge effects are rather weak in AGNRs.

For ZGNRs, however, the situation is drastically changed. In principle, the band structure of a N_r-ZGNR obtained by applying the zone-folding approach should be similar to that of a (n, n) armchair nanotube with $N_r = n$. However, the presence of strong edge effects prevents this correspondence from taking place for zigzag GNRs. For example, a $N_r = 8$ zigzag GNR (8-ZGNR) obtained by applying the appropriate boundary conditions [symbols in Fig. 6(b)] should resemble that of an (8,8) SWNT. However, the electronic structure obtained by applying the tight-binding model directly to the nanoribbon structure [solid lines Fig. 6(b)] is quite different from the expected results, especially close to the Fermi energy. Special attention should therefore be given to the nondispersive band seen exactly at the Fermi level. This band corresponds to states localized near the graphene edge. The edge states have a strong ferromagnetic coupling which leads to the opening of a band gap and to a spin polarization of the electronic ground states, as seen in Fig. 6(c) (Nakada *et al.*, 1996). These edge effects have been widely discussed in the literature (Yazyev, 2010; Pan *et al.*, 2012; Li *et al.*, 2013; Wang, Jin, and Liu, 2013; Carvalho, Warnes, and Lewenkopf, 2014) and give rise to important spin-related magnetic effects (Enoki, Kobayashi, and Fukui, 2007). These effects are reviewed here.

C. Vibrational properties

The vibrational properties of graphite have been investigated experimentally using different techniques ranging from electron energy loss spectroscopy (EELS) (Oshima *et al.*, 1988; Siebentritt *et al.*, 1997), neutron scattering (Nicklow, Wakabayashi, and Smith, 1972), x-ray scattering (Maultzsch *et al.*, 2004), and by double-resonance Raman scattering (Saito *et al.*, 2001). However, it is only more recently that some of these techniques have become available for measurements on single-layer graphene (Yanagisawa *et al.*, 2005).

Theoretical investigations of the graphene and graphite phonon dispersion relations have also been performed using techniques such as a four neighbor force constant model (Saito *et al.*, 2001; Samsonidze *et al.*, 2003), a valence band force model (Perebeinos and Tersoff, 2009), and by *ab initio* calculations (Dubay and Kresse, 2003; Wirtz and Rubio, 2004; Mounet and Marzari, 2005; Yan, Ruan, and Chou, 2008). Figure 7 shows the density functional theory (DFT)

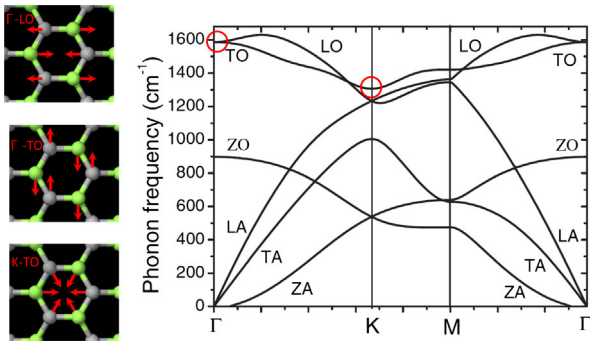

FIG. 7. DFT calculated phonon dispersion relations for monolayer graphene. The insets on the left show the phonon displacements associated with the optically active LO (top) and TO (middle) phonon modes at the Γ point and the *K* point TO phonon mode (bottom), corresponding to the modes highlighted by red circles. Adapted from Yan, Ruan, and Chou, 2008.

calculated phonon dispersion relations of single-layer graphene together with the atomic displacements associated with selected phonon modes (Yan, Ruan, and Chou, 2008).

The early theoretical models failed to describe the behavior of both the longitudinal optical (LO) phonon mode near the Γ point and the transverse optical (TO) phonon mode at the *K* point due to the presence of Kohn anomalies near those specific points in the Brillouin zone (Piscanec *et al.*, 2004) and to a breaking of the Born-Oppenheimer approximation (Pisana *et al.*, 2007). These effects are a consequence of the strong electron-phonon coupling in these materials. This coupling gives rise to important and interesting electronic properties as discussed in Sec. II.E. Recent attention has been directed to the study of the low frequency modes in few-layer graphene (FLG), which can be used to determine the number of layers in FLG, as well as the relative stacking order (Lui *et al.*, 2012, 2015; Tan *et al.*, 2012; Popov and Van Alsenoy, 2014).

Application of the zone-folding technique for understanding the vibrational properties of both carbon nanotubes and graphene ribbons is limited since the zone-folding method does not include important confinement and curvature effects (Jishi *et al.*, 1993; Saito *et al.*, 2001). For instance, the frequency of the radial breathing modes cannot be accurately predicted using the zone-folding approach. Furthermore, the carbon nanotube curvature also affects the magnitude of the force constant between the atoms, thus affecting the vibrational properties of the nanotubes. For this reason, more detailed approaches based on force constants (Savinskii and Petrovskii, 2002; Mahan and Gun, 2004), tight-binding (Yu, Kalia, and Vashishta, 1995), or *ab initio* calculations (Maultzsch *et al.*, 2002; Dubay and Kresse, 2003; Ye *et al.*, 2004; Gunlycke and White, 2008) have also been considered, especially for carbon nanotubes, in order to describe the vibrational properties of these systems more accurately.

In Fig. 8(a), we show the phonon dispersion relations of a (10,0) zigzag carbon nanotube obtained using *ab initio* calculations to evaluate the force constants. We also show the dispersion relations obtained by the zone-folding approach applied to the graphene phonon bands. Figure 8(a) also shows the vibrational density of states (VDOS) obtained with the two approaches (solid lines for the *ab initio* calculation and dashed lines for the zone folding). Furthermore, we show in Figs. 8(b) and 8(c) the predicted dependence of the Raman and infrared-active modes for $(n, 0)$ zigzag nanotubes on the nanotube index n. Since the diameter of zigzag nanotubes scales linearly with n, the result in Fig. 8 represents the diameter dependence of these particular phonon modes for the armchair nanotubes. Special attention must also be given to the higher frequency optical modes near 1590 cm^{-1} which are responsible for the *G* band in nanotubes and to the lowest frequency Raman-active phonon mode in carbon nanotubes, known as the radial breathing mode (RBM). This RBM mode shows an approximate $1/d_t$ dependence, with d_t being the nanotube diameter, and the observation of the RBM by Raman spectroscopy has long been used to identify the presence of carbon nanotubes in a given sample and to provide a measurement of their diameters (Rao *et al.*, 1997; Jorio *et al.*, 2001).

For graphene nanoribbons the theoretical and experimental research is not as vast as for carbon nanotubes. Using a DFT based approach, Gillen and co-workers found that the Γ-point

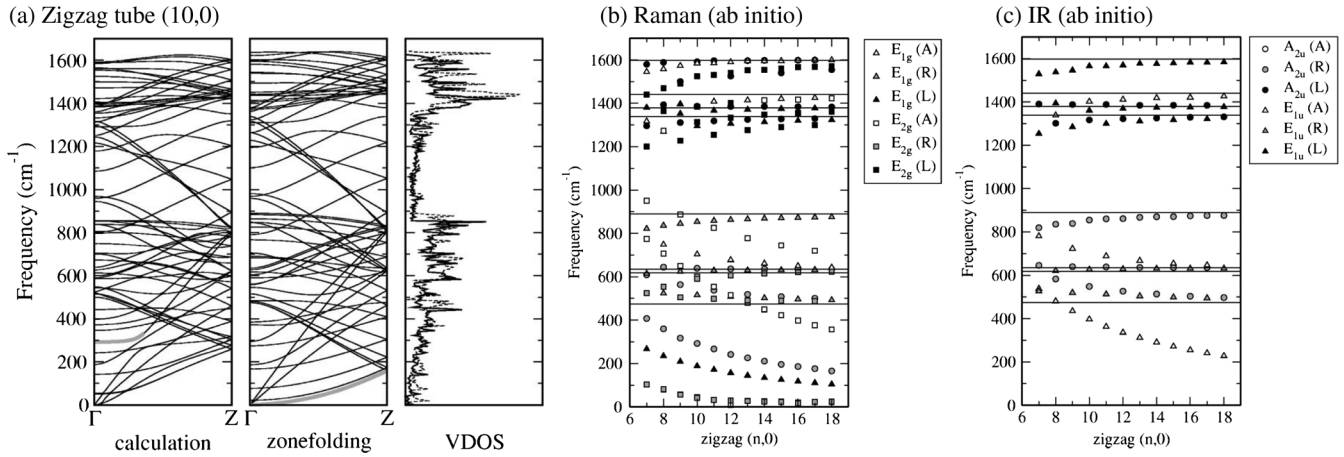

FIG. 8. (a) Phonon dispersion of a (10,0) carbon nanotube obtained by DFT calculations (left panel) and zone folding (middle panel) together with the vibrational density of states (VDOS) for both approaches (right panel). Solid and dashed lines are for data obtained with DFT calculations and the zone-folding scheme, respectively. Dependence of the frequencies of the (b) Raman-active and (c) IR active phonon modes as a function of the nanotube index n for selected $(n, 0)$ zigzag nanotubes. Adapted from Dubay and Kresse, 2003.

phonon frequencies of both armchair- and zigzag-edged graphene nanoribbons show a characteristic nanoribbon width dependence scaling with N_r^{-1} (Gillen *et al.*, 2009). The phonon frequencies have also been shown to depend on the metallic character of the AGNR (Gillen *et al.*, 2009) and on the degree of passivation of the edges (Yamada, Yamakita, and Ohno, 2008). Another numerical study used a combination of classical force field and DFT for investigating the phonon normal modes in hydrogen-terminated GNRS, where the presence of edge modes absent in graphene was shown to provide a clear signature of GNRs (Vandescuren *et al.*, 2008).

D. Raman spectroscopy

Raman spectroscopy is one of the most informative techniques for studying the vibrational and electronic properties of sp^2 graphitic materials. This is due to three important properties of graphene: (1) graphene's unique electronic band structure allows for resonance conditions using visible and infrared frequency excitations, (2) the low mass of carbon atoms and the strong carbon-carbon bonds lead to high energy (~0.2 eV) optical phonons in graphene and in other graphitic materials, and (3) the relatively strong electron-phonon coupling leads to many interesting properties (Piscanec *et al.*, 2004). The successful study of the these three properties has established Raman spectroscopy as a powerful tool for studying not only the vibrational properties of sp^2 nanocarbons, but also to unveil their special electronic properties and to characterize electron-phonon-coupling effects. Extensive studies of the Raman properties of graphite, graphene, and carbon nanotubes have already been carried out (Dresselhaus *et al.*, 2005; Malard, Pimenta *et al.*, 2009; Dresselhaus, Jorio, and Saito, 2010; Beams, Canado, and Novotny, 2015).

The Raman spectra of graphene is characterized by the presence of four main spectral peaks: the G band, the D band, the D' band, and the G' band [shown in Fig. 9(a)]. The G band is associated with the doubly degenerate (iTO and iLO) phonon modes (E_{2g} symmetry) at the Brillouin zone center (see Fig. 7). In fact, the G band is the only relevant graphene Raman peak [Fig. 9(a)] originating from a first-order Raman scattering process. The other three bands originate from a doubly resonant second-order process (Saito *et al.*, 2001; Maultzsch, Reich, and Thomsen, 2002). For instance, the G' and D bands originate from a second-order process involving two iTO phonons near the K point for the G' band, or one iTO phonon and one defect in the case of the D band. Since the G' band is observed at approximately twice the D-band frequency ($\omega_{G'} \cong 2\omega_D$), some prefer to call it the $2D$ band rather than the G' band which is a historic name for this feature, emphasizing the fact that the G' band is symmetry allowed. Finally, the D' band is related to a double-resonance effect involving a defect and one iTO phonon with a nonzero wave vector near the Γ point.

The Raman spectra of carbon nanotubes [see Fig. 9(b)] and graphene nanoribbons are populated with many other peaks [see Fig. 9(c)], which either become symmetry allowed due to the reduced symmetry of the nanotube or appear due to different double-resonance processes involving other phonons throughout the Brillouin zone. For carbon nanotubes, we

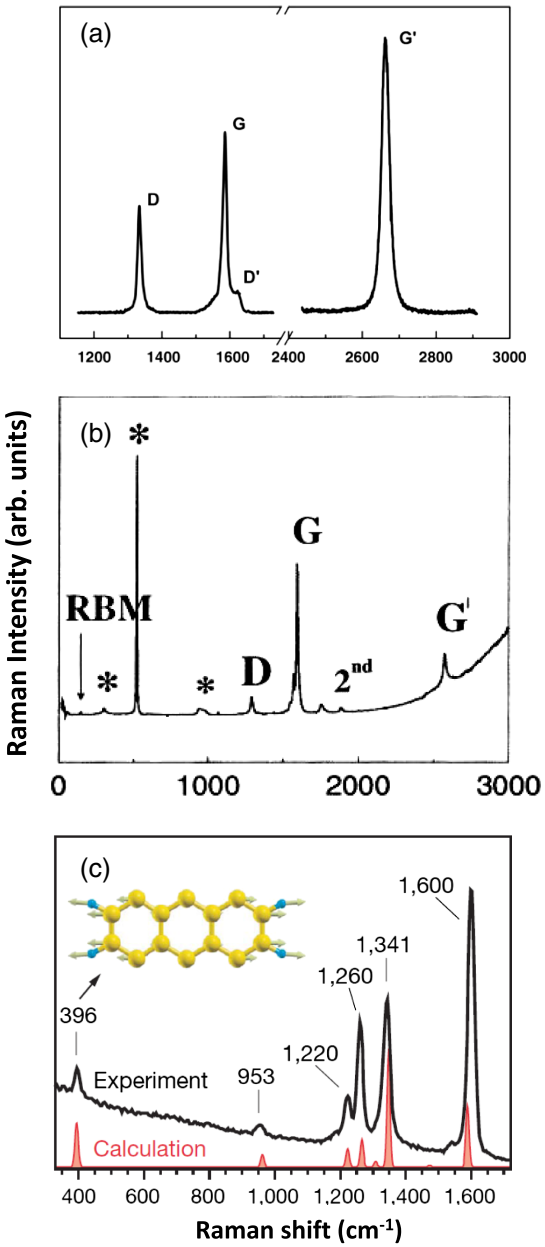

FIG. 9. Raman spectra of (a) graphene, (b) an isolated single-wall carbon nanotube, and (c) a $N_r = 7$ AGNR. Adapted from Malard, Pimenta *et al.*, 2009, Jorio *et al.*, 2001, and Cai *et al.*, 2010.

highlight the presence of the RBM phonon already discussed. This mode is related to the totally symmetric expansion and contraction of the tube diameter and which shows a diameter dependence

$$\omega_{\mathrm{RBM}} = \frac{227}{d_t}\sqrt{1 + C_e d_t^2}, \tag{9}$$

where C_e is a fitting parameter that accounts for the nanotube interaction with the environment (Araujo *et al.*, 2008; Dresselhaus, Jorio, and Saito, 2010), as discussed in Sec. III.A. The advances in understanding the optical transition energies for nanotubes were made possible only by the accurate (n, m) assignment procedures using the RBM frequency dependence on the SWNT diameter. For carbon

nanotubes the *G* band is composed of several different peaks. Kohn anomaly effects have also been shown to contribute significantly to the optical phonons in carbon nanotubes (Piscanec *et al.*, 2007; Sasaki *et al.*, 2008).

The study of the Raman spectra of graphene nanoribbons has been more limited due to the difficulties in the preparation of reliable samples. A number of studies reported in the literature are focused on ribbons obtained from unzipped carbon nanotubes which lead to fairly wide nanoribbons (Xie *et al.*, 2011; Jovanović *et al.*, 2014). But other synthesis techniques, such as on-surface polymerization, have been used to produce ultrathin monolayered ribbons which could be studied both by far-field and near-field Raman spectroscopy (Cai *et al.*, 2010; Shiotari, Kumagai, and Wolf, 2014). In Fig. 9(c) we show the Raman spectra of a 7-AGNR where the *G*-band and *D*-band peaks are observed at ∼1600 and 1341 cm^{-1}, respectively. An RBM-like feature is seen at ∼396 cm^{-1} and corresponds to the stretching of the ribbon width, as seen in the inset at the upper left of Fig. 9(c).

The double-resonance process allows Raman spectra to probe *k*-dependent phenomena in both graphene and carbon nanotubes (Venezuela, Lazzeri, and Mauri, 2011) and allows one to selectively probe the atomic structure of the edges (Cancado *et al.*, 2004). Furthermore, the dependence of the *D*-band intensity on the presence and types of defects can be used to evaluate the crystallinity and sample quality of all different types of sp^2 nanomaterials (Thomsen and Reich, 2007; Eckmann *et al.*, 2012; Rodriguez-Nieva *et al.*, 2014).

Raman spectroscopy has become one of the standard tools for studying and understanding the properties of sp^2 nanocarbons. Conversely, sp^2 carbon nanomaterials such as graphene and carbon nanotubes can also be used as tools for enhancing the Raman signal from adsorbed molecules. This effect has been observed recently and is generally referred to as the graphene-enhanced Raman spectroscopy effect (Jung *et al.*, 2010; Ling *et al.*, 2010, 2012; Ling and Zhang, 2010; Qiu *et al.*, 2011; Peimyoo *et al.*, 2012). There has been considerable debate about the origin of this effect as originating from a combination of different factors, such as a multiple reflection mechanism (Jung *et al.*, 2010), luminescence quenching (Xie *et al.*, 2009), and chemical coupling effects (Xu, Chen *et al.*, 2011; Xu, Xie *et al.*, 2011; Ling *et al.*, 2012). More recently, Barros and Dresselhaus (2014) proposed a model based on time-dependent perturbation theory which concisely describes the chemical coupling contribution to the Raman signal enhancement.

To illustrate this effect, we compare in Fig. 10(a) the Raman spectra of an organic molecule known as PTCDA [the structure of the PTCDA is shown in the inset to Fig. 10(a)] when the molecules are deposited on a SiO_2/Si substrate (black line) and when the molecules are on top of the monolayer graphene (green line). It can be seen that the Raman intensity of the PTCDA molecules are enhanced by a factor of 4 due to their interaction with graphene. Other molecules, such as CuPc, show enhancement factors on the order of 40 to 50. It has been shown experimentally that the enhancement factors are strongly dependent on which molecule is being probed, on the laser excitation energy used (Huang *et al.*, 2015), on the Fermi energy of the system, as

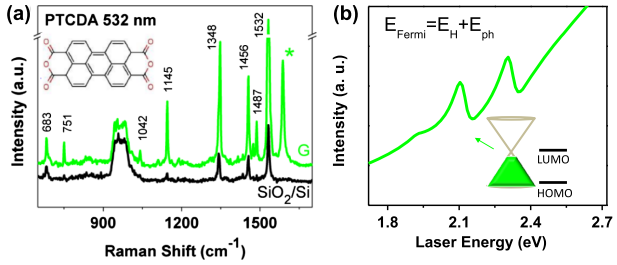

FIG. 10. (a) Raman spectra of 5 Å PTCDA on graphene (colored line) and on a blank SiO_2/Si substrate (black line) with a 532 nm excitation laser wavelength ($E_{laser} = 2.33$ eV). The inset shows the structure of the PTCDA molecule. From Huang *et al.*, 2015. (b) Calculated Raman intensity as a function of laser excitation energy for $E_F = E_H + \hbar\omega_q$. A homogeneous broadening of $\gamma = 0.03$ eV is applied. Adapted from Barros and Dresselhaus, 2014.

controlled by a gate voltage (Xu, Chen *et al.*, 2011; Xu, Xie *et al.*, 2011; Ling *et al.*, 2012), and even on the anisotropic nature of the substrate, as recently demonstrated for a few-layer black phosphorus substrate (Lin *et al.*, 2015).

Barros and Dresselhaus showed that for a given molecule on top of an ideal 2D metal (constant density of states) there is a set of conditions for maximum signal enhancement, summarized by

$$\text{(i)}\quad \hbar\omega_0 = E_L - E_H \quad \text{or} \quad \hbar\omega_0 = E_H - E_L + \hbar\omega_q, \tag{10}$$

$$\text{(ii)}\quad E_F = E_H \pm \hbar\omega_q \quad \text{or} \quad E_F = E_L \pm \hbar\omega_q, \tag{11}$$

$$\text{(iii)}\quad \hbar\omega_0 = E_F - E_H \quad \text{or} \quad \hbar\omega_0 = E_F - E_H + \hbar\omega_q, \tag{12}$$

$$\text{(iv)}\quad \hbar\omega_0 = E_L - E_F \quad \text{or} \quad \hbar\omega_0 = E_L - E_F - \hbar\omega_q, \tag{13}$$

where E_H and E_L are the energies of the highest occupied molecular orbital (HOMO) and the lowest unoccupied molecular orbital (LUMO) states of the molecule, respectively, E_F is the Fermi energy of the metal, $\hbar\omega_q$ is the energy of the phonon, and $\hbar\omega_0 = E_{laser}$ is the laser excitation energy. For graphene, the nearly linear electronic bands near the Dirac point add an extra enhancement contribution which increases linearly with the distance between the excited electron energy and the energy of the Dirac point. Figure 10(b) shows the dependence of the Raman intensity on the laser excitation energy for a PTCDA molecule ($E_L = -4.7$ eV, $E_H = -6.8$ eV) on top of graphene. The phonon energy 0.2 eV corresponds approximately to that of the 1532 cm^{-1} Raman peak. For simplicity the Dirac cone was considered to be matching the HOMO energy, and the Fermi energy to be given by $E_F = E_L - \hbar\omega_q$. In addition, all the matrix elements for the molecule and graphene interactions are considered to be associated with a unitary matrix. It can be seen that the laser excitation energy of 2.33 eV used in the experiment shown in Fig. 10(a) is close to the predicted enhancement peak and thus was chosen for the laser source in the experiments.

E. Electron-phonon coupling

Here we briefly discuss the rich body of evidence showing how the electronic and vibrational degrees of freedom are coupled and how this coupling affects the intrinsic properties of sp^2-based nanocarbons. This strong coupling is manifested both in the electronic and transport properties of these materials and also in their vibrational properties. For instance, the lower frequency G-band peak (G^-) in the Raman spectra of metallic nanotubes undergoes a frequency softening associated with a strong electron-phonon coupling near the Fermi energy in these materials (Dubay, Kresse, and Kuzmany, 2002). In carbon nanotube bundles this interaction leads not only to a softening of the peak, but also to an asymmetric line shape called the Breit-Wigner-Fano (BWF) (Brown *et al.*, 2001). This strong electron-phonon coupling was shown to also be important for graphite and graphene. It was determined that this phonon softening can be well described in terms of a Kohn anomaly (Piscanec *et al.*, 2004; Farhat *et al.*, 2007).

Turning to the electronic properties, the presence of Kohn anomalies causes the appearance of dynamical band gaps in the electronic band structure (Dubay, Kresse, and Kuzmany, 2002; Piscanec *et al.*, 2007; Samsonidze *et al.*, 2007), which can have important consequences on the transport properties of metallic sp^2 carbon materials (Park *et al.*, 2004; Sapmaz *et al.*, 2006).

The effect of this strong electron-phonon interaction is not limited to metallic or quasimetallic carbon nanomaterials. For example, the presence of sidebands in the optical absorption and photoluminescence spectra of semiconducting carbon nanotubes have also been associated with phonon-mediated excitations and relaxation processes (Chou *et al.*, 2005; Perebeinos, Tersoff, and Avouris, 2005; Plentz *et al.*, 2005).

The electron-phonon coupling in graphitic materials, although of small magnitude compared to other materials, has a large effect and implies important consequences for the detailed Raman spectra in sp^2 carbon materials. Besides the aforementioned phonon softening effects, the strong electron-phonon coupling is responsible for the appearance of the dominant second-order Raman features (such as the D band, the D' band, and the G' band) in graphene, carbon nanotubes, and other sp^2 carbon materials through a double resonance process (Saito *et al.*, 2001; Maultzsch, Reich, and Thomsen, 2002). Additionally, the strong electron-phonon coupling means that in graphitic materials the vibrational and electronic degrees of freedom are strongly coupled, which indicates that the Born-Oppenheimer approximation, one of the pillars of solid-state physics theory, is not strictly valid for these materials, as noted previously (Pisana *et al.*, 2007).

Finally, as another illustration of the strong electron-phonon coupling, Duque *et al.* (2011) found that the Raman resonance profile for isolated semiconducting single-wall carbon nanotubes is asymmetric regarding the resonances associated with the incident and scattered photons due to a breaking of the Condon approximation.

III. EFFECTS OF THE ENVIRONMENT

Carbon nanomaterials have a large percentage of their surface area exposed to the environment, causing their properties to be highly sensitive to their interaction with their surroundings. Obtaining a proper description for these environmental effects is usually a complicated task since it involves the interface between nanoscopic and macroscopic systems. In this review, we selected a few examples to illustrate how environmental effects play an important role in affecting the vibrational, electronic, and optical properties of graphene and carbon nanotubes. These particular examples have been selected because of their importance for the proper characterization and identification of carbon nanotube and graphene samples and because they could be well described using effective models, allowing for a solid understanding of the processes responsible for these specific effects. The environment is expected also to affect other properties of sp^2 nanocarbons. For instance, it is known that the transport properties of graphene are strongly dependent on the interaction of graphene with the substrate, whereas both the electronic and vibrational properties of graphene are changed when in contact with other 2D nanostructures, an effect which plays an important role in the tailoring of the properties of 2D.

A. Phonons

The sensitivity of phonons in sp^2 nanocarbons to their external environment is remarkable and both the van der Waals interaction (translated as a strain effect) and the charge transfer (translated as a doping effect) perturb the phonon energies because electrons and phonons are strongly coupled in graphene and in related nanocarbon systems. Changes in frequencies, intensities, and linewidths have been extensively used for monitoring in detail the interaction of carbon nanostructures with different external environments into which the nanocarbons are introduced. As a result of such studies, it was found that the frequency of the G-band Raman peak can be used to probe strain. The average frequency downshift with stress was determined to be $\Delta\omega = -5\omega_0^{-1}$ cm^{-1} MPa^{-1}, where ω_0 is the vibrational frequency of the G band in the absence of strain (Frank *et al.*, 2011). This method is very useful for the quantitative evaluation of the stress or strain introduced by the external environment.

Recently, Raman-active phonon modes were used to characterize graphene deposited on the (100), (110), and (111) faces of copper single crystals (Frank *et al.*, 2014). This study pointed out that both the strain and the doping level of graphene grown on a copper surface is independent of the crystal quality or the topography of the substrate. In contrast, strain and doping levels were shown to depend on the atomic details of the copper lattice orientation, which therefore plays a key role. On Cu(100) and (110) surfaces, the graphene sheet grows flat and undoped, showing a narrow second-order G' band (linewidth about 16 cm^{-1}), while the same phonon mode appears to be broadened to about 20 cm^{-1} and the Fermi level is shifted by about 250 meV for graphene grown on a Cu (111) surface. This shift in Fermi level is responsible for the upshifting of $\omega_{G'}$ by 18 cm^{-1} compared with the graphene grown on Cu(100) and (110) faces.

As mentioned previously, one of the unique vibrational modes in carbon nanotubes is the so-called radial breathing

mode. The frequency ω_{RBM} of this vibrational mode scales with nanotube diameter d_t, according to $\omega_{\mathrm{RBM}} = A/d_t + B$, where the parameters A and B vary from sample to sample, while A is an intrinsic property of the nanotube and B is associated with environmental effects, such as the presence of a substrate, functional molecules, bundling, etc. The value of $A = 227\ \mathrm{cm}^{-1}\,\mathrm{nm}^{-1}$ was found by fitting data for a special sample called "supergrown" carbon nanotubes, where the tubes are aligned and are located relatively far from each other and therefore hardly interact with each other.

The physical basis for the environmental effect on the RBM frequency in carbon nanotubes was elucidated by considering a harmonic oscillator for a cylindrical shell subjected to an inward pressure $p(x)$. Using a continuum elastic model, the displacement $x(t)$ of the cylinder in the radial direction is described by (Longhurst and Quirke, 2006)

$$\frac{\partial^2 x(t)}{\partial t^2} + \frac{2Yx(t)}{(1-\nu^2)\rho d_t} + \frac{p(x)}{h\rho} = 0, \tag{14}$$

where $p(x) = (24K/s_0^2)x(t)$, and K gives the van der Waals interaction strength, s_0 is the equilibrium separation between the nanotube and the environmental shell, Y is the Young's modulus, ρ is the mass density per unit volume, ν is the Poisson's ratio, h is a term which measures the thickness of the shell, and t is the time. In the limit of vanishing pressure $p(x) = 0$, and the fundamental frequency of the nanotube is obtained as

$$\omega^0_{\mathrm{RBM}} = \frac{1}{\pi c}\left[\frac{Y}{\rho(1-\nu^2)}\right]^{1/2}\frac{1}{d_t}. \tag{15}$$

For a nonvanishing $p(x)$, which means that the environment plays a role and interacts with the nanotube, the frequency is given by

$$\omega'_{\mathrm{RBM}} = 227\left[\frac{1}{d_t^2} + \frac{6(1-\nu^2 K)}{Yhs_0^2}\right]^{1/2}, \tag{16}$$

where the correction term is $6(1-\nu^2K)Yh = 26.3\ \text{Å}^2/\mathrm{eV}$. Thus, the shift in the RBM phonon frequency is given by $\Delta\omega = \omega'_{\mathrm{RBM}} - \omega^0_{\mathrm{RBM}}$. By adjusting $\Delta\omega$ using experimental data, the parameter K/s_0^2 was found to be $2.2\ \mathrm{meV/Å}^4$. For simplicity, Eq. (16) can be rewritten as Eq. (9) for describing the frequency of the RBM taking into account the van der Waals interaction due to the environment (Araujo *et al.*, 2008). The constant $C_e = [6(1-\nu^2K)Yh][K/s_0^2](\mathrm{nm}^{-2})$ accounts for the environment effects on the radial breathing phonon frequency. The value of C_e was found to be 0.05, 0.059, 0.065, and $0.067\ \mathrm{nm}^{-2}$ for single-wall carbon nanotube samples of HiPCO@SDS, alcohol-assisted chemical vapor deposition (CVD), nanotubes sitting on a SiO_2 substrate and freestanding carbon nanotubes, respectively (Jorio *et al.*, 2011).

B. Excitons

Excitons in carbon nanotubes are unique insofar as the electronic structure of graphene has two nonequivalent energy bands near the K and K' corners of the Brillouin zone leading to what is usually called *two valleys*. Because of this effect, which is sensitive to spin and spin-orbit interaction in sp^2 carbon, an optical transition can occur vertically in k space but the electron and hole can reside in the same valley or the electron can either be in one valley and the hole in the other valley. This latter case means that an exciton can be formed in real space but the hole and electron will not recombine if they are in different valleys and this exciton is called a *dark* exciton. When both the electron and the hole belong to the same valley and the symmetry requirements allow them to recombine radiatively, the exciton is called a *bright* exciton. The eigenfunctions of the excitons in carbon nanotubes were discussed previously in terms of symmetry and the effective mass approximation (EMA) and the envelope approximation, such that (Barros *et al.*, 2006)

$$\psi^{\mathrm{EMA}}(\vec{r}_e, \vec{r}_h) = \sum_{v,c}{}' A_{vc}\phi_c(\vec{r}_e)\phi_c^*(\vec{r}_h)F_\nu(z_e - z_h), \tag{17}$$

where ϕ_c (ϕ_v) are the conduction (valence) band eigenstates, and F_ν is the envelope function which provides an *ad hoc* way to describe the localization of the exciton along the z axis. The prime in the summation stands for the fact that the sum includes only the electron and hole states associated with singularities in the density of states.

The energy of the excitons in carbon nanotubes can be calculated by solving the Bethe-Salpeter equation which takes into account the static screened Coulomb interaction w, which in the random phase approximation is given by

$$w = \frac{\nu}{\kappa\epsilon(\vec{q})}, \tag{18}$$

where κ is the dielectric constant and $\epsilon(\vec{q}) = 1 + \nu(\vec{q})\Pi(\vec{q})$ is the dielectric function. By calculating the polarization function Π and the Fourier transform of the unscreened Coulomb potential, it is possible to obtain the exciton energy and wave functions.

We note that the environmental effect is considered by the value of κ but it is rather difficult to evaluate because the electric field involving the electron-hole pair is not only distributed in the environment around the nanotube but also within the nanotube itself and κ includes the screening effect from both the tube and the environment. Therefore, for reproducing the experimental data of excitons in carbon nanotubes, it is necessary to consider an effective κ which depends both on the environment and on the nanotube diameter. Thus, κ in Eq. (18) represents the screening of the electron-hole pair by the core ($1s$) and σ electrons (κ_{tube}) and by the surrounding materials (κ_{env}), where the term $\epsilon(q)$ accounts for the polarization function of the π electrons. In order to fit the experimental data, an empirical equation for κ was found to be

$$\kappa = C_\kappa\left(\frac{p}{d_t}\right)^\alpha, \tag{19}$$

where $p = 1, 2, 3, 4, \ldots$ refers to the distance of the cutting lines (the allowed states for the nanotubes) from the K point being, respectively, related to $E^S_{11}, E^S_{22}, E^M_{11}, E^S_{33}, \ldots$. The

exponent α in Eq. (19) was found to be 1.7 for all exciton energy transitions, but different C_k values are needed for different samples to account for the different environmental conditions. The diameter dependence of κ in Eq. (19) depends on the exciton size and the amount of electric field sensitive to the dielectric constant κ_{env} of the surrounding material. The results, rationalized in terms of the model and experiments, indicate that κ_{env} is more effective for excitons related to the low energy subbands E_{11}^S and E_{22}^S, which means that the electric field of the excitons for these states has a considerable extension outside the nanotube volume, in contrast to E_{33}^S and E_{44}^S, where the electric field is more localized inside the tube. Therefore, the binding energies for the E_{11}^S and E_{22}^S excitons are strongly affected by the environment (influence of κ_{env}) and the environment should be considered in order to describe the photophysics of nanotubes more accurately. This environmental κ dependence is also useful for optical-based sensors where changes in the surroundings of the nanotubes induce measurable changes in the energies of the optical emission.

IV. PROPERTY ENGINEERING

In this section we review how some properties of sp^2 nanocarbons can be rationally designed. We discuss the effect of strain, defects, edge structure, layer stacking (e.g., graphene on top of graphene and graphene on top of other 2D materials) on the electronic, vibrational, and magnetic properties of graphene, nanoribbons, and nanotubes.

A. Strain

We discuss here how the properties of sp^2 nanocarbons can be tailored by controlling the level of strain and how the effect of strain on the electronic properties can be probed by resonant light scattering (Mohiuddin *et al.*, 2009). The topic of band gap engineering will be reviewed for graphene, nanoribbons, and nanotubes (Yang and Han, 2000; Ni *et al.*, 2008; Y. Li *et al.*, 2010).

1. Graphene and nanoribbons

Because graphene is isotropic in plane, the elastic tensor in graphene is isomorphic to the elastic tensor of the two-dimensional rotation group. When the bond lengths and angles are changed due to strain, the hexagonal symmetry is broken and some symmetry-breaking effects emerge, such as the opening of an electronic gap and the splitting of doubly degenerate phonon modes. Understanding the effects of strain is crucial because most of the practical applications envisaged for graphene and carbon nanoribbons have their critical nanostructures sitting on a substrate or these nanostructures are immersed within a polymer matrix.

The strain tensor in graphene is written as

$$\epsilon = \begin{pmatrix} \epsilon_A & \gamma \\ 0 & \epsilon_Z \end{pmatrix}, \tag{20}$$

where ϵ_A and ϵ_Z denote, respectively, the uniaxial strain applied along the armchair and zigzag directions, and γ is the shear strain. Figure 11(a) provides a schematic view of an

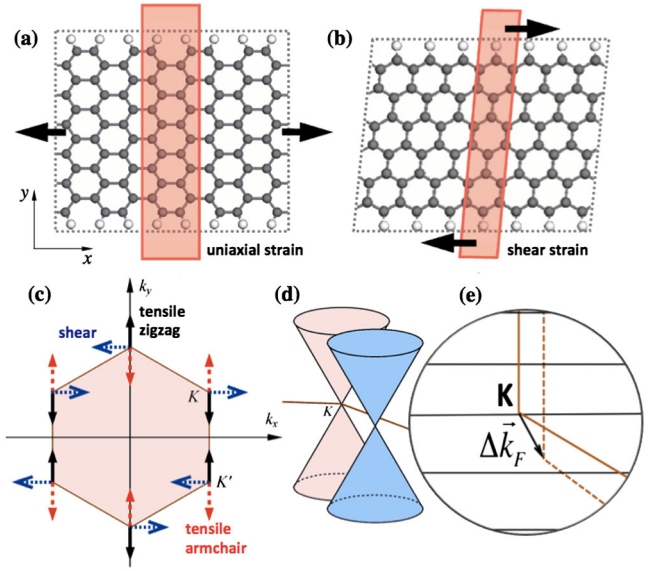

FIG. 11. (a) A uniaxial and (b) shear strain applied to graphene nanoribbons in real space. The red shaded rectangles denote the unit cell of the strained structures. (c) The displacement of the K point in reciprocal space due to the tensile strain (along the armchair and zigzag directions) and the shear strain is shown. The effect of strain is to displace the Dirac cone from the K point to another position of the Brillouin zone (d). (e) The allowed states for low-dimensional nanostructures, such as nanoribbons and nanotubes, are illustrated by the cutting lines. The effect of strain on those structures can be interpreted based on the displacement of the Fermi points by a vector $\Delta\mathbf{k}_F$. Adapted from Y. Li *et al.*, 2010.

uniaxial strain ϵ_A applied along an armchair direction of a carbon nanoribbon, and of a shear strain γ [Fig. 11(b)] applied to a zigzag nanoribbon. The general picture of the effect of strain on the properties of graphene can be interpreted in terms of the displacement of the K point in reciprocal space. The displacement of the Dirac point, which can be represented by a vector $\Delta\mathbf{k}_F$, depends on how the strain is applied to the real lattice in reciprocal space, as illustrated in Figs. 11(c) and 11(d) for tensile and shear strain, respectively. An analytical expression based on the tight-binding model is possible to obtain for describing the band gap opening E_{gap} in graphene as a function of strain (Y. Li *et al.*, 2010)

$$E_{\text{gap}} = 3ts \begin{cases} (1+\nu_A)\epsilon_A & \text{(strain along armchair direction)}, \\ (1+\nu_Z)\epsilon_Z & \text{(strain along zigzag direction)}, \\ \gamma & \text{(shear strain)}, \end{cases} \tag{21}$$

where t, s, and ν are, respectively, the hopping parameter t between nearest-neighbor orbitals, the wave-function overlap s between the nearest-neighbor orbitals, and the Poisson ratio γ.

The effect of strain in opening a band gap in graphene due to the displacement of the Dirac point away from the K point is shown by the points in Fig. 12(a). The lines of E versus strain are fit to the analytical expressions in Eq. (21) to simulations (points) obtained with DFT calculations. The

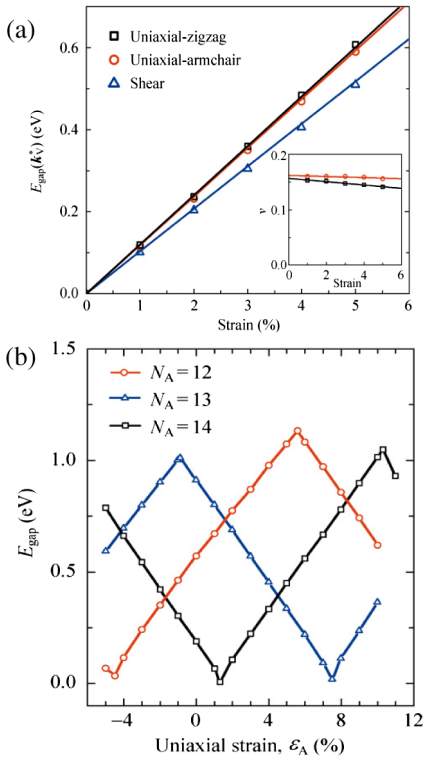

FIG. 12. Band gap opening E_{gap} as a function of strain for (a) graphene and (b) armchair nanoribbons. The inset to (a) shows the variation of the Poisson ratio ν along the armchair and zigzag directions as a function of strain. Adapted from Y. Li *et al.*, 2010.

shear strain effect is less pronounced than that of the uniaxial strain, while strain applied along the armchair and zigzag directions corresponds to responses that differ slightly from one another. These small deviations are due to a small difference in the Poisson ratio along these directions, as shown in the inset to Fig. 12(a).

This simple picture where strain moves the Dirac point also allows us to understand many strain-induced phenomena, such as band gap opening, semi-conducting to metallic transitions in both carbon nanotubes and carbon nanoribbons by correlating the position of the allowed states (cutting lines) and the position of the K point, as illustrated in Fig. 11(e). Since strain can be used to break symmetry in graphene and to induce a band gap opening, it is expected that the electronic gap in carbon nanoribbons is also affected by strain. Armchair graphene nanoribbons can be classified into three families depending on the number of C-C dimers N_r (see Fig. 3): $N_r = 3p$, $N_r = 3p + 1$, and $N_r = 3p + 2$, where p is an integer number. Strain affects the band gaps of the three families differently, as shown in Fig. 12(b). The oscillatory behavior (opening and closing of band gaps) can be understood by looking at the simple picture shown in Fig. 11(e), where the strain moves the Dirac point. Between two cutting lines there are no allowed states for the ribbon, so a band gap is observed, which reaches a maximum value in the midpoint between two cutting lines. As the Dirac point crosses the next cutting line, allowed states are available and the band gap closes. The linear dependence of the band gap closing comes from the fact that, close to the K point, the energy dispersion for monolayer graphene is linear. The maximum of the gap E_{gap}^{max} can be analytically obtained considering that the quantization of the states and E_{gap}^{max} scales with the width (which is proportional to $N_A + 1$) of the armchair nanoribbon as

$$E_{gap}^{max} = \frac{\sqrt{3}\pi t}{N_A + 1}, \tag{22}$$

where N_A is the number of C-C dimers along the width of the ribbon, as defined in Fig. 3. The shear strain also affects the band gap of armchair nanoribbons, but the effect is on the energy scale of meV and is not as strong as the effect predicted for uniaxial strain.

The properties of zigzag nanoribbons are also affected by strain and since the allowed states for the zigzag ribbons are perpendicular to those of armchair nanoribbons, the simple model discussed in terms of a displacement of the Dirac point and of the cutting lines suggests that the zigzag nanoribbons are more affected by the application of shear strain. However, calculations show that neither uniaxial nor shear strain open a gap in zigzag nanoribbons, unless spin polarization is taken into account (Y. Li *et al.*, 2010). The electronic band structure for a zigzag nanoribbon as a function of different levels of uniaxial and shear strain is shown in Figs. 13(a) and 13(b),

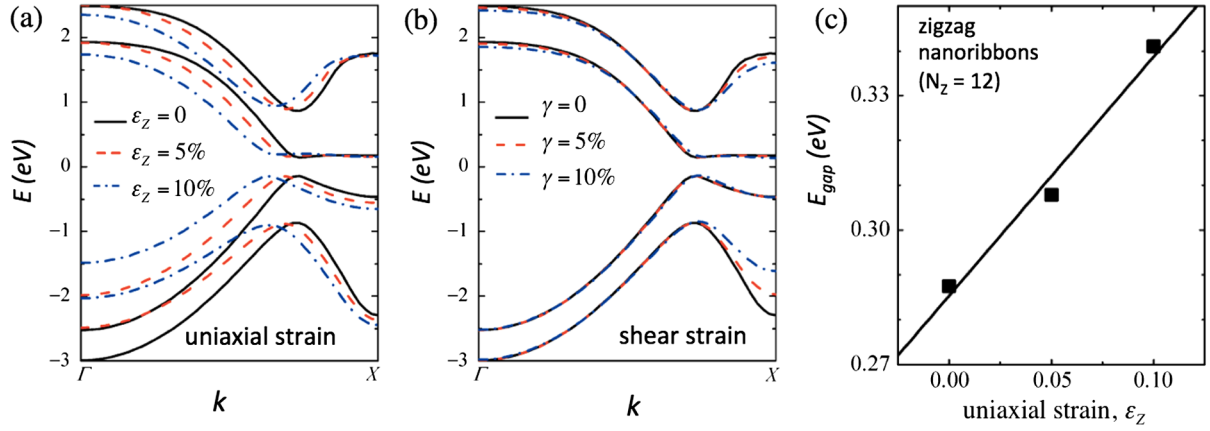

FIG. 13. Electronic band structure considering spin-polarization effects for a zigzag nanoribbon as a function of (a) uniaxial and (b) shear strain. (c) Band gap opening as a function of uniaxial strain for the band structure shown in (a). Adapted from Y. Li *et al.*, 2010.

respectively. The band gap opening is observed for the case of uniaxial strain, as illustrated in Fig. 13(c).

Since one of the effects of strain is to break the symmetry of the lattice, the phonon spectra measured by means of resonance Raman spectroscopy have been used for probing the strain effect in graphene in more detail (Ni *et al.*, 2008; Mohiuddin *et al.*, 2009). In Fig. 14(a) the splitting of the doubly degenerate G band is shown as a function of strain (Mohiuddin *et al.*, 2009). The strain induces a splitting of the doubly degenerate G band into G^+ and G^- peaks and changes in lineshapes which are interpreted in terms of atomic displacements perpendicular and parallel to the uniaxial strain direction [see Fig. 14(c)]. The strain coefficients values $\partial\omega_{G^+}/\partial\epsilon = -10.8\ \mathrm{cm}^{-1}/\%$ and $\partial\omega_{G^-}/\partial\epsilon = -31.7\ \mathrm{cm}^{-1}/\%$ were obtained by fitting the experimental data shown in Fig. 14(a). These frequency shift coefficients are large, which is a consequence of the fact that graphene is one of the most stretchable solids ever measured. This sensitivity of the G-band mode to strain is very useful from a practical point of view in order to evaluate the magnitude of the strain level that can be achieved in controlling graphene-based devices.

Local strain produced by using the tip of a scanning probe microscope has also been used for studying strained graphene. For example, strain-induced diamondization of few-layer graphene was reported at room temperature (Barboza *et al.*, 2011). By combining experimental and modeling results, this study showed the possibility of synthesizing a new 2D material named *diamondol*, which is a ferromagnetic insulator with different band gap energies for each value of spin.

2. Carbon nanotubes

Strain can also be used for engineering properties of carbon nanotubes but, in this case, curvature and chirality make the picture more complex than for carbon nanoribbons. Both theoretical and experimental investigations have been carried out in order to understand the electronic, optical, transport, vibrational, and mechanical properties of carbon nanotubes under strain. Isotropic (hydrostatic pressure) and nonisotropic (uniaxial and torsional) strain have been exploited, and the observed effects of strain on the electronic properties were found to depend sensitively on the symmetry of the carbon nanotube. A pioneering study in this regard was performed by Yang and Han (2000) who obtained analytical expressions for quantifying the displacement of vector $\Delta\mathbf{k}_F$ shown in Fig. 11(e) in terms of strain along the nanotube axis (l) and the circumference (c) as follows:

$$\Delta k_F^c a_{\mathrm{CC}} = (1+\nu)\epsilon\cos(3\theta) + \tau\sin(3\theta), \tag{23}$$

$$\Delta k_F^l a_{\mathrm{CC}} = -(1+\nu)\epsilon\cos(3\theta) + \tau\sin(3\theta), \tag{24}$$

where the superscripts c and l denote the displacement components along the nanotube circumference and along the axis, respectively, and a_{CC} is the carbon-carbon distance in unstrained graphene. Here ϵ and τ are the uniaxial and torsional strains, ν is the Poisson ratio, and θ is the nanotube chiral angle. By considering small strain values and energies close to the K point, where the linear approximation remains valid, the gap variation in carbon nanotubes due to strain is given by

$$\Delta E_{\mathrm{gap}} = \mathrm{sgn}(2p+1)3t[(1+\nu)\epsilon\cos(3\theta) + \tau\sin(3\theta)]. \tag{25}$$

In this equation, p is an integer and t is the hopping parameter between nearest-neighbor orbitals. The changes in band gap for some (n,m) nanotubes as a function of strain ϵ obtained by plotting Eq. (25) (lines) along with simulations (points) are shown in Fig. 15 and excellent agreement between the analytical model and the simulation data is observed. It can be seen that armchair nanotubes are insensitive to uniaxial strain and sensitive to torsional strain, while zigzag nanotubes behave in the opposite way (see Fig. 15). Chiral nanotubes have an intermediate behavior.

Raman spectroscopy has proven a sensitive method for probing the effect of strain on carbon nanotubes induced by manipulating the nanotube with an atomic force microscopy (AFM) tip (Cronin *et al.*, 2004, 2005; Souza Filho *et al.*, 2005; Araujo *et al.*, 2012). Previous experiments have been carried out using micro-Raman measurements on individual tubes and the latest advances in experimental techniques allowed the mapping of the strain with high resolution along a single nanotube using tip enhanced Raman spectroscopy (Yano *et al.*, 2013).

In the same way that the electronic properties can be controlled by applying strain to a carbon nanotube, it is also possible to use the electronic properties of nanotubes in order to control the lattice strain. Control of this nanotube property opens up the possibility of using carbon nanotubes for quantum nanomechanical actuators, a possibility which has been investigated both experimentally (Baughman *et al.*, 1999; Gupta *et al.*, 2004; Hartman *et al.*, 2004; Chen *et al.*, 2010) and theoretically (Gartstein, Zakhidov, and Baughman, 2003; Sun *et al.*, 2003; Verissimo-Alves *et al.*, 2003; Hartman *et al.*, 2004; Pastewka *et al.*, 2009; Vieira *et al.*, 2014).

For example, Pastewka and co-workers investigated how the introduction of a fixed electronic charge to an individual single-wall carbon nanotube affects the nanotube axial and

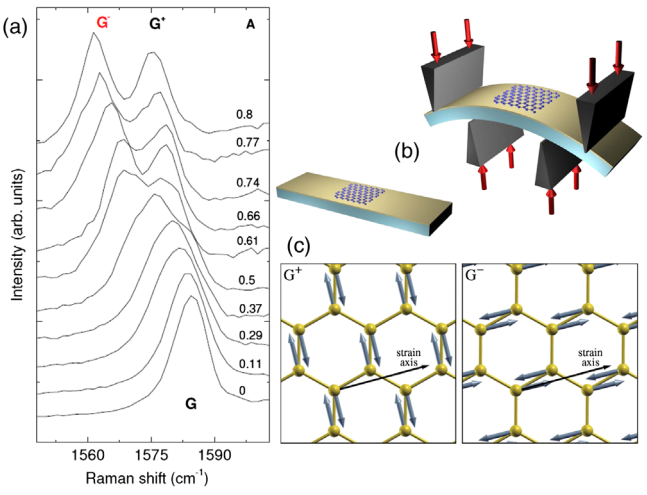

FIG. 14. (a) G-band evolution as a function of the amount of strain applied [numbers on the right side of (a)] in arbitrary units to a graphene layer immersed in a polymer matrix, as illustrated in (b). (c) Eigenvectors for the G^- and G^+ modes obtained by DFT based calculations in strained graphene. Adapted from Mohiuddin *et al.*, 2009.

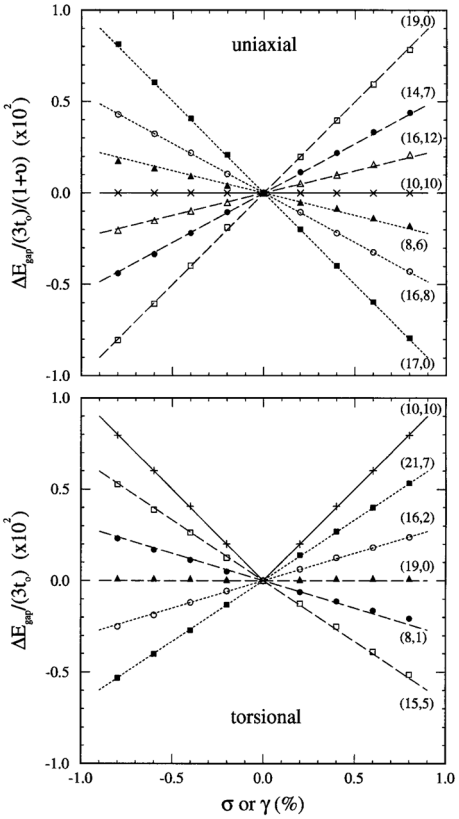

FIG. 15. Effects of uniaxial and torsional strain on the band gap of several (n, m) nanotubes. Lines are for the analytical model and points are simulation data using the tight-binding method. Adapted from Yang and Han, 2000.

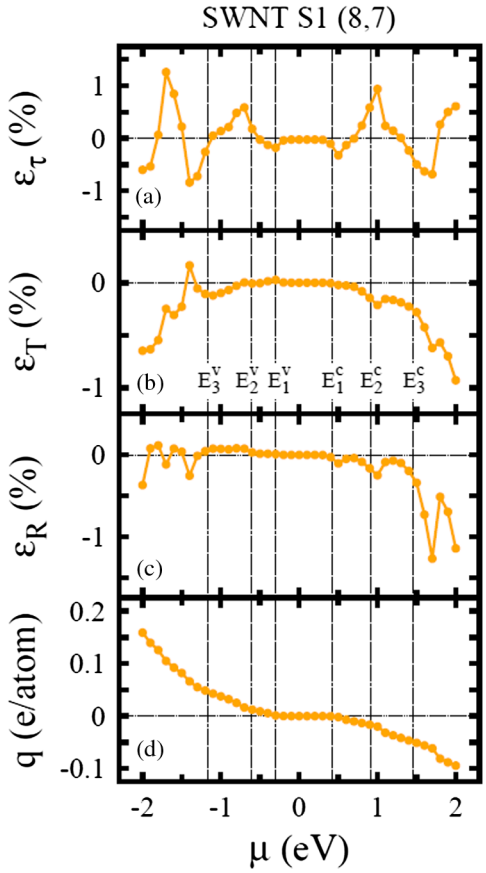

FIG. 16. (a) Torsional ϵ_τ, (b) axial ϵ_T, (c) radial strains ϵ_R, and (d) the resulting injected charge q as a function of the Fermi energy (μ) for the (8,7) semiconducting SWNT. The charge is given in units of the elementary charge e per carbon atom in the SWNT structure. The vertical lines show, as a guide to the eye, the approximate energy values for the valence subband maxima (E_1^v, E_2^v, and E_3^v) and the conduction subband minima (E_1^c, E_2^c, and E_3^c). From Vieira *et al.*, 2014.

radial strains (Pastewka *et al.*, 2009). In another study, an extended tight-binding model was used to show that axial, radial, and torsional strains of more than 1% can be imposed onto single-wall carbon nanotubes simply by controlling the nanotube Fermi energy (Vieira *et al.*, 2014).

Figure 16 shows the dependence of the torsional, axial, and radial strains for selected SWNTs as a function of the Fermi energy (μ) of the tube. For the torsional strain, Fig. 16(a) shows that whenever the Fermi energy approaches one of the extremes of the carbon nanotube electronic subbands, the resulting torsion increases (Vieira *et al.*, 2014). For the axial strain [Fig. 16(b)] and for the radial strain [Fig. 16(c)], there is a clear tendency for compression as the Fermi energy moves away from the charge neutrality point ($\mu = 0$). However, similarly to the case of the torsional strain, there is a change of behavior of axial and radial strains whenever the value of Fermi energy μ reaches one of the nanotube subband extrema. Similar results are observed for both metallic and semiconducting nanotubes. Furthermore, it was also shown that the Coulomb repulsion between the electrons leads to even higher values of torsional, axial, and radial strains as a function of increasing Fermi energy (Vieira *et al.*, 2014).

B. Edges

Here we discuss how the presence of edges affects the properties of graphene, and also the effect of edge modifications beyond simple quantum confinement effects. Special attention is then given to the presence of edge magnetism in both zigzag and chiral ribbons (Li *et al.*, 2013; Wang, Jin, and Liu, 2013; Carvalho, Warnes, and Lewenkopf, 2014) and how these magnetic properties are modified by doping and strain. The effect of inherent edge disorder is also discussed, based on experimental data obtained using local characterization techniques (Tao *et al.*, 2011; Pan *et al.*, 2012).

The edge structure has an important effect on the physical properties of graphene nanoribbons. From an experimental point of view, the atomic structure of the ribbons depends on the preparation method used for shaping the nanoribbons. Wang *et al.* (2011) developed nanoribbons with high-quality edges made by unzipping single- and double-walled carbon nanotubes. Tao *et al.* (2011) observed evidence of a 1D edge state in graphene nanoribbons by scanning tunneling microscopy (STM) and scanning tunneling spectroscopy (STS) techniques in nanoribbons prepared by unzipping carbon nanotubes (Kosynkin *et al.*, 2009; Jiao *et al.*, 2010). The sample preparation method used in that work generates chiral graphene nanoribbons with different widths and lengths, and

both zigzag and armchair edges are present in such samples. Most of the studies focused on electrical transport properties, and such measurements do not enable a clear connection between local atomic structure and electronic properties of the nanoribbons. The work of the Crommie group significantly advanced this research field because these authors were able to use subnanometer resolution for accessing the local electronic structure along the edges of the nanoribbons (Tao *et al.*, 2011). Figure 17(a) shows the atomically resolved topography of a (8,1) graphene nanoribbon along with its structural model [Fig. 17(b)]. The dI/dV measurements along a series of black points along a line perpendicular [Fig. 17(c)] and red points along a line parallel [Fig. 17(d)] to the edge reveal interesting features of the local density of electronic states. Very close to the edge, the dI/dV spectra exhibit two peaks which are separated in energy by $\Delta = 23.8 \pm 3.2$ meV for the (8,1) nanoribbon and by $\Delta = 27.6 \pm 1.0$ meV for the (5,2) nanoribbon [see the inset to Fig. 17(c)]. It was further observed that

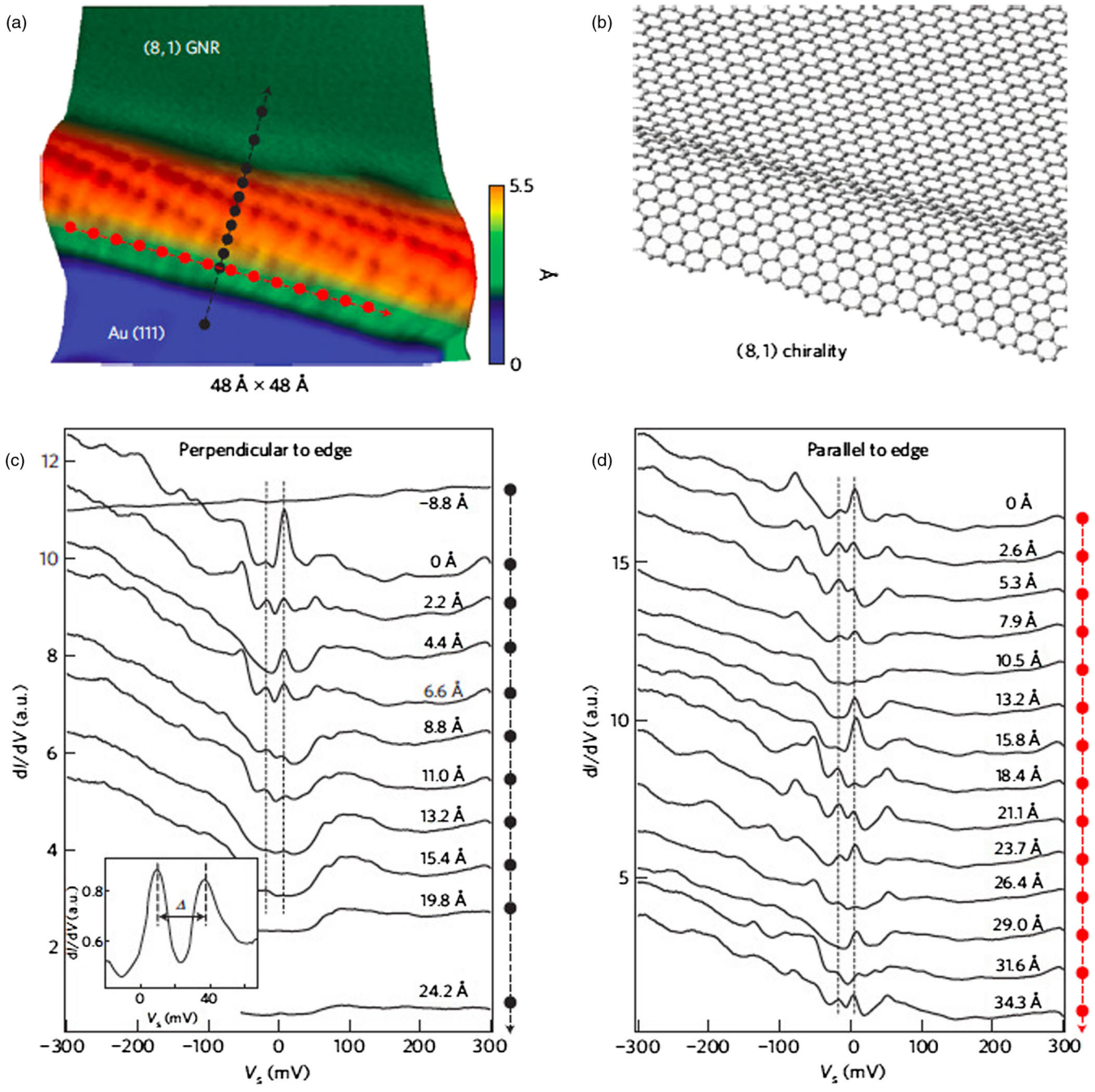

FIG. 17. Scanning tunneling microscopy (STM) measurements on graphene nanoribbons obtained by unzipping carbon nanotubes. (a) STM topographical image ($V_S = 0.3$ V, $I = 60$ pA, $T = 7$ K) of the edge of an (8,1) graphene nanoribbon over an Au(111) surface and (b) its corresponding structural model. STS measurements of the graphene nanoribbon measured along a line (c) perpendicular (black points) and (d) parallel (red points) to the ribbon edge. The inset to (c) shows a high-resolution dI/dV spectrum for another nanoribbon with a (5,2) geometry, thus showing the energy splitting Δ of the edge states. From Tao *et al.*, 2011.

the amplitude of these peaks decays exponentially when moving perpendicularly away from the edge. On the other hand, when moving parallel to the edge, the dI/dV oscillates with the same spatial period (about 20 Å) of the atomic edge. Furthermore, it was experimentally observed that the gap energy decreases as the ribbon's width increases. These experimental results provide evidence through scanning tunneling spectroscopy measurements that clearly establish the existence of 1D spin-polarized edge states which are coupled across the width of the ribbon, with an increased coupling as the ribbon width decreases (Tao *et al.*, 2011).

The dI/dV spectroscopic features in Figs. 17(c) and 17(d) can be interpreted using a Hubbard-like model with an Hamiltonian based on a single-orbital nearest-neighbor tight-binding Hamiltonian and an on-site Coulomb repulsion term U, which accounts for electron-electron interactions. Figures 18(a) and 18(b) show the electronic band structure and the density of states for an (8,1) nanoribbon obtained by including electron-electron interactions. It is clearly seen that when the on-site Coulomb repulsion interaction is turned on ($U \neq 0$), the degenerate edge state peak at the Fermi level disappears and several new van Hove singularities appear, along with a gap at 0 eV. Since the electron-electron interaction is responsible for the onset of magnetic correlations, the opening of the gap shown in the inset of Fig. 17(c) induces a ferromagnetic alignment of spins along the edges and an antiferromagnetic correlation across the edges (Tao *et al.*, 2011). The calculated gap shown in Fig. 18(b) has been correlated with the two peaks experimentally observed in the STS measurements [inset of Fig. 17(c)], thus providing evidence for the formation of spin-polarized edge states in zigzag nanoribbons.

It should be mentioned that the Coulomb repulsion energy value $U = 0.5t$ (where $t = 2.7$ eV) which was found to fit the experimental data is different from the $U = 1.3t$ value predicted by first-principles calculations (Yazyev, 2008). This difference in values of U might be due to the screening provided by the gold substrate, thus pointing out the sensitive role of the environment on the electronic properties of nanocarbons, as discussed previously in Sec. III. Recent theoretical results obtained using a more realistic Hamiltonian including next-nearest-neighbor interactions affect the simple description of the magnetic properties of nanoribbons and further experiments on the local density of states as a function of the width of the nanoribbons are needed to clarify this point (Carvalho, Warnes, and Lewenkopf, 2014).

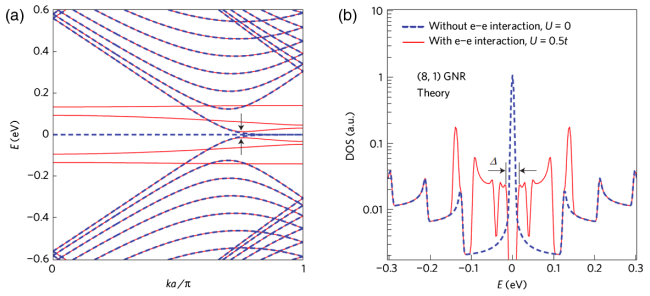

FIG. 18. (a) Electronic band structure and (b) the corresponding electronic density of states for the (8,1) graphene nanoribbon, calculated using a Hubbard-like model without (dashed blue lines) and with (solid red lines) electron-electron interactions. The calculated energy splitting of $\Delta = 29$ meV in (b) is comparable to the experimentally observed value of 23.8 ± 3.2 meV. From Tao *et al.*, 2011.

Graphene nanoribbons can also be grown by CVD but the edges of these samples tend to be defective, and consequently the local densities of states of these ribbons are much more complex than those for ribbons obtained through unzipping carbon nanotubes (Jia *et al.*, 2011). Pan *et al.* (2012) investigated CVD-grown nanoribbons using high-resolution STM and STS measurements and their findings point out that besides the edges of the CVD ribbons being parallel, they have a different local density of states, where the edge states are different on each side of the ribbons. Figure 19 shows the STM and STS measurements for a nanoribbon and calculations based on a structural model where the edges are modeled as having a (3,1) chirality edge on one side of the ribbon and a pentagon–heptagon (5–7) reconstructed edge on the other side of the ribbon [Fig. 19(d)]. The local density of state calculations [Fig. 19(d)] that best match the experimental dI/dV data [see the dashed square in Fig. 19(e) which was measured at the position marked by the cross in Fig. 19(a)] correspond to the 5–7 reconstructed edge where both the energy splitting of the bands and the peak asymmetry are captured. The asymmetry of the peak intensity comes from the broken electron-hole symmetry induced by the defective edge.

Another interesting edge-induced effect is the possibility of using an external electric field to make a graphene nanoribbon act like a spin-semiconductor material. Wang, Jin, and Liu (2013) showed theoretically that graphene nanoribbons with sawtooth edges [see Fig. 20(e)] have a ferromagnetic ground state and, furthermore, that, by applying a transverse electrical

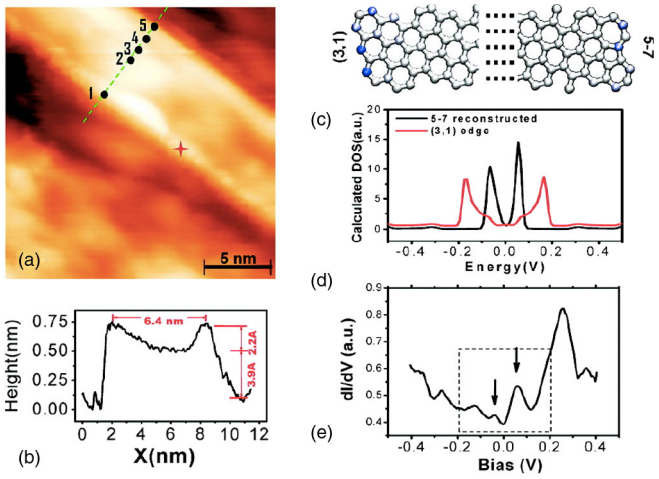

FIG. 19. (a) STM image and (b) a line profile of height measurements of a CVD-grown 6.4 nm wide nanoribbon. (c) An atomic model is shown for the ribbon with the (3,1) chirality on one edge and a pentagon–heptagon 5–7 reconstructed edge on the other side. The local density of electronic states is calculated as a function of energy in (d) considering the different edges shown in (c). (e) The experimental dI/dV measurements measured at the edges of the nanoribbon are shown [see the + in (a)]. From Pan *et al.*, 2012.

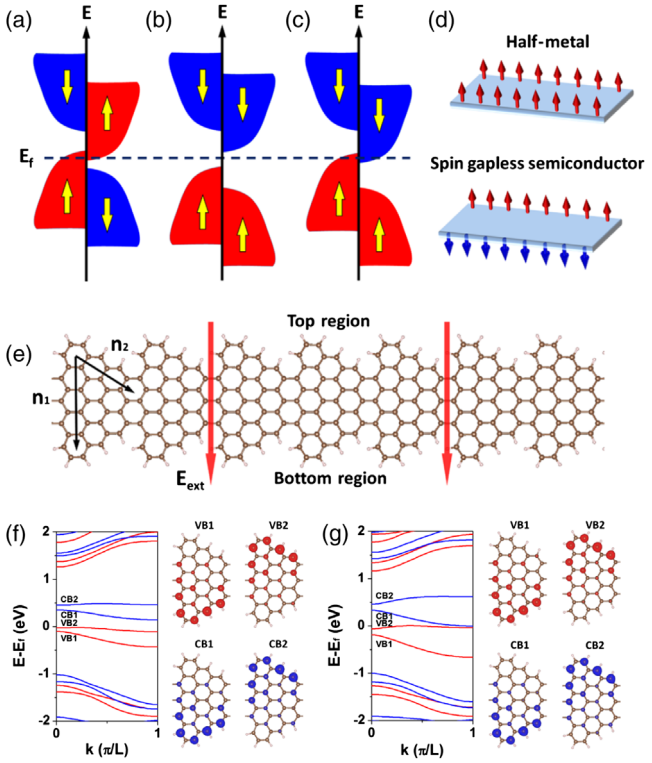

FIG. 20. Schematic diagrams for the electronic band structure of a (a) half-metal, (b) spin-semiconductor, and (c) a spin gapless semiconductor nanoribbon along with their spin-polarization configurations at the edges (d). (e) The atomic model of the sawtooth nanoribbons defining the chiral index (n_1, n_2) is shown for $(n_1, n_2) = (4, 3)$. (f), (g) The electronic band structures $E - E_F$ vs k of the graphene nanoribbons for external electric fields E_{ext} of 0.04 and 0.0 eV/Å are shown. The right panels in (f) and (g) denote the partial charge densities for the four levels close to the Fermi level E_F. From Wang, Jin, and Liu, 2013.

field, the charge carriers become not only spin polarized in energy space, they also become spatially separated at different sides of the nanoribbon. It follows that spin-up electrons are polarized on one edge and spin-down holes are oppositely polarized on the other edge [Figs. 20(f) and 20(g)]. The spin induced electronic band gap shown in this study can be engineered by applying an electric field in order to reach a new state called a *spin gapless semiconductor* and is shown in Fig. 20(c). The presence of the transverse electric field breaks the degeneracy of the low energy bands (close to the Fermi level) for spin-up and spin-down states. Furthermore, as the magnitude of the electric field increases, the energy gap between the lower energy spin-up band and the higher energy spin-down band decreases, and this gap closes when the electric field is 0.063 eV/Å (Wang, Jin, and Liu, 2013). Calculations predict that the spin semiconducting states are preserved up to the presence of 10% of randomly distributed vacancies at the edges. Such robustness considerations are likely to play an important role in spintronics-based applications.

The synthesis of carbon nanoribbons with control of their atomic edges was reported by Cai *et al.* (2010, 2014) who used a bottom-up approach through the so-called Ullmann coupling for obtaining straight but also chevron- or wigglelike edge systems as shown in Fig. 21. These nanowiggles are conceptually built by joining segments of armchair and zigzag nanoribbons (Costa Girão *et al.*, 2011). By considering the nanoribbon axis, the structure of these nanowiggles is composed of parallel and oblique segments as shown in Fig. 21(a). It is possible to generate a set of different nanowiggles by changing the width [defined as the number of C-C dimer lines as shown in Fig. 21(a)] of the parallel [P] and oblique [O] sectors. The existence of these degrees of freedom provides considerable control for designing the details of the wiggle structures. The complete description of the structure can be written as (P_α, O_β), while $\alpha, \beta = A, Z$, and A and Z stand for armchair and zigzag edges, respectively, in Fig. 21. Regarding the structures of the edges, four possible geometries are possible, as illustrated in Figs. 21(b)–21(e).

The particular case of graphene nanowiggles has been investigated theoretically in detail to unveil a rich set of electronic, magnetic, and thermal properties depending on the combination of edge types (Costa Girão *et al.*, 2011; Liang *et al.*, 2012; Liang, Girão, and Meunier, 2013). Figure 22 shows the electronic band structures for the nanowiggles described in Figs. 21(b)–21(e) calculated using DFT (dashed lines) and tight-binding (solid lines) methods. On the top of each panel in Fig. 22 we show the spin polarization being red for spin up and black for spin down. The most remarkable effect of the edges on the properties of nanowiggles is the spin-polarization arrangements that emerge by combining segments with armchair and zigzag edges (as in Fig. 21).

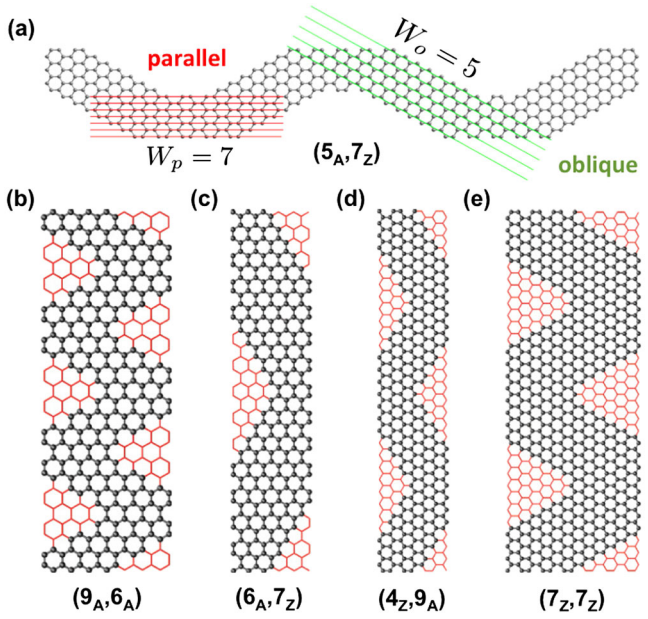

FIG. 21. (a)–(e) Structural model and nomenclature for graphene nanowiggles, which are made up of successive oblique and parallel cuts in armchair (A) or zigzag (Z) graphene patches. (a) Illustration of how the widths of the parallel (W_p) and oblique (W_o) sectors are defined in terms of the number of C-C lines (red and green). W_p and W_o refer, respectively, to the number of parallel and oblique atomic rows that are present in a nanowiggle in the two indicated directions. The structure shown in (b) is one of the structures actually synthesized by Cai *et al.* (2010). From Costa Girão *et al.*, 2011.

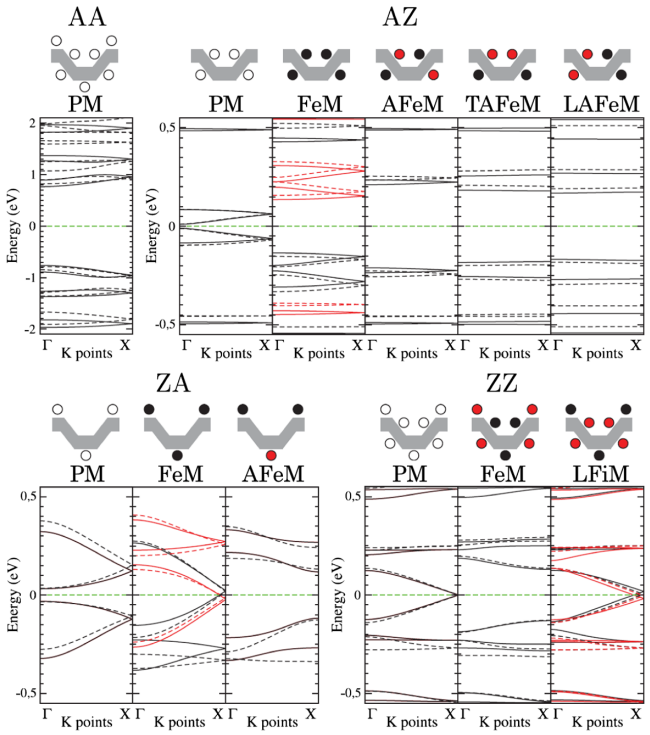

FIG. 22. Electronic band structures $E(k)$ calculated along $\Gamma - X$ using DFT (dashed lines) and tight-binding (solid lines) methods corresponding to the different magnetic states for the representative *AA*, *AZ*, *ZA*, and *ZZ* graphene nanowiggles, shown in Figs. 21(b)–21(e). The schematic spin distributions (red: down, black: up) are shown on top of each panel. From Costa Girão *et al.*, 2011.

As expected, nanowiggles with both parallel and oblique sectors composed of armchair edges (*AA* configuration in Fig. 22) do not exhibit any polarization spin along the edges and the system is paramagnetic (PM). Conversely, if one sector features a zigzag edge, the nanowiggle shows a rich set of magnetic states, as illustrated in Fig. 22 for the *AZ*, *ZA*, and *ZZ* configurations. For these three configurations, the spins are polarized in different zigzag segments. In the case of *AZ* and *ZA* nanowiggles, the armchair segments limit the magnetic domains and the most stable configuration is the antiferromagnetic (AFeM) arrangement, which is due to the bipartition of the graphene lattice. However, deliberate choices of the initial guess for the on-site occupations allow the self-consistent computational process to converge into four different magnetic states as is schematically shown on the top of Fig. 22 for the *AZ* case. This variety of possible metastable spin distributions makes carbon nanowiggles potentially interesting materials to be used as components for spintronic devices.

There is still a large gap between the body of theoretical predictions for magnetism in nanoribbons and their experimental realization. A key point for preserving the edge magnetism in zigzag nanoribbons is that the periphery C atoms should have a pure sp^2 coordination. This is difficult to achieve experimentally under normal conditions since nonmagnetic molecules, such as O_2, H_2O, NH_3, and CO_2, will strongly interact with an open edge. Calculations predict that only for a low hydrogen concentration, which is quite challenging to achieve in experimental realizations, can the nanoribbons exhibit edge magnetism (Wassmann *et al.*, 2008). Therefore, a critical point in producing edge magnetism of carbon nanoribbons is to find chemical groups that can passivate the edges and at the same time preserve the magnetism. In this context, ethylene (C_2H_2) is predicted to be a good potential candidate (Li *et al.*, 2013).

C. Superlattices

When two graphene layers are placed on top of each other, a superlattice structure, which is also called a moiré pattern, is generated by the mismatch generated by the rotation angle θ between the top and bottom layers. This superlattice structure can be defined by the lattice parameters ($|\vec{r}_1|$, $|\vec{r}_2|$) which are usually much larger than the graphene lattice parameters ($|\vec{a}_1|$, $|\vec{a}_2|$), as shown in Fig. 23.

As discussed, the electronic structure for monolayer graphene near the Dirac point is linear and consequently the density of states increases linearly when departing from the neutrality point. On the other hand, twisted bilayer graphene, Fig. 23, shows one van Hove singularity (vHs) in the DOS below and another vHs above the Fermi level, Fig. 24 (G. Li *et al.*, 2010). Of particular interest is the energy difference between these two singularities which can be tuned by controlling the relative twist angle θ between the two layers. The presence of these two van Hove singularities near the Dirac point generates new electronic properties which can be potentially exploited in graphene-based devices.

The appearance of the van Hove singularities in the density of electronic states for twisted bilayer graphene (tBLG) can be studied by considering the electronic band structure for two noninteracting layers misoriented by an angle θ. In

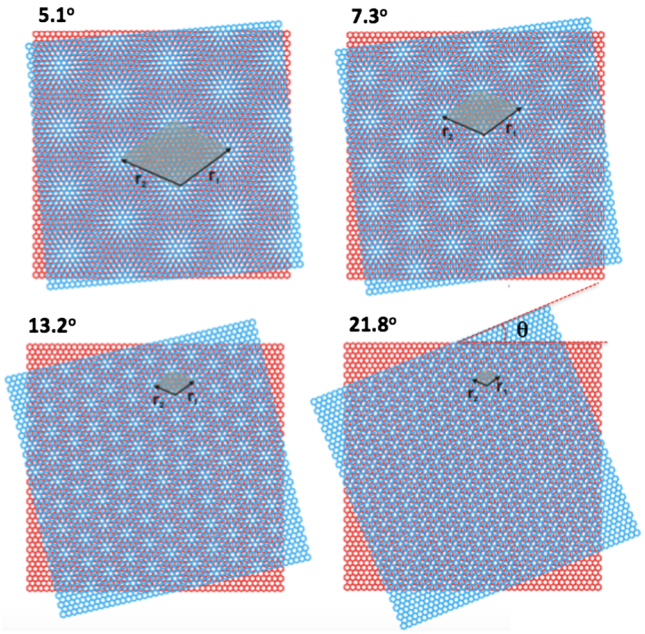

FIG. 23. Schematic diagrams of the moiré patterns that are formed by the twisting angles $\theta = 5.1°$, 7.3°, 13.2°, and 21.8°. The gray area highlights the unit cell, which decreases as the twisting angle θ increases. Adapted from Carozo *et al.*, 2013.

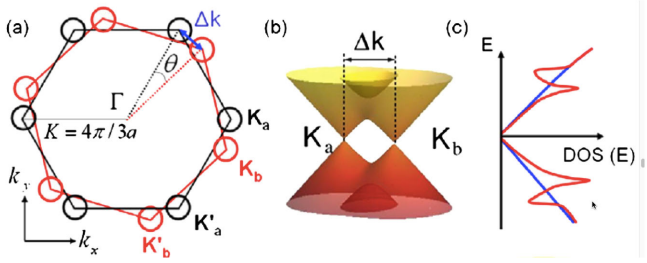

FIG. 24. (a) Brillouin zone for a twisted bilayer graphene (see Fig. 23) rotated by θ, where the circles represent the isoenergies for Dirac cones from the bottom layer (black) and from the top layer (red). (b) The energy dispersion for each Dirac cone close to the K point and in the vicinity where the two cones overlap, giving rise to van Hove singularities as shown in (c). The two Dirac cones are separated in reciprocal space by Δk which depends on θ, as shown in (a). Adapted from Kim *et al.*, 2012.

momentum space close to the K point of the Brillouin zone, the Dirac cones of each layer are rotated by θ from one another and the van Hove singularities appear at the wave vectors, where the two cones overlap with each other as schematically shown in Fig. 24. Therefore, the properties of electrons and phonons are strongly affected by the interaction between the two layers. The magnitude of the interaction can be finely tuned by changing the twist angle θ as discussed below.

Figures 25(a)–25(c) show electronic band-structure calculations for tBLG using *ab initio* calculations for the three distinct twist angles $\theta = 9.4°$, 13.2°, and 21.8°. The Dirac cones are still present in each case, but the slope of the $E(k)$ linear dispersion changes as a function of the twist angle, thus implying that the electronic spectrum can be described by massless Dirac fermions, but with a Fermi velocity renormalized by the twist angle (Luican *et al.*, 2011). For very low values of the twist angle (i.e., below 3°), the Dirac cone picture breaks down, because the density of states is dominated by the singularity and the carriers are localized in a charge density wave (Luican *et al.*, 2011).

Close to the M point of the Brillouin zone we can observe maxima and minima in the $E(k)$ dispersion curves in Figs. 25(a)–25(c), which also give rise to van Hove singularities. This stacking of layers discussed previously leads to a system with electronic properties significantly different from that of double layer graphene with the standard AB Bernal stacking, where massive Fermions are present (Castro Neto *et al.*, 2009). The detailed analysis of the effect of the number of layers on the electronic properties is described, for example, in detail by Partoens and Peeters (2007). Figure 25(d) shows the absorption spectra calculated using dipole transition matrix elements between the valence and conduction Kohn-Sham states (Carozo *et al.*, 2013). The absorption spectrum was smoothed out by Gaussian functions with widths of 0.05 eV, and the optical transition energies were enhanced by 18% to account for quasiparticle effects (Kim *et al.*, 2012). Figure 25(d) shows the calculated absorption spectra for six values of θ, where well-defined absorption peaks with maxima at $E_L^{\max}$ can be clearly seen. The $E_L^{\max}$ values for the resonance transitions as a function of θ are calculated by DFT and are plotted as open squares in Fig. 25(e). The open circles represent values replicated by symmetry, since $E_L^{\max}$ is expected to be symmetrical around $\theta = 30°$ and have a 60° period. The $E_L^{\max}$ results in Fig. 25(e) can be fitted by the simple equation

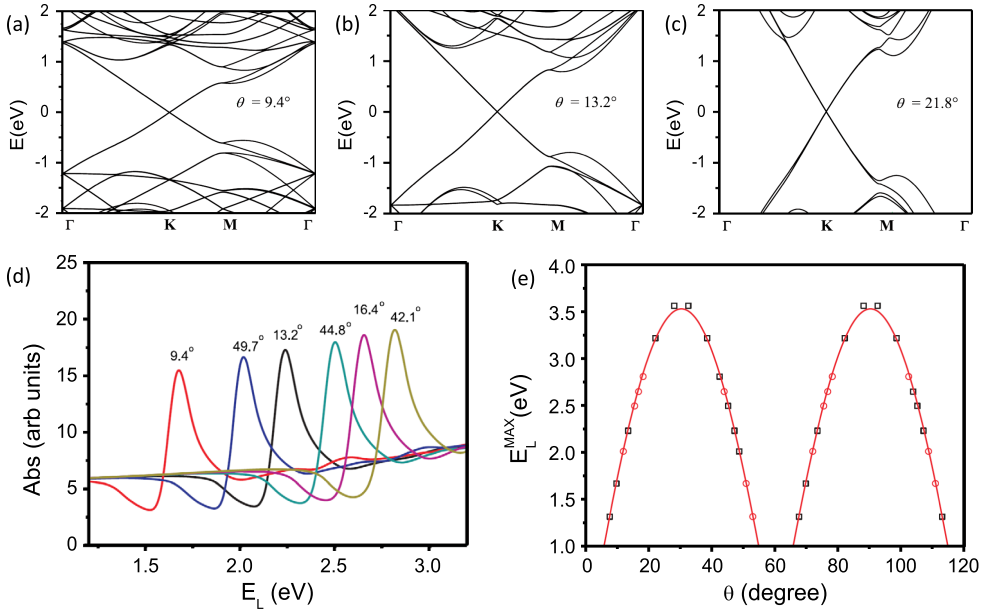

FIG. 25. (a)–(c) Electronic band structure for twisted bilayer graphene for three distinct twist angles θ (9.4°, 13.2°, and 21.8°, respectively) taken over the range of energy −2.0 to +2.0 eV. (d) Calculated optical absorption spectra near the absorption peak as a function of twist angle θ. (e) θ dependence for the optical absorption peaks at $E_L^{\max}$, according to the results calculated in (d), and others not shown. Squares denote calculated data and circles are values replicated by symmetry. The solid line is a fit to the equation $E_L^{\max} = E_0|\sin(3\theta)|$. Adapted from Carozo *et al.*, 2013.

$$E_L^{\max} = E_0 |\sin(3\theta)|, \tag{26}$$

where $E_0 = 3$ eV. The maximum energy absorption occurs at $\theta = 30°$, where the largest possible separation $\Delta\mathbf{k}$ between Dirac points in reciprocal space occurs [Fig. 24(e)].

Raman spectroscopy has been used to investigate special properties of tBLG by exploiting the resonance of the laser energy with the electronic transitions that are enhanced in intensity at van Hove singularities (Carozo *et al.*, 2011, 2013; Righi *et al.*, 2011; Havener *et al.*, 2012; Kim *et al.*, 2012; Sato *et al.*, 2012). The novel phenomenon emerging in the Raman spectra of tBLG is the enhancement of the G band and the activation of new modes called rotation-induced bands R, R' and disorder-induced D-like bands. Note that while R stands for rotation, the superscript is used to be consistent with the nomenclature used for the D and D' bands. All these spectroscopic phenomena allow researchers to develop models to determine the twist angle with good precision using Raman spectroscopy and also to learn more details about phonon scattering in graphene-based systems. One way of preparing tBLG is by folding a large graphene sheet onto itself by using an AFM tip as schematically shown in Fig. 26(b) (Carozo *et al.*, 2011). With this method, the AFM tip is first used (operating in the contact mode) to scan the graphene sheet along one line. After generating a defect line, the tip is used to fold the graphene and a portion of the sample ends up with a tBLG region, as shown in Fig. 26(a). In this particular experiment, the twist angle can be directly measured by the lattice resolution AFM [see the inset of Fig. 26(a)] and for this case it was found that $\theta = 6°$. When the Raman spectrum is measured in the folded region, a sharp R' mode is observed at about 1625 cm^{-1} [see Fig. 26(c)], which appears only in the tBLG region as confirmed by the Raman intensity map shown in Fig. 26(e). It is also fortunate that the intensity of this rotation-induced mode relative to the G band depends on the laser excitation energy, as illustrated in Fig. 26(c). The resonance window measured for both the G band and the R' band of tBLG with $\theta = 13.3°$ shows a peak at about 2.7 eV, which is in agreement with the prediction of Eq. (26) (Carozo *et al.*, 2013). Further studies on tBLG are shown in Fig. 27 with the AFM images obtained of a graphene monolayer [(a)] and of a twisted bilayer graphene tBLG [(b)] obtained by folding the graphene with the AFM tip. Compared to the Raman spectrum obtained in the folded region, a new sharp (as narrow as 4 cm^{-1}) band attributed to the R mode is observed close to 1383 cm^{-1} [see traces 1, 2, and 3 in Fig. 27(e)] in the folded regions, Fig. 27(d).

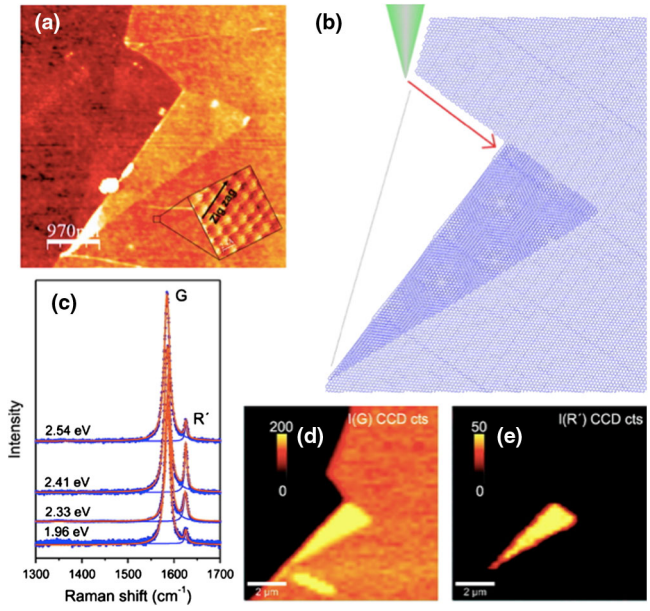

FIG. 26. (a) Atomic force microscope image of tBLG folded using the AFM tip as schematically shown in (b). The inset to (a) is the atomic resolution AFM image used for estimating the twist angle as 6°. (c) Raman spectra of tBLG shown in (a), using excitation laser energies at $E_{\text{laser}} = 1.96$, 2.33, 2.41, and 2.54 eV. Besides the first-order allowed G band, a peak centered at 1625 cm^{-1} is observed in (c). The absence of the disorder-induced D band (1350 cm^{-1}) provides evidence that the folded region has a low density of defects. The Raman image obtained from the same region shown in (a) for the G-band [(d)] and the R' band centered at 1625 cm^{-1} in (e). Adapted from Carozo *et al.*, 2011.

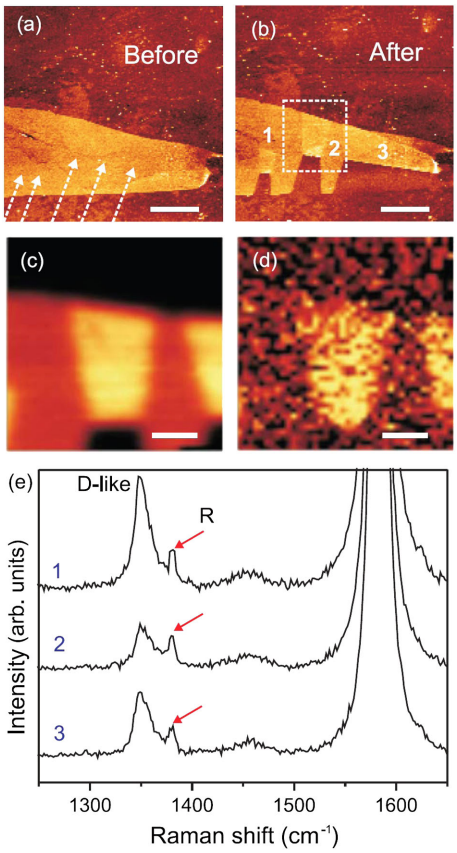

FIG. 27. (a) Atomic force microscopy image of monolayer graphene sitting on a Si/SiO_2 substrate. The white arrows stand for the directions over which the AFM tip was used in contact mode to scan the graphene sheet and to generate defects. (b) Three regions of folded graphene (labeled 1, 2, and 3) were obtained with the AFM tip. (c), (d) denote, respectively, the G-band and R-band map intensities for the boxed area in (b). (e) Raman spectra of tBLG obtained from regions 1, 2, and 3 defined in (b). The scale bars are 4 μm (a), (b) and 1 μm (c), (d). Adapted from Carozo *et al.*, 2013.

The activation of the rotation-induced R modes (at 1383 cm^{-1}) and the R' modes (at 1625 cm^{-1}) can be understood in terms of double-resonance features, Fig. 28 (Thomsen and Reich, 2000; Saito *et al.*, 2001). The magnitude of the rotational wave vector $\mathbf{q}(\theta)$, which connects the Brillouin zones of the two rotated layers can be written as (Carozo *et al.*, 2011)

$$q(\theta) = \frac{8\pi}{\sqrt{3}a}\sin(\theta/2). \tag{27}$$

The light scattering phenomena for activating the rotation-induced modes start with the absorption of a photon with energy E_L and wave vector $\mathbf{k}_L$ which generates an electron-hole pair with wave vector $\mathbf{k}_{\text{intra}}$ measured from the K point in Fig. 28(b). The static potential generated by the supercell structure allows a momentum transfer with rotational wave vector $\mathbf{q}(\theta)$, and the electron is elastically scattered to another

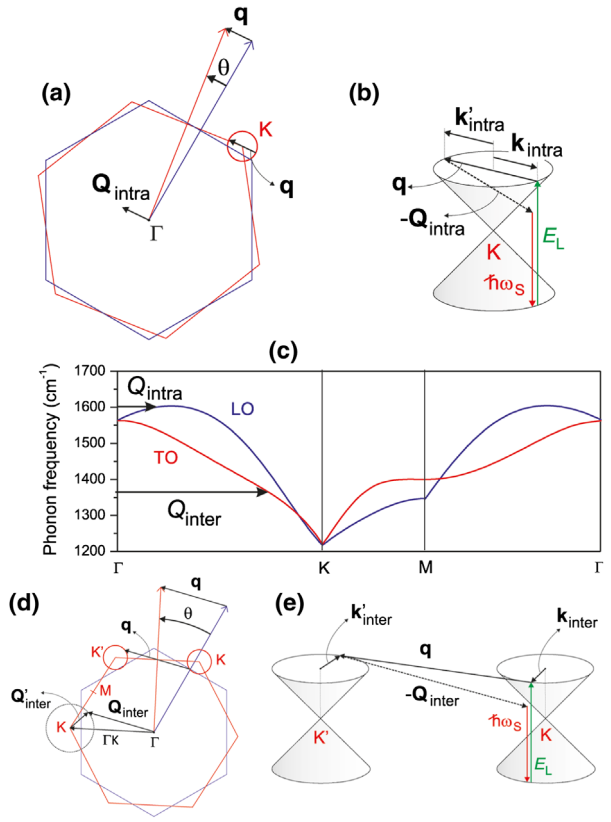

FIG. 28. (a) Brillouin zones for the top and bottom graphene layers, rotated from each other by a small twist angle θ. (b) The intravalley double-resonance process involving elastic electron scattering by the static potential generated by the moiré pattern. (c) High energy in-plane transverse (TO) and longitudinal (LO) optical phonon branches along high symmetry directions in the first Brillouin zone of graphene. Adapted from Venezuela, Lazzeri, and Mauri, 2011. The scattering phonon wave vectors $\mathbf{Q}_{\text{intra}}$ and $\mathbf{Q}_{\text{inter}}$ stand for scattering the electron or hole within the same valley and different valleys, respectively. The electron-phonon coupling is stronger for the LO and TO phonon branches near the Γ and K points, respectively, and relevant $\mathbf{Q}_{\text{intra}}$ and $\mathbf{Q}_{\text{inter}}$ wave vectors are outlined in (d). Adapted from Carozo *et al.*, 2011.

$\mathbf{k}$ point with wave vector $\mathbf{k}'_{\text{intra}} = -\mathbf{k}_{\text{intra}}$ belonging to the same isoenergy circle with radius $|\mathbf{k}_{\text{intra}}|$ [Fig. 28(b)]. A phonon with wave vector $\mathbf{Q}_{\text{intra}}$ is then created in the lattice, and the electron is inelastically scattered back to $\mathbf{k}_{\text{intra}}$ (or the hole is inelastically scattered to $-\mathbf{k}_{\text{intra}}$). These two events are classified as intravalley processes, since they connect two electronic states belonging to the same Dirac cone. Finally, the electron recombines with the hole, thereby emitting a photon with energy $\hbar\omega_S = E_L\hbar\omega$ (ω is the phonon frequency) and wave vector $\mathbf{k}_S$. This process gives rise to the R' Raman feature. The momentum conservation is satisfied when $\mathbf{k}_0 + \mathbf{k}_S = \mathbf{q}(\theta) - \mathbf{Q}_{\text{intra}}(\theta)$. Since $|\mathbf{k}_S|$ and the laser phonon momentum $|\mathbf{k}_0|$ are small compared to the size of the first Brillouin zone, the momentum conservation condition can be reduced to $\mathbf{Q}_{\text{intra}}(\theta) \simeq \mathbf{q}(\theta)$, as can be seen in Fig. 28(b). Therefore, the magnitude of $\mathbf{Q}_{\text{intra}}(\theta)$ is given by Eq. (27).

Figure 28(c) shows the TO and LO phonon branches for graphene along high symmetry lines in the Brillouin zone. For small angles ($\theta = 10°$), the wave vector $\mathbf{Q}_{\text{intra}}$ lies near the Γ point in the first Brillouin zone of graphene, close to the $\Gamma - K$ direction. Since the electron-phonon coupling is especially strong for the LO phonon branch close to the Γ point, the frequency $\omega_{R'}$ can be assigned to that branch. Notice that for larger values of $|\mathbf{Q}_{\text{intra}}|$ (larger θ angles), the R' band is unlikely to be observed experimentally, since the strength of the electron-phonon matrix element is drastically reduced for the LO phonon branch.

The intervalley scattering depicted in Fig. 28(d) is dominant for larger θ angles. For larger rotation wave vectors $\mathbf{q}(\theta)$, an electronic state with wave vector $\mathbf{k}_{\text{inter}}$ (measured from the K point) is connected to an electronic state with wave vector $\mathbf{k}'_{\text{inter}}$ (measured from the K' point), as shown in Fig. 28(e). From the momentum conservation selection rule, the wave vector of the phonon involved in the Raman process can be related to the rotational wave vector by $\mathbf{Q}_{\text{inter}}(\theta) \simeq \mathbf{q}(\theta)$. This wave vector lies near the K (or K') point in the first Brillouin zone, and it is more convenient to work with the phonon wave vector $\mathbf{Q}'_{\text{inter}}$ (measured from the K point), which can be evaluated as $\mathbf{Q}'_{\text{inter}}(\theta) = \mathbf{q}(\theta) - \mathbf{\Gamma K}$ [see Fig. 28(e)], with modulus

$$Q'_{\text{inter}}(\theta) = \frac{4\pi}{\sqrt{3}a}\sqrt{7 - 2\sqrt{3}\sin(\theta) - \cos(\theta)}. \tag{28}$$

By using the θ dependence for both Q'_{intra} and Q_{inter}, it is possible to map these values to obtain the frequencies $\omega_R(\theta)$ and $\omega_{R'}(\theta)$. The predicted values for $\omega_R(\theta)$ and $\omega'_R(\theta)$ thus obtained are plotted as solid and dashed lines, respectively, in Fig. 29.

We now discuss another unique phonon-activated mode occurring in tBLG which has been called the "D-like" band, Fig. 27(e) (Gupta *et al.*, 2010). The presence of a superlattice allows the use of Raman spectroscopy for investigating a new class of defects through the observation of the D-like band in graphene-type samples which would not be accessible otherwise. This band is called the D-like band because its frequency and dispersive behavior are both similar to what is observed for the well-known D band. However, the D-like band is activated only in the twisted region, even when the

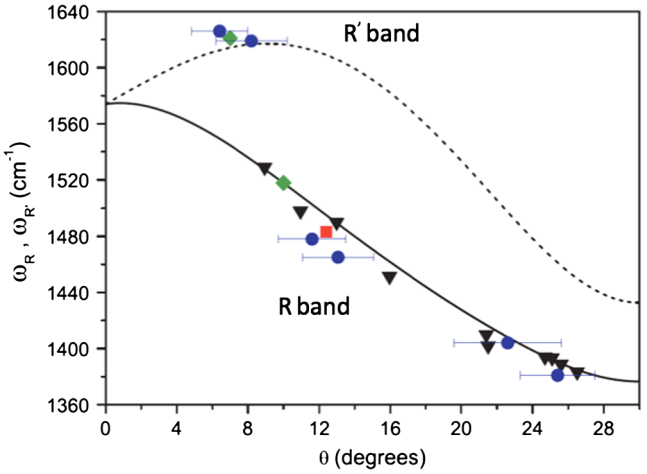

FIG. 29. R and R'-band frequency [$\omega_R(\theta)$ and $\omega'_R(\theta)$] as a function of the twist angle θ. The solid circles, squares, diamonds, and up triangles are experimental data. From Carozo *et al.*, 2013, (Havener *et al.*, 2012, Kim *et al.*, 2012, and Wang *et al.*, 2013, respectively. Adapted from Carozo *et al.*, 2013.

D band is absent in the unfolded region (Carozo *et al.*, 2013). Therefore, the D-like band cannot be attributed to edges or to vacancies, as can be done for the D band. It was proposed that the D-like band is not activated by the same type of short-range lattice defects as the D band, but rather by a combination of a periodic potential due to the tBLG superlattice with large θ angles (close to 30°) and of long-range defects such as Coulomb impurities, intercalated molecules, or strain.

D. Heterostructures

We now review recent works on how the properties of graphene can be preserved or even enhanced when graphene is used in heterostructures. The presence of another layer can in effect shield graphene from certain adverse environmental effects that significantly degrade its most desirable properties (Dean *et al.*, 2010). Under this heading, we also discuss how new, sometimes unexpected, functional materials can be obtained by mixing the properties of the separate, individual components (Terrones, Banhart *et al.*, 2002; Hunt *et al.*, 2013). One possible way of tuning and controlling the properties of sp^2 carbon materials for specific applications is by associating them with different materials in heterostructures. The 2D nature of graphene enables researchers to study two different types of heterostructures independently: in plane (horizontal) and out of plane (vertical).

Thus far, in-plane heterostructures involving graphene have been produced mainly with hexagonal boron nitride due to the small lattice mismatch (1.8%) of this wide band gap semiconductor (Z. Liu *et al.*, 2013). In-plane split closed-loop resonators were fabricated using graphene and h-BN. These devices have been shown to have properties similar to those obtained with copper but with the advantage of being one-atom thick and suitable for use in flexible devices (Z. Liu *et al.*, 2013).

Conversely, vertical graphene-based heterostructures, also referred to as van der Waals heterostructures, can be obtained with a wide range of different 2D materials, such as h-BN, MoS_2, WS_2, etc. (Ponomarenko *et al.*, 2011; Britnell *et al.*, 2013; Larentis *et al.*, 2014; Lin *et al.*, 2014), thereby providing a wide range of controllable properties and possible applications. For example, it was shown that when hexagonal boron nitride is stacked on top of graphene (Fig. 30), the lattice mismatch and the difference in orientation between the two materials gives rise to a moiré pattern-induced periodic potential that modulates the electronic structure of graphene (Yankowitz *et al.*, 2012). The wavelength λ of the periodic potential associated with the periodicity of the moiré pattern is then given by

$$\lambda = \frac{(1+\delta)a}{\sqrt{2(1+\delta)(1-\cos\phi)+\delta^2}}, \tag{29}$$

where $\delta \sim 1.8\%$ is the lattice mismatch between h-BN and graphene that is obtained using STM [Fig. 30(a)], ϕ is the relative rotation angle between the two lattices involved in the small mismatch, and a is graphene's lattice constant. The relative angle (θ) between the resulting moiré pattern and the angle ϕ of the h-BN–graphene lattice is defined in terms of

$$\tan\theta = \frac{\sin\phi}{(1+\delta)-\cos\phi}. \tag{30}$$

Figure 30(b) plots both the wavelength λ and the orientation angle θ of the moiré pattern as a function of the relative rotation angle ϕ between h-BN and graphene. Figures 30(c)–30(e) show STM topography images depicting the moiré patterns for three different rotation angles between the h-BN

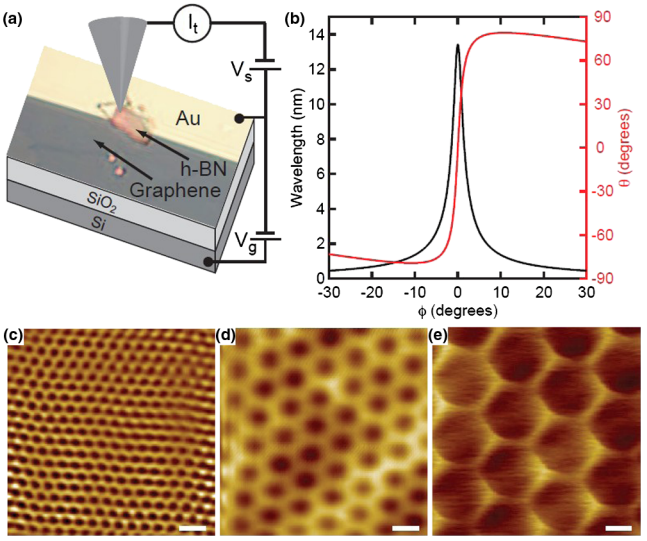

FIG. 30. (a) Schematic of the measurement setup showing the STM tip and an optical microscope image of a graphene and h-BN heterostructure where the graphene layer is on the top of the h-BN layer. (b) Superlattice wavelength and rotation as a function of the angle ϕ between the graphene and h-BN lattices. (c)–(e) STM topography images for three different moiré patterns with the wavelength of the periodic potential λ = (c) 2.4, (d) 6.0, and (e) 11.5 nm. The white scale bars in all images are 5 nm. Adapted from Yankowitz *et al.*, 2012.

and graphene lattices when the graphene layer is on top of the h-BN layer. The periodic potential was shown to be responsible for the appearance of extra Dirac cones associated with the hexagonal superlattice structure of the moiré pattern (Yankowitz *et al.*, 2012). Furthermore, Hunt *et al.* (2013) showed that the *AB* lattice symmetry breaking by the small lattice mismatch between h-BN and graphene in such heterostructures was capable of changing how the electrons move along the graphene plane turning it from a semimetal into a small gap semiconductor. These systems also showed Hofstadter butterfly effects on their two-terminal magnetoconductance measurements due to the moiré-like potential modulation.

The concept of stacked h-BN and graphene heterostructures was further extended into heterostructures consisting of two graphene flakes separated by a boron-nitride barrier layer (Mishchenko *et al.*, 2014). In such devices the electron tunneling between the two graphene electrodes is controlled by the difference in the angle of orientation between the two graphene flakes, opening up new possibilities for device application of twisted bilayer flakes as high-frequency oscillators.

Britnell *et al.* (2013) showed that heterostructures comprised of a thin layer of a transition metal dichalcogenide, such as WS_2, WSe_2, and MoS_2, sandwiched between two graphene layers can be used for highly efficient photovoltaic devices. In addition, they assembled a bipolar field-effect transistor whose functioning principle is based on graphene low density of states and its atomic thickness. This result was obtained by combining graphene and atomically thin BN or a MoS_2 layer in a hybrid system where the noncarbon layer acts as a vertical transport barrier (Britnell *et al.*, 2012).

Recently, the electronic properties of a heterostructure consisting of single-layer and bilayer phosphorene stacked on top of graphene were calculated using the DFT method (Padilha, Fazzio, and da Silva, 2015). Figure 31(a) shows the structure of the single-layer phosphorene/graphene system. The DFT calculations show that the interlayer distance ($d_{P/G}$) is optimized at 3.45 and 3.49 Å for single-layer and bilayer phosphorene systems, respectively. The calculations show that the electronic properties of both graphene and phosphorene remain essentially unchanged by the interaction between them, with the main difference being the increase of the phosphorene band gap by 0.1 eV for the single-layer phosphorene and 0.05 eV for the bilayer. It was also shown that it is possible to tune the position of the band structure of phosphorene relative to that of graphene through the application of an external electric field perpendicular to the system (Padilha, Fazzio, and da Silva, 2015). Figure 31(c) shows the evolution of both the band edges Δ_{CB} and Δ_{VB} as a function of the external electric field applied perpendicular to the graphene-phosphorene plane, z direction in Fig. 31(a). The band edge energies are defined as the energy difference between the phosphorene conduction (Δ_{CB}) or valence (Δ_{VB}) band edges and the energy of the graphene Dirac point; see Fig. 31(b). This allows the design of a system for tuning the Schottky barrier height between graphene and phosphorene and also for controlling the doping of phosphorene.

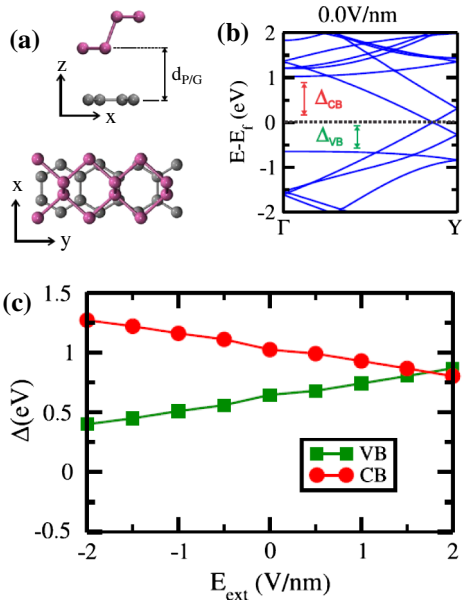

FIG. 31. (a) Side and top views of a single layer of phosphorene on top of graphene, where $d_{P/G}$ is the distance between the graphene and phosphorene layers. (b) Band structure of the phosphorene/graphene heterostructure near the Fermi energy. The energy differences between the energy of the graphene Dirac point and the band edges of the phosphorene conduction (Δ_{CB}) and valence (Δ_{VB}) bands are shown as a function of the wave vector from Γ to one corner of the Brillouin zone Y. (c) Evolution of the band edges, as a function of the field relative to the graphene Dirac point, for single-layer phosphorene. Adapted from Padilha, Fazzio, and da Silva, 2015.

E. Sculpting and coalescing

Defects in graphene can play both beneficial and detrimental roles, depending on the context of the intended graphene use (Vicarelli *et al.*, 2015). First, defects are essential in chemical and electrochemical studies, since they provide excellent bonding sites for the adsorption of atoms and molecules. However, defects also constitute a problem for applications in electronics, since the presence of defects has been found to significantly lower the charge carrier mobility and thus increase the resistivity of graphene (Stampfer *et al.*, 2009; Haskins *et al.*, 2011; Tsen *et al.*, 2012), with some specific exceptions such as when defects are organized in regular arrays for some intended use (Simonis *et al.*, 2002; Lahiri *et al.*, 2010; Yazyev and Louie, 2010).

Transmission electron microscopy (TEM) irradiation can trigger the nucleation of a number of defects, among which single vacancy and disclinations are the most likely varieties. For instance when a vacancy is formed in graphene, an external element can fill the void left behind by the knocked-off carbon atom, thereby forming an impurity defect. Another type of defect is the appearance of a zero-Burgers-vector dislocation, i.e., a pair of pentagon-heptagon disclinations with abutting heptagons, as formed by a single bond rotation (Lauginie and Conard, 1997; Yazyev and Chen, 2014). The control of defect formation and the possibility to reduce or eliminate the effect of existing defects are therefore essential for the development of graphene-based

electronics. Controlling the formation of defects enables engineering carbon nanostructures via welding, coalescing, and annealing as a promising area of nanoscale materials fabrication (Banhart, Kotakoski, and Krasheninnikov, 2011). New structures can be formed by the displacement of atoms, the reconstruction of both dangling bond and excited thermal states, and by the possibility of high structural strain release (Buongiorno Nardelli, Yakobson, and Bernholc, 1998).

The displacement threshold energy for sp^2 carbon is 15–20 eV (Banhart, 1999; Smith and Luzzi, 2001), depending on the curvature of the structure (Banhart, Li, and Krasheninnikov, 2005). Impinging electronic radiation in the vicinity of 100 keV can impart this threshold energy, rendering such displacements possible, for instance, in transmission electron microscopes (Banhart, Kotakoski, and Krasheninnikov, 2011). Furthermore, sp^2 carbon materials have demonstrated remarkable self-healing capabilities at elevated energies, which are usually the result of Stone-Thrower-Wales (STW) bond rotations, and such defects act to reduce the system energy, including the relief of structural stress (Banhart, Li, and Krasheninnikov, 2005; Robertson *et al.*, 2012). This self-healing is not observed under normal room-temperature conditions, since the energy barrier for a STW defect is on the order of 5–10 eV (Li, Reich, and Robertson, 2005). By combining the effects of the atomic displacements with the relaxation effects of annealing, systems can be transformed into new and stable configurations in a variety of morphologies (Krasheninnikov and Banhart, 2007). For instance, methods to form carbon nanotube junctions include soldering using ionic carbon irradiation (Wang *et al.*, 2005), catalyst-assisted chemical vapor deposition (Bandaru, 2007), and chemical methods such as pyrolysis (Lepro *et al.*, 2007). Many new or even exotic structures can be fabricated by the coalescence of elementary building blocks (Terrones *et al.*, 2000, 2002; Metenier *et al.*, 2002; Hernandez *et al.*, 2003; Endo *et al.*, 2004, 2006; Guan *et al.*, 2007; Nie *et al.*, 2010; Muramatsu *et al.*, 2013; Yang *et al.*, 2013; Zhao *et al.*, 2014). An early example of functional nanosystems built from elementary carbon nanotube building blocks is that of the welding of crossed nanotubes into a quasiorthogonal X junction, as has been shown experimentally (Terrones, Banhart *et al.*, 2002). More recent works include the development of techniques for the solution-mediated nanosoldering of carbon nanotube junctions, that is in principle scalable and compatible with mainstream manufacturing techniques (Do *et al.*, 2015). A number of models have been developed to explain the atomistic details of the annealing process, including molecular dynamics with localized heating (Meng *et al.*, 2006; Piper *et al.*, 2011), knock-on irradiation events (Jang *et al.*, 2004), or the reformation of dangling bonds around newly created vacancies (Terrones, Banhart *et al.*, 2002). Further, topology-driven methods have focused on finding the lowest energy paths using STW defects as the smallest units of disorder (Zhao, Smalley, and Yakobson, 2002; Zhao, Yakobson, and Smalley, 2002; Zhao, Lin, and Yakobson, 2003; Bullard and Meunier, 2013).

Significant progress has been reported regarding the TEM characterization of graphene edges (Meyer *et al.*, 2008b; Girit *et al.*, 2009; Huang *et al.*, 2009a; Jia *et al.*, 2009; Liu *et al.*, 2009; Warner, Ruemmeli, Ge *et al.*, 2009; Warner, Ruemmeli, Gemming *et al.*, 2009; Warner, Schaeffel *et al.*, 2009; Warner *et al.*, 2010). In addition to characterization, the electron beam can also enable the deposition of carbon onto graphene with high accuracy (Meyer *et al.*, 2008a, 2008b; Qi *et al.*, 2014). Fischbein and Drndic (2006) showed that suspended multilayer graphene sheets can be controllably nanosculpted into nanopores, nanobridges, and nanogaps with a few-nanometer precision by ablation using focused electron-beam irradiation in a TEM at room temperature. This type of fabrication of narrow constrictions in graphene layers is of great interest for electronic property engineering (Bunch *et al.*, 2005; Berger *et al.*, 2006; Chen *et al.*, 2007; Han *et al.*, 2007; Li *et al.*, 2008; Ponomarenko *et al.*, 2008; Stampfer *et al.*, 2008; Song *et al.*, 2011). For example, the modification of CVD-grown graphitic nanoribbon edges has been carried out by *in situ* Joule heating for the first time in 2009 (Jia *et al.*, 2009). In this experiment, a voltage is applied along a piece of graphitic nanoribbon suspended between two electrodes inside the TEM. Upon application of electron-beam irradiation, the graphitic nanoribbon becomes highly defective but when the voltage is increased, the material undergoes recrystallization and subsequent edge reconstruction due to the effect of significant resistive Joule heating, thereby yielding almost entirely achiral edges. This postprocessing approach shows that Joule heating inside an electron microscope provides a possible way of modifying rough edges in graphene nanoribbons and provides a further step toward using graphene nanoribbons for electronic device applications.

Complementary theories, based on first-principles calculations, have been offered to explain the details of the Joule heating mechanism in cleaning the edges, highlighting the role of electron irradiation induced by the TEM itself in the process (Cruz-Silva *et al.*, 2010; Engelund *et al.*, 2010). We note that under most typical experimental conditions, the edges of multilayered GNRs can recrystallize into bilayered structures, by forming covalent bonding with the adjacent edges, in a way similar to a zipping mechanism (Huang *et al.*, 2009b; Cruz-Silva *et al.*, 2010). This effect has been recently employed to fabricate atomically smooth freestanding graphene nanoribbon devices with superior electrical transport (Qi *et al.*, 2015). In this experiment, lattice disorder and bonded bilayer edges were observed for sub-10-nm GNR devices immediately after patterning. With increasing Joule heating, the GNR is continuously recrystallized while preserving the bonded bilayer edges, and the intrinsic ribbon conductance increases in spite of the reduced GNR width. The improvement in electron conductance was modeled as resulting from enhanced structural recrystallization, indicating the limitations of traditional patterning and etching procedures and the potential for Joule-heat recrystallization for property modifications. In this particular setup, nanosculpting typically leads to GNR structures with linked edges at various twist angles which can be used to control electron flow across the device. Other methods of patterning multilayer graphene are expected to leave the edges exposed and susceptible to bonding. One consequence of recrystallization induced by heating (either external or Joule) is the systematic formation of bonded edges (Liu *et al.*, 2014). Any open edge in a bilayer or a multilayer graphene sheet will fuse with the closest free edge available. For

electrochemical studies, this could represent a disadvantage because there are no dangling bonds available for chemical functionalization. On the other hand, bilayer GNRs with closed edges could, in theory, have a finite band gap (up to 0.25 eV), depending on the twist angle between the two layers (Lopez-Bezanilla *et al.*, 2012; Qi *et al.*, 2015).

V. TRANSPORT PROPERTIES

In this section, we highlight current understanding and recent progress in describing electron transport in sp^2 carbon nanostructures and how recent investigations provide insight applicable to the development of novel nanomaterials and devices. This text does not aim at providing a detailed picture of all aspects of the science of transport properties in all types of carbon nanostructures. However, abundant references are provided throughout the text and the interested reader is referred to reviews available elsewhere (Avouris, Chen, and Perebeinos, 2007; Charlier, Blase, and Roche, 2007; Biercuk *et al.*, 2008; Cresti *et al.*, 2008; Castro Neto *et al.*, 2009; Dubois *et al.*, 2009; Peres, 2010; Biswas and Lee, 2011; Das Sarma *et al.*, 2011; Foa Torres, Roche, and Charlier, 2014).

A. Graphene

The simple technique of isolating bulk graphite into individual *graphene* sheets was made readily available to the broad research community in 2004, marking the starting point of intense nanocarbon research in both experimental and theoretical directions (Novoselov *et al.*, 2004). One crucial achievement reported in the 2004 seminal paper is the possibility of gating monolayer graphene to continuously control the Fermi level of graphene, thereby continuously changing graphene from a *p*-type to an *n*-type conductor with the Dirac point marking the separation point between the two transport regimes. Many experiments have since then focused on investigating the electronic transport properties of graphene, and how the electronic properties relate to other physical properties. The control over the number of graphene layers making up a transistor devise is a topic of much research and development. This technique consists of sputter-coating graphene materials (such as graphene itself, graphene oxides, CVD-grown graphene, and micromechanically cleaved graphene) with Zn followed by an acid treatment to remove one graphene layer at a time in a highly controlled manner (Dimiev *et al.*, 2011). Graphene is an attractive material for electronic devices because of it high mobility, along with other outstanding and unique physical and chemical properties. For instance, in a pioneering research work, spin transport and Larmor spin precession were observed over a micrometer distance in graphene using a nonlocal spin valve where the graphene sheet is placed in contact with ferromagnetic cobalt electrodes This allowed Dimiev *et al.* (2011) to estimate a spin relaxation length between 1.5 and 2 mm at room temperature (Tombros *et al.*, 2007). Further, current saturation was observed in zero band gap graphene field-effect transistors in a top-gate geometry (Meric *et al.*, 2008). A vertical graphene-based *hot-electron transistor* with an on-off ratio as high as 10^5 was developed recently where the transport of hot electrons proceeds across the ultrathin graphene while their filtering occurs through a built-in energy barrier (Zeng *et al.*, 2013). Single-layer graphene, as a zero-gap semimetal, is not directly adequate as a channel for transistor application. A number of methods discussed here and presented below have been devised to address this issue. For instance, the inversion symmetry in graphene can be broken in bilayer graphene in the presence of a vertical displacement and induces the opening of a band gap. This effect can be further controlled by the presence of chemical molecular doping for single and dual gate modulation, as demonstrated for the control of the on-off ratio as well as the position of the Fermi energy level in the opened gap in order to devise transistors with tunable Dirac points for functional devices. This can be achieved with a number of doping molecules, as demonstrated by different research groups (Yu *et al.*, 2011; Park *et al.*, 2012).

1. Mobility

The concept of carrier mobility is a semiclassical notion that applies only in the diffusive regime and is no longer valid when transport is ballistic or quasiballistic (e.g., when transport is governed by contact resistance effects). In the diffusive regime, the intrinsic electron mobility is a measure of how easily electrons move in a given material before being scattered, and increasing the carrier mobility is one method of making semiconductor devices smaller and faster.

Two important factors contribute to this increased mobility in graphene: low phonon scattering and a vanishing effective mass at the Dirac point. Graphene's structure consists of two atoms per unit cell in a honeycomb lattice, where carbon atoms are arranged according to a two-dimensional hexagonal motif (Fig. 1). This simple arrangement makes a description of its electronic structure possible to a first approximation when described within a tight-binding model (Saito, Dresselhaus, and Dresselhaus, 1998). Most notably, this approach reproduces the most salient characteristic of a linear $E(k)$ relation around the K and K' points of the first Brillouin zone, where the valence and conduction bands meet at the Dirac point. It is the graphene linear electronic band-structure diagram close to the Dirac point that confers to graphene its unusual electronic properties and a room-temperature in-plane conductivity higher than any other known material. Theory indicates that graphene's intrinsic charge-carrier mobility μ can exceed 200 000 $\mathrm{cm}^2/\mathrm{Vs}$ at room temperature (Akturk and Goldsman, 2008; Chen *et al.*, 2008; Morozov *et al.*, 2008), which is the absolute record of any reported material [i.e., it significantly surpasses that of Si ($\mu \sim 1500$ $\mathrm{cm}^2/\mathrm{Vs}$) or semiconductors such as AlGaAs/InGaAs ($\mu \sim 8500$ $\mathrm{cm}^2/\mathrm{Vs}$)].

Because of this local linear relation for the low-lying energy levels of graphene, the electrons behave as massless Dirac fermions, leading to the onset of Klein tunneling (where an electron passes through a potential barrier with a transmission probability of unity). Klein tunneling in graphene is a quantum phenomenon unique to massless Dirac fermions and it was first observed by Katsnelson, Novoselov, and Geim (2006). It also manifests itself in metallic carbon nanotubes (Ando, Nakanishi, and Saito, 1998). Klein tunneling was also theoretically predicted to occur in graphene *p*-*n* junctions

(Cheianov and Fal'ko, 2006), and was experimentally confirmed (Huard *et al.*, 2007).

As a result of its high carrier mobility, graphene is characterized by a high Debye temperature T_D of about 2100 K (Pop, Varshney, and Roy, 2012), where T_D is the temperature associated with a thermal energy $k_B T = \hbar\omega_D$ (where k_B is the Boltzmann constant and $\hbar$ is Planck's constant divided by 2π) corresponding to the vibrational frequency ω_D of the highest normal mode. In common materials, ω_D provides a measure of the level of electron scattering by phonons (i.e., a high Debye temperature T_D corresponds to a material with reduced scattering). However, Efetov and Kim experimentally showed that owing to graphene's very small Fermi surface, the boundary between high-temperature and low-temperature behaviors of the electron-phonon scattering in graphene is not set by the Debye temperature, as in conventional metals which have a large Fermi surface, but rather by the Bloch-Grüneisen temperature, the characteristic electronic energy scale for metals with small Fermi surfaces, such as graphene (Hwang and Das Sarma, 2008; Efetov and Kim, 2010), and as discussed by Fuhrer (2010); see Fig. 32.

Hofmann (2011) discusses the apparent contradiction between these properties and the direct application of the semiclassical definition of the effective mass to graphene. Indeed, solid-state physics textbooks state that the effective mass is expressed by $m^* = \hbar^2(d^2E/dk^2)^{-1}$ and this expression would indicate that graphene's linear dispersion relation should yield an infinite effective mass rather than a zero mass. Classically, an infinite mass would indeed make it impossible for electrons to be accelerated by an external field, in stark contrast with experimental observations for graphene. Matters are made even more confusing by the fact that the electrons in graphene are often called *massless*, which is a drastic

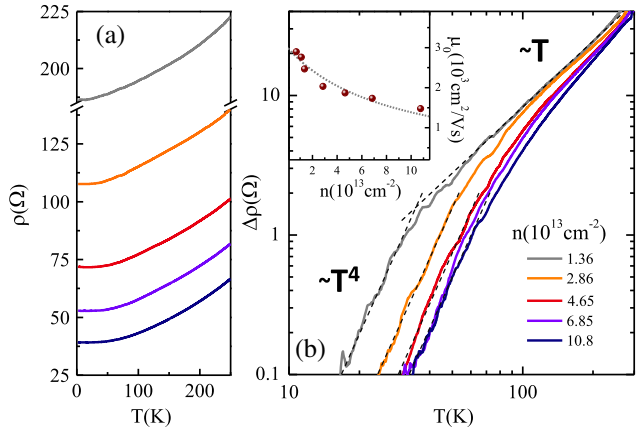

FIG. 32. Temperature (T) dependence of the resistivity $\rho(T)$ for different charge-carrier densities in graphene. The measured sample resistivity increases linearly with temperature T in the high-temperature limit, thereby indicating that a quasiclassical phonon distribution is responsible for the electron scattering. As T decreases, the resistivity decreases more rapidly, following a T^4 dependence. This low-temperature behavior is described by a Bloch-Grüneisen model, taking into account the quantum distribution of the two-dimensional acoustic phonons in graphene, as explained by Fuhrer (2010). From Efetov and Kim, 2010.

departure from what the semiclassical formula for m^* appears to suggest.

As pointed out by Ariel and Natan (2012), the key issue with the apparent contradiction is that the semiclassical definition of the effective mass is inspired by a parabolic band dispersion. These authors suggested a cure to this problem by introducing an alternative expression for the effective mass. The problem of the diverging mass is resolved by using $m^* = \hbar^2 k(dE/dk)^{-1}$, which they derived using semiclassical arguments. From this formula it follows that exciting an electron from the valence band to the conduction band generates an electron-hole pair that can be seen as a particle and its antiparticle, respectively, and all of the excitation energy goes into the kinetic energy of these two particles since their rest mass vanishes. This viewpoint allows one to reconcile the apparent paradox between the effective mass obtained from the textbook definition and the experimental observations. It is also worth mentioning that while the graphene electronic properties can be described using mathematical expressions borrowed from relativistic theory, electrons in graphene are not intrinsically relativistic and the formalism that has been used to describe them is merely chosen for mathematical convenience.

2. Suspended versus substrate-deposited graphene

Many experiments have focused on investigating the electronic transport properties of graphene. The field of electronic transport in graphene and graphene-related materials is rich and is rapidly developing and as pointed out, the modest aim of this section is only to provide a bird's-eye overview of the present state of the field. While most of the early experimental electrical measurements were performed on graphene deposited on Si/SiO^2 substrates, a number of other studies used other substrates, including hexagonal boron nitride (Dean *et al.*, 2010), or even freestanding graphene (Bolotin, Sikes, Jiang *et al.*, 2008). For instance, the presence and choice of a substrate can have a profound influence on the measured properties of few-layered materials. The record high mobilities predicted by theory are difficult to achieve experimentally, due to limitations imposed by extrinsic and intrinsic scattering mechanisms. The highest reported experimental mobility values were obtained on suspended devices (Bolotin, Sikes, Jiang *et al.*, 2008; Du *et al.*, 2008), reaching 120 000 m^2/Vs at 240 K (Bolotin, Sikes, Hone *et al.*, 2008). Mayorov *et al.* (2011) further improved the properties of graphene-boron-nitride heterostructures by showing that h-BN-encapsulated graphene possesses robust ballistic transport with a large negative transfer resistance. This system exhibits a measured low-temperature mean-free path exceeding 3 μm at low T, showing that the conductivity along the sample is no longer limited by the graphene bulk value but rather by diffusive scattering at the sample boundaries. Many of the reported data indicate that careful sample preparation, including current annealing prior to transport measurement, is critical to achieve high mobility values (Moser, Barreiro, and Bachtold, 2007). We note that CVD-grown graphene samples deposited on h-BN with a dry method also display ballistic transport on micrometer length scales (Calado *et al.*, 2014).

The mobility value of suspended graphene is about an order of magnitude larger than values typically reported for

graphene on a substrate (Fig. 33). In suspended graphene, carrier scattering is mainly governed by the existence of flexural phonon modes, which yield a tenfold reduction in mobility relative to other phonon modes. The flexural mode is an out-of-plane transverse acoustic mode, also called the bending or *ZA* phonon mode (Jiang *et al.*, 2015). It can be quenched by the presence of a substrate or the application of tension. This latter approach, which does not add significant scattering for a modest applied tension, can restore large mobility values close to the theoretical predictions (Castro *et al.*, 2010). Suspended graphene devices also offer the possibility to controllably screen Coulomb scatterers by changing the dielectric constant of the materials surrounding graphene (Newaz *et al.*, 2012). Performance of graphene electronics is limited by contact resistance associated with the metal-graphene interface and much research has been devoted to improve control over the contact effect. For example, carrier injection was shown to be enhanced in graphene devices when cuts normal to the channel are formed in graphene within the contact region to improve bonding between the contact metal and carbon atoms at the graphene cut edges. This method has shown to yield a 32% reduction in contact resistance in Cu-contacted, two-terminal devices and a 22% reduction in a top-gated graphene transistor with Pd contacts, when compared to conventionally fabricated devices (Smith *et al.*, 2013).

3. Disorder

As in any metallic system, graphene's electronic mobility is strongly affected by disorder. In addition to perturbations caused by substrate effects, disorder in graphene can originate from adsorbed atoms or molecules, impurities [e.g., charges trapped in the oxide, chemical impurities], extended defects

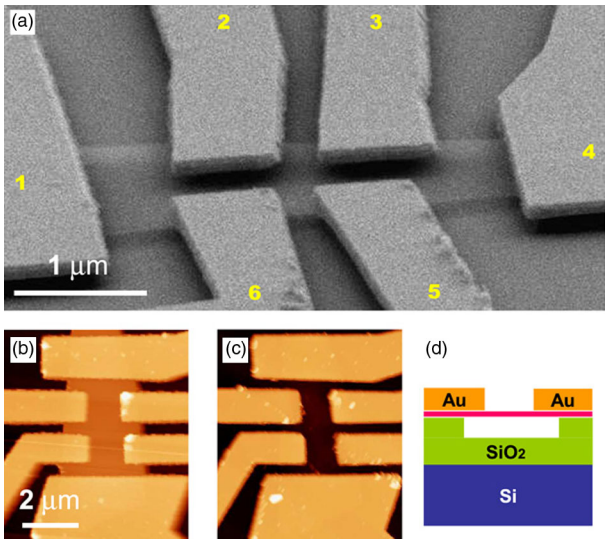

FIG. 33. (a) Off-side view of a scanning electron microscopy (SEM) image using a suspended six-probe graphene device. (b) Atomic force microscopy image of the suspended device before the measurements, and (c) after the measurements with graphene removed by a short oxygen plasma etch. (d) Side view of the device (schematic). The doped silicon gate, partly etched SiO_2, suspended single-layer graphene and Au/Cr electrodes are shown, respectively, in blue, green, pink, and orange (from bottom to top). The white rectangle denotes vacuum. From Bolotin, Sikes, Jiang *et al.*, 2008.

(i.e., wrinkles, folds), and topological defects [vacancies, edge disorder, Stone-Thrower-Wales types of defects (Stone and Wales, 1986)]. We note that when present in large quantities in an orderly fashion, extended defects in graphene can even act as one-dimensional conducting channels (Simonis *et al.*, 2002; Lahiri *et al.*, 2010) and it is the physical impact of the environment that is created by the defect that becomes relevant rather then the surrounding defect-free graphene itself. The presence of random rippling (Fasolino, Los, and Katsnelson, 2007; Meyer *et al.*, 2007; Vazquez de Parga *et al.*, 2008; Bao *et al.*, 2009; Schoelz *et al.*, 2015) makes the graphene lattice typically far from planar. This effect is even more pronounced for defects present at the edges, where rough edges lead to a number of scientifically interesting morphological features, such as scrolling (Shenoy *et al.*, 2008). Of course, most defects and imperfections in graphene are thermodynamically unfavorable but are usually present in typical actual samples, due in large part to the sample preparation methods and to sample exposure to the environment. All these effects strongly affect the measured electronic transport properties in undesirable ways. To some extent, contamination can be controlled using annealing processes at high temperature in ultrahigh vacuum, or, at low temperature, by electrical current-induced cleaning (Moser, Barreiro, and Bachtold, 2007).

In all nanostructures, scattering processes are critically dependent on the spatial range of the disorder potential and the associated effect on the underlying sublattice symmetries (Cresti *et al.*, 2008). For instance, for massless Dirac fermions, a long-range scattering potential strongly reduces the intervalley scattering probability between the two nonequivalent Dirac points. In one-dimensional cases, such as armchair CNTs, this leads to a full suppression of backscattering as demonstrated by Ando, Nakanishi, and Saito (1998) and by White and Todorov (1998). In contrast, short-range disorder can lead to intravalley and intervalley scattering events between the two Dirac points in graphene, causing stronger backscattering and localization effects. For example, disorder in the quantum coherent regime can yield localization behavior as reported by Flores and coworkers who showed evidence of weak and strong Anderson localization regimes in carbon nanotubes (Gomez-Navarro *et al.*, 2005; Flores *et al.*, 2008) while Lherbier *et al.* (2011) predicted Anderson transitions in graphene.

Finally, we note the recent study which established that defect-induced localization in graphene can be tuned by using an accelerated helium ion beam to insert low-density defects in the graphene lattice, as a means to modulate the electronic current by the resulting random potential modulation (Nakaharai *et al.*, 2013).

We conclude this section on the transport properties of graphene by noting that much research is underway to develop means to use graphene in actual applications. We mainly focused on the use of single- and few-layer graphene here, but much research is also devoted to other forms of graphene, including composites and networks. Graphene sheets and composites often suffer from poor electrical and thermal conductivity due to the low quality of interconnections between individual components of the composites. For example, the direct synthesis of highly conductive three-dimensional *graphene foam* macrostructures by template-directed CVD was reported. This macroscopic graphene-based material consists of

an interconnected flexible network of graphene which provides a highly conductive channel for fast charge carrier transport, with high potential as flexible, foldable, and stretchable conductors (Chen *et al.*, 2011).

B. Carbon nanotubes

Soon after their first unambiguous observation by Iijima in 1991, carbon nanotubes were touted as the most promising materials for future technologies, in particular, for further scaling down of the channel length in the common use of field-effect transistors in electronics (Ebbesen *et al.*, 1996). However, any technology that aims to compete with conventional approaches must also display significant benefits and distinct advantages. In that respect, carbon nanotubes have been among the most cited candidate materials for future nanoelectronics, owing to their intrinsic structural and electronic properties.

The unique features of carbon nanotubes that distinguish them from other nanostructures, including conventional semiconductors and semiconductor nanowires, are their nearly perfect stoichiometry and the associated relative ease to create carbon nanotubes with a low density of defects. Carbon nanotubes have versatile properties, being metallic or semiconductor depending on the details of the nanotube chirality and diameter. However most techniques of mass production yield a broad distribution of nanotube types. This versatility is both a benefit as stated earlier and a curse, since the inhomogeneity of behavior in samples typically obtained using large-scale synthesis methods yields structures with highly varying characteristics. Highly effective methods have been developed to isolate specific metallicities and chiralities such as using an alternating current dielectrophoresis (Krupke *et al.*, 2003; Sarker, Shekhar, and Khondaker, 2011) or using density gradient ultracentrifugation (DGU) (Arnold *et al.*, 2006; Ghosh, Bachilo, and Weisman, 2010). DGU has proven to be scalable, leading to metallic and semiconducting enriched SWNT samples being commercially available since 2007 (Green and Hersam, 2007). The versatility of DGU has also allowed it to be used for the purification and sorting of a range of 2D materials including graphene (Green and Hersam, 2009), transition metal dichalcogenides (Kang *et al.*, 2014), boron nitride (Zhu *et al.*, 2015), and black phosphorus (Kang *et al.*, 2016).

Recent efforts have highlighted the possibility to fully control the structure of the synthesized nanotubes, using a bottom-up approach but this technique has not been scaled up to large nanotube production yet (Sanchez-Valencia *et al.*, 2014). In addition to the practical difficulties of isolating nanotubes with well-defined properties, the integration of carbon nanotube devices with macroscopic electrodes constitutes an even more formidable challenge. However, it is clear that the physical phenomenon taking place at the metal-nanotube contact is crucial for device operations, especially in the pertinent quantum mechanical regimes.

1. Intrinsic transport properties

Turning to fundamental transport properties of carbon nanotubes, in a typical transport measurement, a single-wall carbon nanotube is directly connected to two metallic contacts (source and drain), and capacitively coupled to a third terminal (gate) that can be used to control the charge density of the nanotube. The actual measurements consist of applying an electrostatic potential difference between the various terminals and recording the source-drain current. Many reports have provided information on transport measurements in carbon nanotube devices since the first experimental reports devoted to their transport properties (Bockrath *et al.*, 1997; Martel *et al.*, 1998; Tans, Verschueren, and Dekker, 1998; Tans and Dekker, 2000). Carbon nanotubes are one dimensional and, in the ballistic regime, obey the Landauer formula, which states that the conductance of a quasi-1D system is proportional to the transmission probability of each 1D electronic band (Landauer, 1970). In practice, a conductance measurement yields a transmission function with a broadening factor related to the finite temperature under which the experiment is conducted, as well as the lifetime of the excited state.

As in any moderate band gap semiconductor (e.g., $\lesssim 1$ eV), when the Fermi energy is in the band gap, the electrical transport is determined by the tail of the Fermi function at finite temperature. However, typical measurements do not directly yield the intrinsic transmission properties of the nanotubes. The actual transport measurements instead provide a measure of the transmission across the nanotube together with its contact to the external electrodes (in this review, the word *device* is reserved for the entire nanotube and contact entity). Ballistic transport occurs for perfect contacts and in this case, the total conductance is precisely $4e^2/h$ as expected for each fourfold degenerate 1D subband present at the Fermi energy of metallic nanotubes. Experiments show that this quantized value is often observed in metallic nanotubes even at room temperature (Kong *et al.*, 2001; Liang *et al.*, 2001). There is a corresponding fourfold degeneracy at the Fermi level of semiconducting nanotubes, but experiments on semiconducting devices usually yield significantly smaller conductance values than the theoretical value of $4e^2/h$ unless the measurements are performed at low temperatures (Kong *et al.*, 2001; Javey *et al.*, 2003).

Reasons for obtaining measured conductance properties inferior to the theoretical predictions can originate from the resistance inside the nanotube itself or from its contacts to external circuitry. At low temperatures, coherence and Coulomb blockade effects can dominate transport which is thus governed by quantum mechanical effects. In the absence of coherence, the resistance of a uniform nanotube can be expressed as $R_{\text{tube}} = (h/4e^2)L/l$ for a nanotube of length L in the diffusive scattering regime described by an electron mean-free path $l \ll L$ for momentum relaxation. Additionally, contact (extrinsic) resistance needs to be added to the intrinsic tube resistance in an actual measurement. Electrical nanoprobing can be used to monitor the potential drop along the nanotube to discern the difference between the intrinsic and extrinsic contributions to the measured resistance (Bachtold *et al.*, 2000; Tans and Dekker, 2000; Heinze *et al.*, 2002; Javey *et al.*, 2003; Yaish *et al.*, 2004; Freitag *et al.*, 2007; Varghese *et al.*, 2010; Jalilian *et al.*, 2011).

2. Scattering by disorder

Disorder in the carbon nanotube channel yields profound changes in electron transmission across a conducting channel.

Disorder arises from lattice defects: vacancies and topological defects (Meunier and Lambin, 2000), impurity atom substitutions (Cruz-Silva *et al.*, 2009; Sumpter *et al.*, 2009; Cruz-Silva, Lopez-Urias *et al.*, 2011), heterojunctions between nanotubes of different diameter or chirality (Charlier, Ebbesen, and Lambin, 1996; Chico *et al.*, 1996; Lambin and Meunier, 1999; Yao *et al.*, 1999), electrostatic potential fluctuations due to a random distribution of charges in the substrate, molecules adsorbed on the nanotube, adsorbed processing residues, or mechanical deformations (Bernholc *et al.*, 2002).

Experimentally, how disorder affects transport properties can be elucidated by evaluating the nanotube carrier mean-free paths from conductivity measurements or by direct spatial imaging. Low-temperature measurements of metallic nanotubes routinely show mean-free paths that are many micrometers long, as determined from their measured conductance (Bockrath *et al.*, 1997; Kasumov *et al.*, 1999), from measured sizes of quantum dots (Bockrath *et al.*, 1997; Tans *et al.*, 1997), and from scanning probe measurements (Bachtold *et al.*, 2000; Woodside and McEuen, 2002). Semiconducting tubes often show stronger sensitivity to disorder and shorter mean-free paths at room temperatures and above (Tans *et al.*, 1997; Martel *et al.*, 1998), even if μm-long mean-free paths at low temperatures have also been reported (Shim *et al.*, 2001; Rosenblatt *et al.*, 2002; Durkop *et al.*, 2004; Li *et al.*, 2004; Zhou *et al.*, 2005).

Disorder affects both electrical and thermal transport in nanotubes in two distinct ways depending on the spatial scale, owing to two distinct backscattering processes—nanotubes have two degenerate dispersion branches originating from the K and K' points in the Brillouin zone. Because the two branches have left- and right-moving electrons, backscattering can occur either between the two branches or within the same branch. The first scattering process involves a large momentum transfer and occurs only for an atomically sharp disorder center. The second process is caused by long-range disorder and involves small momentum transfer. Reports have established that due to the symmetries of the electronic wave functions metallic nanotubes are significantly affected only by short-range disorder, whereas semiconducting tubes are affected by both short- and long-range disorder (Ando and Nakanishi, 1998; McEuen *et al.*, 1999). Long-range disorder, e.g., from the electrostatic or mechanical interaction of a nanotube with the substrate, can be significant. This is particularly true for semiconducting tubes with low carrier densities. This effect can be mitigated by preparing the nanotube in a suspended geometry but this technique is not practical for routine experiments and it is performed only in special situations when an accurate measurement is needed (Biercuk *et al.*, 2008).

In clean, high-quality metallic carbon nanotubes at room temperature, the electron-phonon scattering process dominates. Scattering by acoustic phonons plays a major role in determining the resistance at small source-drain biases (Kane *et al.*, 1998; Appenzeller *et al.*, 2001; Park *et al.*, 2004). In contrast, scattering by optical and zone-boundary phonons imposes a limit to the maximal current carried at large bias potentials (Yao, Kane, and Dekker, 2000; Javey *et al.*, 2004; Park *et al.*, 2004).

The identification of the scattering mechanism is usually performed using temperature-dependent measurements, since different scattering phenomena exhibit unique scaling behaviors as a function of temperature. Experiments have shown that phonon scattering limits the ultimate performance of semiconducting nanotube devices (Zhou *et al.*, 2005), showing that the on-state resistance increases linearly with temperature, indicative of scattering by acoustic phonons, whose density also grows linearly with temperature. Measurements of the mobility show that it varies quadratically with the diameter of the nanotube, in agreement with theoretical predictions (Suzuura and Ando, 2002; Perebeinos, Tersoff, and Avouris, 2005), due to the concomitant decreases of the effective mass and the scattering rate with increasing nanotube diameter. The mobilities of clean semiconducting nanotubes are very high (Durkop *et al.*, 2004), with reported values of 15 000 $\mathrm{cm}^2/\mathrm{Vs}$ at room temperature, reaching values beyond 100 000 $\mathrm{cm}^2/\mathrm{Vs}$ at $T = 50$ K. The high mobilities, long mean-free paths, and large current-carrying capacities of carbon nanotubes have inspired many groups to explore a broad spectrum of electronic, high-frequency (Steiner *et al.*, 2012; Wang *et al.*, 2012), and optoelectronic (Nanot *et al.*, 2012) applications of nanotubes, including high-performance transistors (Franklin, Luisier *et al.*, 2012), among others.

3. Role of contacts with electrodes: Schottky barriers

Two types of barriers can be formed at the metal-nanotube interface. First, a barrier can appear due to an imperfect interface between the contact metal and the nanotube. This phenomenon depends on the chemical composition of the metal. Early studies indicated that contact with an Au or Pd electrode yields quasiperfect transmission, due to the favorable alignments of the electronic states at the interface (Javey *et al.*, 2003). Second, a Schottky barrier can form at the interface of a metal and a semiconducting nanotube, with properties fully governed by the band alignment at the interface. The heights of the Schottky barriers for hole and electron injection are (Leonard and Tersoff, 2000)

$$\phi_p^{\mathrm{SB}} = \phi_{\mathrm{NT}} + E_g/2 - \phi_{\mathrm{M}}, \tag{31}$$

$$\phi_n^{\mathrm{SB}} = \phi_{\mathrm{M}} - \phi_{\mathrm{NT}} + E_g/2, \tag{32}$$

where ϕ_{M} and ϕ_{NT} are the work functions of the metal and of the nanotube, respectively, and E_g is the nanotube band gap. Depending on where the Fermi level of the metal lies with respect to the midgap of the nanotube, a Schottky barrier for either an n-type or a p-type carrier will develop, unless the Fermi level is located exactly at midgap, in which case a Schottky barrier appears for both types of carriers.

A series of experiments established the importance of Schottky barriers in nanotube devices. For instance, one experiment showed that the work function of the contact metal can be controlled by the adsorption of oxygen (Heinze *et al.*, 2002), thereby effectively transforming n-type conduction into an ambipolar operation, and eventually to p-type conduction upon increased oxygen absorption (Heinze *et al.*, 2002). Many metals have been investigated for contacts to show that large work function metals make good p-type contacts and low work function metals make better n-type

contacts (Heinze *et al.*, 2002; Cui *et al.*, 2003; Javey *et al.*, 2003; Chen *et al.*, 2005; Pop, 2008; Matsuda, Deng, and Goddard, 2010; Chai *et al.*, 2012).

Development of carbon nanotube in field-effect transistors remains a topic of continued interest, especially since challenges with contact resistance still need to be overcome. For instance, it was recently suggested that most optimal contact metals at long contact lengths (Pd) might not be the best for scaled devices while the newly considered Rh yields the best scaling behavior (Franklin, Farmer, and Haensch, 2014). The role of contacts with carbon nanosystems is also evidenced by the use of carbon electrodes in molecular electronics applications. To this effect, new fabrication methodologies are constantly being developed to produce functional carbon electrode-molecule junctions for the development of practical molecular devices, thereby offering a reliable platform for molecular electronics and the promise of a new generation of multifunctional integrated circuits and sensors. These devices use nanogapped carbon nanomaterials (such as single-walled carbon nanotubes and graphene), as point contacts formed by electron-beam lithography and precise oxygen plasma etching. The current state of this very promising field was recently reviewed (Jia *et al.*, 2015).

4. Electronic transport: Quantum phenomena

The transport properties described thus far can be understood from a semiclassical description of electron dynamics using an appropriately described band-diagram framework, akin to conventional semiconductor band theory. However, at low temperature, this description breaks down due to the manifestation of a number of quantum effects. Similar to the physics of small-width GNRs, the energy scales of quantum phenomena in 1D systems, such as carbon nanotubes, increase with decreasing system size, and the low-temperature regime is more easily reachable compared to typical semiconducting systems. This also accounts for the fact that carbon nanotubes have constituted a perfect test bed for quantum transport as early as the mid-1990s. Manifestations of quantum transport phenomena include quantized charge transport (i.e., Coulomb blockade) and coherent transport leading to interference effects, among others (Biercuk *et al.*, 2008). Quantum effects can also arise from the peculiar interactions of charge carriers with the electrodes, with the emergence of many-body effects, such as the Kondo effect [either related to the spin degree of freedom in a confined nanotube hybridized with the continuum of states in the metallic leads (Nygard, Cobden, and Lindelof, 2000) or in single-molecule transistors, where a divanadium molecule serves as a spin impurity (Liang *et al.*, 2002)] or as charge carriers or spin coupling with superconductivity in the leads (Morpurgo *et al.*, 1999; Shim *et al.*, 2001). As previously discussed, van Hove singularities are electronic signatures of one-dimensional systems and renewed interest in them has recently been brought to light by a study where it was shown that they might be responsible for interference patterns of the electronic wave functions. An anomalous conductance increase was also reported. It was ascribed to the possible signature of Cooper pairs formation and the onset of superconductivity (Yang *et al.*, 2015). In addition, a number of effects also arise from the particularly intense electron-electron correlation in one dimension, as expressed, for instance, in the power-law dependence of the conduction on temperature and source-drain voltage. Figure 34 highlights the crossover between a number of transport regimes as observed by the H. Park group (Liang, Bockrath, and Park, 2005). In addition to the phenomena mentioned, we now present a number of specific examples such as the manifestation of ballistic transport, Luttinger liquid behavior, and quantum dot effects to illustrate the richness of such phenomena in carbon nanotubes.

As discussed at the onset of this section, ballistic transport of carriers is a quantum regime characterized by electrical resistance that does not depend on the channel length. Ballistic electron (hole) transport is realized when the mean-free path of charge excitations exceeds the channel length. This regime has been repeatedly investigated in a number of experiments on carbon nanotubes (Bachtold *et al.*, 2000; Berger *et al.*, 2002, 2003; Javey *et al.*, 2003; Mann *et al.*, 2003; Newson *et al.*, 2008; Pop, 2008). From an electronic band-structure viewpoint and using the precept of Landauer theory, each electronic band (i.e., *Bloch* state) contributes exactly one quantum of conductance ($G_0 = e^2/h$) to the transport. In a metallic single-wall carbon nanotube, this indicates that the intrinsic conductance is $4e^2/h \sim 6.5\ \mathrm{k\Omega}^{-1}$ (i.e., there are four channels, two for spins, and two are due to twofold degeneracy). Of course, in order to measure ballistic transport, the contact resistance between the nanotube and the leads has to be minimized. This can be achieved using Pd electrodes, and such a setup has indeed shown quantized conductance plateaus, even if the observed conductance plateaus were

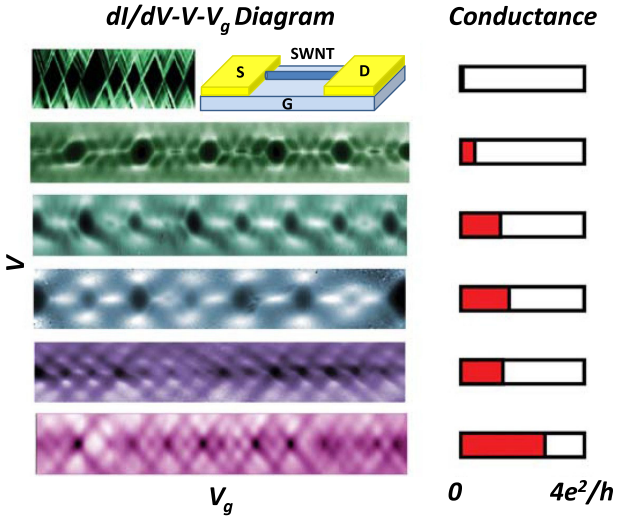

FIG. 34. Differential conductance dI/dV as a function of gate (G) voltage and source-drain (S-D) bias. Various quantum transport regimes of a single nanotube connected to metallic leads are illustrated depending on the coupling strength between the leads and the nanotube conduction channel. The coupling continuously changes from highly reflective (top) to highly transmissive (bottom). The diamond shapes shown on top are typical manifestations of the Coulomb blockade effect where the addition of one charge to the nanotube corresponds to each diamond. The bottom panel corresponds to a Fabry-Pérot–type interference pattern of a one-dimensional standing wave. The amount of conductance in each case is shown on the right. From Liang, Bockrath, and Park, 2005.

separated by e^2/h, instead of the expected $2e^2/h$ as a function of gate voltage. Such observations were made even at zero applied magnetic field (Biercuk *et al.*, 2005), suggesting that both orbital and spin degeneracy are lifted during the gate-depletion process (Ferry, Goodnick, and Bird, 2009). Further, in ballistic nanotubes, interference between the one-dimensional standing waves yields conductance oscillations similar to Fabry-Pérot oscillations in an optical cavity, as shown in the bottom diagram of Fig. 34 (Liang *et al.*, 2001).

Another fascinating quantum phenomena is the Luttinger liquid state, which is a low-dimensional state characterized by strong particle-particle interactions. Metallic states of electrons in two and three dimensions behave like a Fermi liquid in which the excitations carry a charge e, a spin $1/2$, and behave like weakly interacting fermions. In one dimension, where electron-electron interactions are particularly strong, the sea of carriers no longer behaves as a Fermi liquid. Instead, spin and charge excitations obey the physics of bosonic modes and propagate at different velocities (Haldane, 1981). This state, referred to as a Luttinger liquid, has been frequently observed in carbon nanotubes, since CNTs can show nearly an ideal realization of interacting charges in one dimension. One of the main signatures of the presence of the Luttinger liquid state is the observation of a power-law scaling of the conductance with temperature and source-drain bias (Bockrath *et al.*, 1999; Postma *et al.*, 2001; Ilani *et al.*, 2006).

Lastly quantum dots are characterized by a quantum regime where single electron charging governs electron transport. This can happen when the contact resistance of a device is well in excess of a single-channel quantum resistance to effectively trap the electron on the dot. For a nanotube island of capacitance C, the energy required to add a charge (charging energy) $e^2/2C$ must be larger than the thermal energy k_BT. These two conditions are met for nanotubes at cryogenic temperature ($T < 4$ K), since nanotube capacitances are in the range of attofarads and the separation between discrete electronic states in the zero-dimensional islands are in the meV range. In such a case, transport follows a Coulomb blockade behavior and measurements allow for the direct mapping of the discrete charge states, including the excited-state energy spectrum (Kouwenhoven and Marcus, 1998).

5. Functional nanotube device development

A number of devices based on carbon nanotubes have already been demonstrated in the laboratory, and some were shown to compete with and even outperform similar silicon-based devices. For example, Derycke *et al.* (2001) managed to selectively dope part of a single carbon nanotube placed over three metal contacts and demonstrated the possibility of creating an intramolecular complementary carbon nanotube field-effect transistor (CNFET) gate. Using a similar type of CNFET, Bachtold *et al.* (2001) demonstrated inverter device performance. Nanotube devices were built using a feedback-gate FET structure designed with the new feature where an additional feedback gate is connected directly to the drain electrode of the FET, allowing for a low 10^{-13} A off-state current, a high 10^8 current on-off ratio, and negligible leakage current. These results show the potential to meet industry standards for low-static-power logic electronics applications, and for applications with low leakage current (Qiu *et al.*, 2015). Fundamental research on ultrasmall integrated photonic devices demonstrated polarized infrared optical emission from a CNT ambipolar FET where it was hypothesized that optical emission originates from radiative recombination of electrons and holes that are simultaneously injected into an undoped nanotube, showing that thin Schottky barriers form at the source and drain contacts (Misewich *et al.*, 2003). Much work is devoted to the use of carbon nanotubes for high-performance digital logic technology beyond the traditional silicon complementary metal oxide semiconductor (CMOS) scaling but a number of problems remain to be solved, including the need for nanotubes with high purity, their proper placement on chips, and their contact with external electrodes. These technological challenges have been considered in a review article which outlined the recent progress made to tackle these difficulties (Tulevski *et al.*, 2014).

It is now possible to add a number of additional elements to CNT-FET building blocks to realize basic nanocircuits or to obtain simple static random access memory components. For example, memory concepts can be developed by exploiting other carbon nanotube architectures, such as in a crossbar arrangement (Rueckes *et al.*, 2000). Other devices, based on the functioning principle of electrically erasable programmable read only memory, were fabricated by combining semiconducting and metallic carbon nanotubes, for example, with the realization of NAND gates (Fuhrer *et al.*, 2002). Modification to the conducting state of a carbon nanotube by manipulating the relative position of an embedded polar molecule was also proposed as a basis for a nonvolatile memory device (Meunier, Kalinin, and Sumpter, 2007).

A number of applications based on nanotube devices have been developed over the years, including but by no means limited to devices using inkjet-printed carbon nanotube electrodes (Azoubel, Shemesh, and Magdassi, 2012), thermally reliable high-field network devices made up of sorted carbon nanotubes (Behnam *et al.*, 2013), improved device-to-device consistency using methods to understand and reduce variability in carbon nanotube transistors (Franklin, Tulevski *et al.*, 2012), and development of devices with optically imaged and spectroscopically characterized nanotube channels using high-throughput techniques (K. Liu *et al.*, 2013). Integrated circuits with field-effect transistors were built on individual CNTs with different electrical properties, including a multifunctional function generator (Pei *et al.*, 2014). Techniques were devised to couple carbon nanotube devices to microwave circuits, to enable significant increase in bandwidth and signal-to-noise ratio as a means to improve correlation measurements on high impedance devices such as quantum dots (Gramich, Baumgartner, and Schonenberger, 2015) and quantum dot circuits (Ranjan *et al.*, 2015). In a different study, random network single-walled CNTs field-effect transistors were assembled in a bottom contact and top gate geometry with only five different semiconducting nanotube species that were selected by dispersion with poly(9,9-dioctylfluorene) in toluene (Jakubka *et al.*, 2013). Wang *et al.* (2014) reported a method to controllably n-dope single-walled CNTs where the threshold voltage of the resulting transitions can be continuously modified, as a key step toward development of inverters and logic gates. Major recent advances keep being reported toward the

commercial viability of carbon nanotube based electronics. For example, Hersam's group at Northwestern recently demonstrated the stable and uniform electronic performance of complementary *p*-type and *n*-type single-walled CNTs thin-film transistors where the presence of adsorbed atmospheric dopants is controlled by incorporating encapsulation layers. This group then used these films to demonstrate low-power static random access memory circuits (Geier *et al.*, 2015).

6. CNT networks and thin films

The ability to form integrated circuits on flexible sheets of plastic enables attributes in electronic devices that are very difficult to accomplish with conventional technologies. In contrast to emerging technologies based on organic small-molecule and polymer-based materials, carbon nanotube networks show a much more promising performance. For instance, Cao *et al.* (2008) demonstrated implementations of high-performance random networks of single-walled carbon nanotubes for small- to medium-scale integrated digital circuits, made up of tens of highly functional transistors on plastic substrates. Recent advances show CNT network transistors fabricated using the Langmuir-Schaefer approach to exhibit excellent device performance (Cao *et al.*, 2013). One possible macroscopic use of CNTs in actual applications is as part of continuous fibers that retain the properties of individual CNTs. These fibers are also referred to as *yarns* or *threads*, and have been obtained experimentally by a number of research groups (Zhang, Atkinson, and Baughman, 2004; Koziol *et al.*, 2007; Behabtu *et al.*, 2013). One potential use of these pure CNT fibers includes electrical wiring with the advantage of being very light, yet mechanically strong and very efficient for high-frequency signal transfer.

A number of challenges remain to be solved before the technology can be used in real user electronics but recent years have seen much progress as recently discussed in the literature (Lekawa-Raus *et al.*, 2014). For instance, as-grown nanotube networks usually contain both metallic and semiconducting nanotubes, which lead to a trade-off between charge-carrier mobility and on-off ratio: the former increases with the number of metallic nanotubes while the latter increases with the number of semiconducting systems. To address this issue, Sun *et al.* (2011) developed a scalable filtration method to separate metallic nanotubes from semiconducting nanotubes that leads to the fabrication of high-performance thin-film transistors and integrated circuits on flexible and transparent substrates. The nanotube network consists of micrometer long nanotubes connected by low-resistance Y-shaped junctions with excellent mobility and on-off ratio. Recent research on CNT networks indicates that their properties are also sensitive to the CNT length, and that the network can display a negative temperature coefficient of resistance. In contrast, the tunneling activation energy is found to be independent of both CNT length and orientation, thereby establishing the fact that changes in electron transport are due to the number of tunneling (i.e., the morphology of the network) CNT-CNT junctions that create a percolation path between external electrodes (Lee *et al.*, 2015).

Haddon's group recently reviewed the state of the art in using semiconducting CNT thin film as a platform for electronic and photonic devices. CNT thin films can be assembled in such a way as to display the combined advantages of individual CNTs and the possibility of large-area devices. Many properties of flexible CNT thin films have been developed in the laboratory [e.g., FETs, sensors, detectors, photovoltaic cells, and light-emitting diodes (LEDs)] while other more challenging and advanced applications are currently under aggressive development (Itkis *et al.*, 2015).

C. Graphene nanoribbons

Graphene is regarded as a promising candidate for extending some aspects of Moore's law of silicon technology as silicon approaches its miniaturization limit (Schwierz, 2010). One of the reasons for such an interest in graphene is its high electronic mobility and low contact resistance (Palma and Samori, 2011; Xia *et al.*, 2011). However, an ideal infinite graphene sheet is not a semiconducting system, and the absence of an energy gap in graphene is a fundamental impediment for applications in nanoelectronics. To remedy this limitation, researchers have discussed the possibility to modify graphene's electronic structure to induce a separation of the energy bands around the Fermi energy. One possible route was discussed earlier with the use of carbon nanotubes. However, transforming a structure from graphene into a carbon nanotube is an operation that is better suited for computational modeling than for actual sample preparation. Alternatively, conferring spatial confinement to the electronic degrees of freedom can be achieved by reducing the dimensionality from 2D graphene sheets into 1D graphene nanoribbons (Nakada *et al.*, 1996). GNRs exhibit electronic properties strongly dependent on their width and edge structure, as discussed in Figs. 3 and 6. Figure 35 provides an example of an experimental realization of a series of nanoribbons with varying widths.

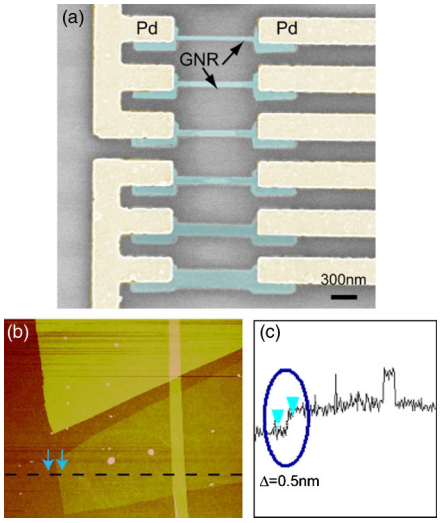

FIG. 35. (a) SEM micrograph of GNR devices with various channel widths fabricated on a 200 nm thick SiO_2 substrate. The widths of the GNRs from top to bottom are 20, 30, 40, 50, 100, and 200 nm. Each GNR was prepared by a lithographic process. (b) AFM image of a single-layer graphene sample before lithographic thinning. (c) Cross-section measurement of the AFM image along the dashed line shown in (b) indicating that the sheet is a single layer of graphene. From Chen *et al.*, 2007.

1. Intrinsic electronic transport properties

Theory predicts that AGNRs show a semiconducting character with a band gap Δ_n that is strongly dependent on the number n of C–C bonds along its width (Fig. 6). While the gap of an n-AGNR is closed as $n \to \infty$, the Δ_n vs n curve has three different branches, such that $\Delta_{3i+1} \geq \Delta_{3i} \geq \Delta_{3i+2}$ (Son, Cohen, and Louie, 2006a). Compared to AGNRs, ZGNRs show a richer set of physical properties. While spin polarization in infinite AGNRs is absent, theory predicts that ZGNRs possess ferromagnetically polarized edges with two possibilities for edge-to-edge polarization. These two possibilities correspond to parallel (ferromagnetic-FeM) and antiparallel (antiferromagnetic-AFeM) alignments, the latter being the overall ground state.

The PM state has two twofold degenerate bands around the Fermi energy which meet and become a flat fourfold degenerate band that extends along one-third of the BZ and whose energy value approaches $E_F = 0$ as the ribbon width increases (Yazyev, 2010). These states are strongly localized along the edges (thereby accounting for the fourfold degeneracy: two due to the spin and an additional two due to the two symmetric edges), producing a high concentration of low energy electrons (Pisani *et al.*, 2007).

Such edge states are predicted to be responsible for the paramagnetic behavior of ZGNRs at low temperatures (Wakabayashi *et al.*, 1999), while a diamagnetic behavior is expected at high temperature. This high density of states indeed produces an instability (paramagnetic instability) which gives rise to the two lower energy magnetic states, as shown in Fig. 36. One observes that the spin-up and spin-down polarizations along the opposite edges of the ribbon are located on different graphene sublattices for the AFeM case which turns out to be the ground state under these conditions (Pisani *et al.*, 2007).

In the FeM case, edge atoms belonging to both sublattices exhibit the same spin orientation and this ends up raising the FeM energy slightly compared with that of the AFeM. While the AFeM case is lower in energy, a remarkably interesting fact about these AFeM and FeM states is the small energy difference between them. The band-energy difference between the AFeM and FeM states

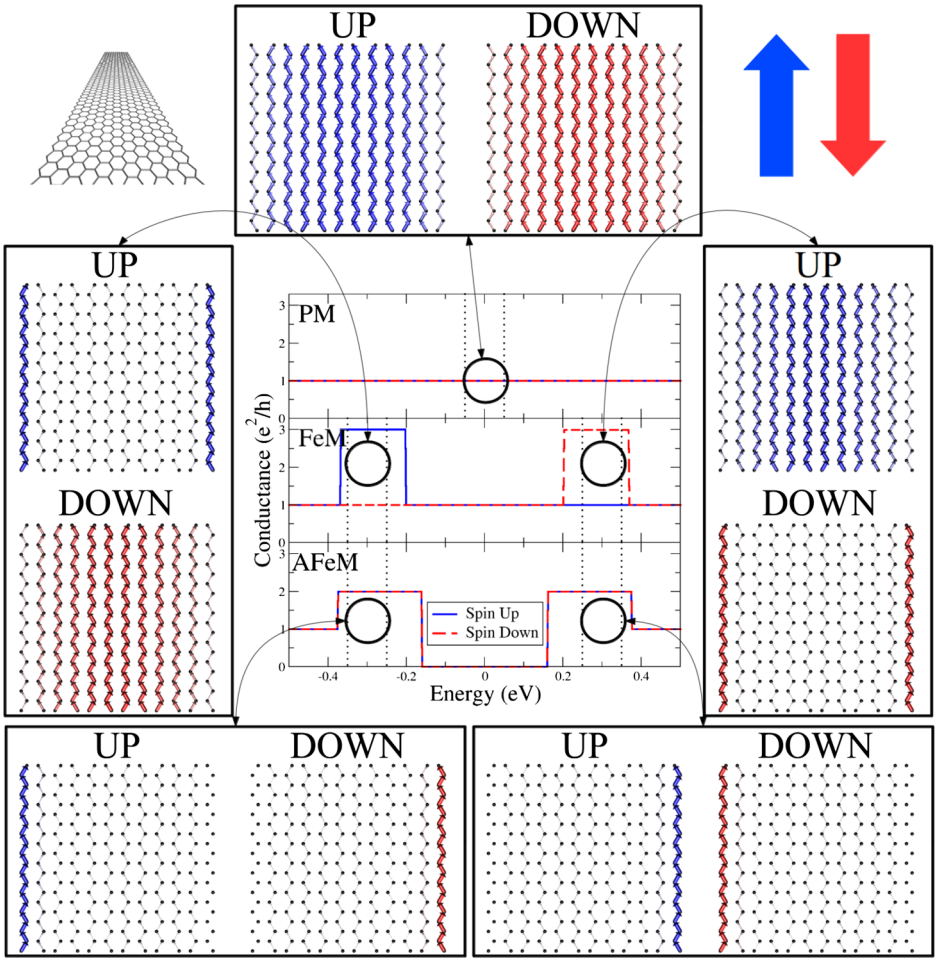

FIG. 36. Quantum conductance as a function of energy (center) for the PM, FeM, and AFeM states in a 12-ZGNR (solid blue curves correspond to spin-up and dashed red lines to spin-down states). For each state we present local current plots corresponding to $\mu_1 = -0.35$ eV and $\mu_2 = -0.25$ eV and to $\mu_1 = +0.25$ eV and $\mu_2 = +0.35$ eV for both the AFeM and FeM states and $\mu_{1/2} = \pm - 0.05$ eV for the PM case (chemical potential windows are marked by vertical black dotted lines), for both spin-up (blue) and spin-down (red) states. Adapted from Girão *et al.*, 2013.

for one ZGNR unit cell as a function of n vanishes as the ribbon width increases, indicating a lowering in the edge-to-edge interaction energy as the two edges become farther apart. A possible switching property based on this low energy difference is an interesting possibility that motivates the concept of producing a ZGNR based magnetic sensor (Munoz-Rojas, Fernandez-Rossier, and Palacios, 2009).

The direct measurement of edge states in zigzag nanoribbons remains a difficult task since clean ribbons with sharp zigzag edges are hard to create (Jia *et al.*, 2011). However, recent spectroscopic evidence obtained by the Tapasztó group indirectly confirms the presence of magnetic states in zigzag-type GNRs, in GNRs obtained using an STM tip to dig straight trenches within a graphene layer (Tapaszto *et al.*, 2008; Magda *et al.*, 2014). Li *et al.* (2014) also reported results on gap openings in zigzag GNRs created from Fe nanoparticle-assisted hydrogen etching of graphene.

The existence of rich magnetic properties opens up a number of exciting possibilities for the use of finite strips of graphene in nanoelectronics and spintronics. For instance, it has been shown that ZGNRs present a half-metallic behavior (where the electronic structure has a metallic character for spin-up levels and is semiconducting for spin-down levels, or vice versa) which can be tuned using a gate voltage (Son, Cohen, and Louie, 2006a).

The importance of the details of the conductance and valence states in ZGNRs in their various spin distributions is embodied by Fig. 36, which presents an overview of the calculated spin-polarized conductance at various chemical potentials for the PM, FeM, and AFeM states. Here the various structures shown in Fig. 36 are connected to perfect electrodes made of the same materials and it follows that the plots of the transport channels are equivalent to the spatial distributions of Bloch states. For example, in the ground state (which adopts an AFeM spin configuration), a remarkable 1D localization of the spin states along the edge can be seen with spin-up and spin-down channels localized at opposite sides of the structure. We note that experimental evidence indicates that actual edges are usually made up of a mixture of armchair and zigzag edges, thereby forming what is usually referred to as *chiral* edges; see, e.g., Tao *et al.* (2011) and Pan *et al.* (2012). Chen *et al.* (2007) showed experimentally that a narrow (∼20 nm) GNR could be fabricated by e-beam lithography and etching techniques and could be incorporated as channels of FETs, showing that transport properties in this case are governed by boundary scattering and trapped charges in the substrate. The analysis of the I-V curves indicates that a confinement-induced gap on the order of 30 meV was found for the narrowest 20 nm ribbon. Furthermore, epitaxially grown GNRs on silicon carbide were recently shown to behave like single-channel room-temperature ballistic conductors over more than a 10 μm distance. This observation is of fundamental importance, not only because this performance is similar to that reported for metallic carbon nanotubes, but also because this material can be produced in large quantity, thereby opening a route to possible scalable manufacture, assembly, and commercial applications based on GNRs (Baringhaus *et al.*, 2014).

2. Toward defect-free GNRs

Electronic transport properties of 1D systems are known to be extremely sensitive to disorder, as stated notably by the theory of localization (Lee and Ramakrishnan, 1985). Care must therefore be taken since there would be no gain in opening a band gap in graphene-based materials if the mobilities were dramatically reduced at the same time. Therefore, the narrowing of graphene into 1D ribbons requires experimentalists to carefully maintain a high structural quality during synthesis. In this context, a notable breakthrough has been achieved with the development of bottom-up chemistry approaches, where perfectly edged graphene nanoribbons can now be obtained from the assembly of small monomers as mentioned in Sec. IV.B (Cai *et al.*, 2010; Blankenburg *et al.*, 2012; Huang *et al.*, 2012; Linden *et al.*, 2012), including ultranarrow armchair systems (Kimouche *et al.*, 2015). The monomers are gradually assembled by chemical reaction and thermal treatment to first form polymers on a metallic surface by Ullmann coupling followed by cyclo-dehydrogenation to yield the coveted atomically sharp graphene ribbons (Cai *et al.*, 2010; Björk, Stafström, and Hanke, 2011). One notable drawback of this approach is the difficulty to assemble nanodevices since the structures are firmly bonded to a metallic substrate following fabrication. In spite of this difficulty, Koch *et al.* (2012) utilized this synthesis technique to prepare a GNR structure which was subsequently lifted off the surface (with minimal damage) using an STM tip for transport measurements, as shown in Fig. 37.

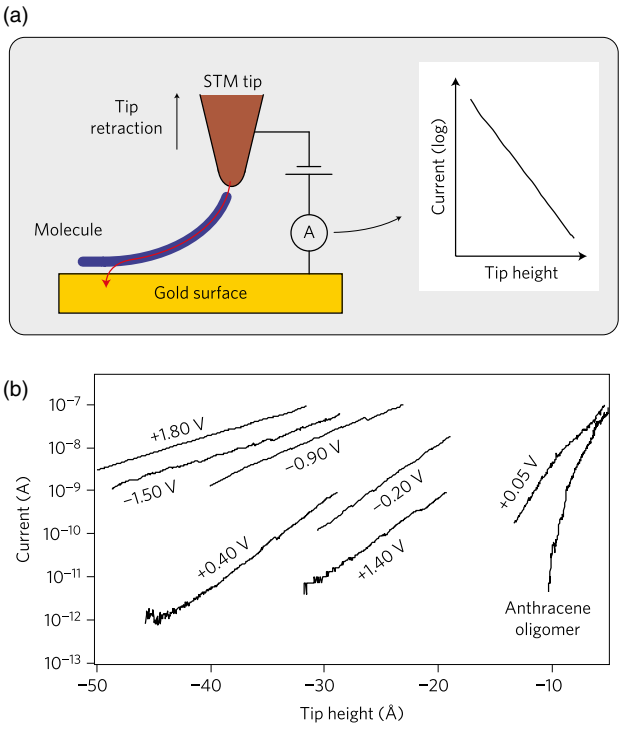

FIG. 37. Conductance measurements of a defect-free GNR obtained by the Ullmann coupling followed by the cyclo-dehydrogenation method (Cai *et al.*, 2010). In this experiment, an STM tip pulls on the molecule to detach it from the gold substrate (a) and the current is recorded for various values of tip-substrate bias [inset to (a)] and tip height (b). Adapted from Koch *et al.*, 2012.

Further, Bennett *et al.* (2013) developed field-effect transistors using nanoribbons assembled using this technique and created prototypical devices thanks to the development of a layer transfer process. Note that a substrate is not necessary to synthesize large quantities of nanoribbons using this technique, as demonstrated by the Sinitskii group for both pristine and nitrogen-doped GNRs grown in solution. However, the assembly of devices with this technique presents many of the usual challenges faced by solution-based approaches to nanoelectronics (Vo *et al.*, 2014a, 2014b).

This growth method has shown promising versatility since monomers of various shapes, sizes, and compositions can be employed to produce different types of ribbons (Cai *et al.*, 2010; Han *et al.*, 2014; Sakaguchi *et al.*, 2014). These include graphene nanowiggles (see Fig. 21), which are ribbons with chevronlike edges with attractive transport properties, as discussed previously in Sec. IV with Figs. 21 and 22 (Costa Girão *et al.*, 2011). The possibility of assembling larger molecules into wider nanoribbons has also been demonstrated, allowing for a fine-tuning of the band gap with the change of the nanoribbon width (Huang *et al.*, 2012; Linden *et al.*, 2012; Sakaguchi *et al.*, 2014). Recent work performed in Crommie's group used a similar growth technique with a variety of monomers to enable band gap engineering based on all-carbon heterojunctions (Chen *et al.*, 2015).

In addition to pure hydrocarbon monomers, monomers where a number of carbon atoms are substituted by chemical elements, such as B or N, can also be employed to create atomically precise doped nanoribbons. For instance, nitrogen substitution in the tetraphenyl-triphenylene monomers leads to the fabrication of N-doped graphene nanowiggles (Bronner *et al.*, 2013; Cai *et al.*, 2014; Vo *et al.*, 2014b). Such a doping scheme offers opportunities toward a precise control of dopant positions and concentrations in 1D sp^2 carbon materials. A perfect knowledge of the nitrogen dopant positions in the graphene sublattice is expected to yield a number of well-defined features in the electronic spectrum of such materials (Yu *et al.*, 2010; Lherbier, Botello-Méndez, and Charlier, 2013; Owens, Cruz-Silva, and Meunier, 2013; Rani and Jindal, 2013; Cai *et al.*, 2014; Liang and Meunier, 2015). Moreover, more recent work showed that pristine and substituted monomers can be used concurrently to produce one of the first atomically sharp carbon-based type-II (i.e., staggered gap) heterojunctions, as shown in Fig. 38 (Cai *et al.*, 2014).

3. Tailoring GNR's electronic properties

As mentioned a number of times in this review, GNRs can be either semiconducting or metallic, depending on their edge geometry and magnetic order (Son, Cohen, and Louie, 2006b; Pisani *et al.*, 2007). However, the energy band gap is strongly dependent on the nanoribbon width (Son, Cohen, and Louie, 2006a). For experimentally feasible nanoribbon widths, semiconducting GNRs have energy band gaps on the order of a few hundredths to a few tenths of eV, which are comparable to thermal energies. This is impractical for integrated nanoelectronic applications. Several methods have been explored to increase the energy gap and to modulate the electronic properties of GNRs, ranging from defect-based to chemical-based methods, as discussed next.

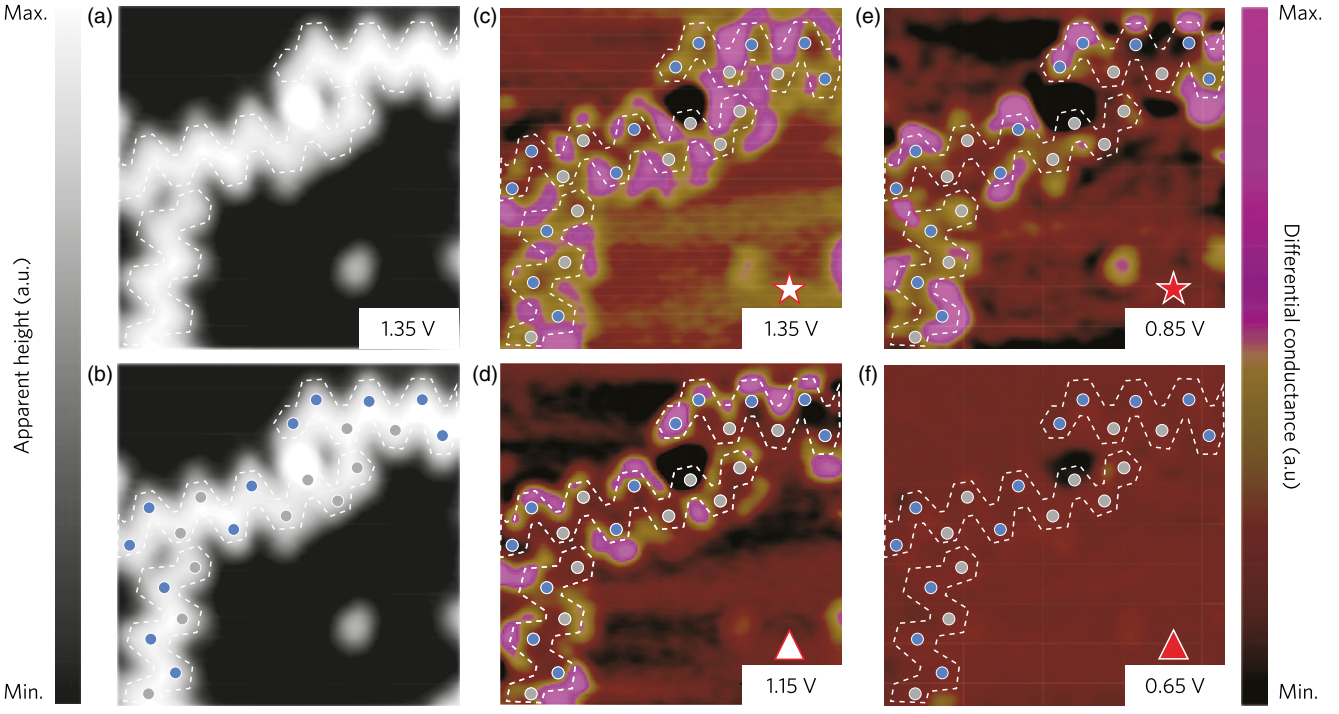

FIG. 38. Differential conductance maps of an intramolecular junction between a pristine (p) and nitrogen-doped GNR heterostructures. Heterostructures are artificially outlined by white dashed lines for clarity for the reader. The 10×10 nm^2 STM images recorded at $T = 5$ K, $U = 1.35$ V, and $I = 0.15$ nA are shown in (a) and (b). In (b), the p- and N-GNR units are indicated by gray and blue dots, respectively. (c)–(f) Selected examples of conductance maps at energy positions around the conductance band minimum. The analysis of the results shows that the heterojunction features a type-II alignment with a sharp transition region. From Cai *et al.*, 2014.

a. Nonhexagonal ring defects

While hexagons are the most stable rings in graphenelike structures, the carbon lattice can also sustain the presence of nonhexagonal rings, so long as the topology of the structure seen as a direct graph is maintained (Bullard *et al.*, 2014). These topological defects can be created during growth or after growth, and, for instance, created by electron irradiation (Krasheninnikov and Banhart, 2007). Terrones and Mackay (1992) proposed that pentagon and heptagon (5-7) pairs could be introduced in planar graphitic structures without modifying the long-range planarity of the structure, as opposed to the curvature changes introduced by only pentagons or heptagons. 5-7 pairs and other higher order rings, such as 5-8-5 groups, could be found at grain boundaries between graphitic domains with different orientations, and similar structures were later observed experimentally by Simonis *et al.* (2002). In this respect, Huang *et al.* (2011) developed an atomic resolution imaging technique based on diffraction-filtered imaging to determine the location and nature of all atoms in a grain boundary in graphene, and they concluded that the grains stitch together predominantly by pentagon-heptagon pairs. Koskinen, Malola, and Häkkinen (2008) proposed that unpassivated zigzag edges in graphene nanoribbons could undergo a bond rotation that would change the hexagons at the zigzag edge into a sequence of pentagons and heptagons, transforming the zigzag edge into an armchair edge. Later, the same group reported the experimental observation of such edges (Koskinen, Malola, and Häkkinen, 2009) from the analysis of a high-resolution transmission electron microscope (Girit *et al.*, 2009). Dubois *et al.* (2010) investigated the effects of pentagon and heptagon rings at the edges of armchair graphene nanoribbons, showing that defects break the aromaticity of the edge atoms and severely affect the conductance of the system.

Defects play an important role in the science of sp^2 carbon materials and offer an additional degree of freedom to tune their properties. Extended lines of defects and grain boundaries are natural defects that can be found in some synthesized graphene samples and they can assume a highly crystalline organization. Both extended line defects (Botello-Mendez, Declerck *et al.*, 2011) and grain boundaries (Yazyev and Louie, 2010) in graphene are predicted theoretically to have interesting electronic and transport properties stemming from the interface between systems of varying structures and properties. These structures do not pose an unsurmountable issue for producing highly crystalline structures, but instead open a set of new possibilities to modify and tune the properties of graphene and their GNRs to promote specific new applications (Simonis *et al.*, 2002; Lahiri *et al.*, 2010; Yazyev and Louie, 2010; Ajayan and Yakobson, 2011; Botello-Mendez, Declerck *et al.*, 2011; Lin and Ni, 2011). Botello-Mendez *et al.* (2009) theoretically studied a chain of 5-7 pairs in order to create a seamless interface between an armchair and a zigzag GNR, creating hybrid GNRs that display new properties emerging from the presence of both zigzag and armchair edges. When stitched along the periodic direction, these hybrid GNRs display a half-metallic behavior (Fig. 39), since the zigzag edge presents a spin-polarized edge state, while the armchair edge is nonmagnetic, resulting in a spin-polarized conductor. On the other hand, if stitched perpendicular to the periodic direction, these hybrid graphene nanoribbons feature both zigzag and armchair domains, and the electronic transport across these junctions is driven by tunneling phenomena (see Fig. 39).

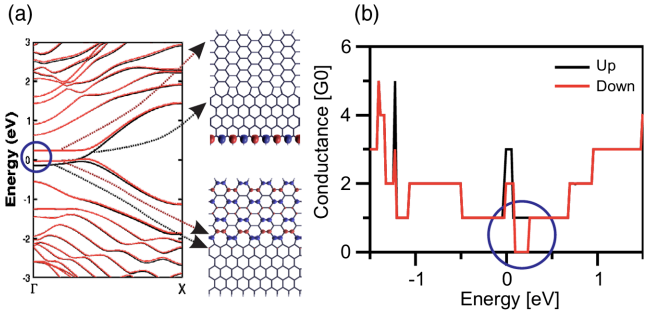

FIG. 39. (a) Band structure of a hybrid graphene nanoribbon with both zigzag and armchair edges. The arrows point to the wave-function plot of the states around the Fermi energy, displaying the edge state associated with the zigzag edge. The lower arrow points to the junction. (b) Electronic transport plot of conductance vs energy, revealing that the nanoribbon can be used as a spin filter on an energy window just above the Fermi energy. Adapted from Botello-Mendez *et al.*, 2009.

b. Edge and bulk disorder

In order to provide estimates of the stability of GNR-based electronic devices, an accurate account must be taken of the defects and their effects on transport properties, since these are inherent to most large-scale GNR production systems. Several groups have studied the effects of edge and bulk disorder on the transport properties of GNRs from a theoretical perspective (Areshkin, Gunlycke, and White, 2007; Evaldsson *et al.*, 2008; Lherbier *et al.*, 2008; Li and Lu, 2008; Cresti and Roche, 2009; Mucciolo, Neto, and Lewenkopf, 2009). Specifically, Areshkin, Gunlycke, and White (2007) used a recursive model to remove edge atoms to create vacancies at the edges that span several layers of atoms. It was also shown that zigzag-edged GNRs are more resistant to edge degradation than their armchair counterparts. While the zigzag edge is able to withstand large (50%) edge defect concentrations up to four edge layers deep, in the armchair case, only a 10% erosion of the outer edge layer is predicted to suppress electronic transport. Furthermore, a number of studies used a GNR model with a random edge disorder related to widths similar to experimentally available devices (Evaldsson *et al.*, 2008; Mucciolo, Neto, and Lewenkopf, 2009). They found that even moderate edge roughness is enough to cause localized scattering centers leading to Anderson localization and creating an electron transport gap, in accordance with the experimental results (Han *et al.*, 2007). Finally, we note that atomic vacancies have also been proposed to modify local transport properties (Amorim *et al.*, 2007), resulting in an enhancement of the system's reactivity and opening a set of new possibilities predicted for the physics and chemistry of these structures.

c. Substitutional doping

Substitutional doping by noncarbon atoms has been widely studied as a method for tailoring the electronic properties of other carbon-based materials, such as fullerenes and carbon nanotubes. The rationale behind this interest is that ions of atoms with a similar size to carbon (boron and nitrogen, in particular) could be easily inserted into the graphitic hexagonal lattice. In addition, it was earlier found theoretically that boron and nitrogen could, respectively, introduce acceptor or donor states in carbon nanotubes (Choi *et al.*, 2000). Substitutional doping of graphene has been experimentally achieved by different methods, such as electrothermal reactions (Wang *et al.*, 2009), hydrocarbon pyrolysis in the presence of ammonia (Qu *et al.*, 2010), and arc discharge (Subrahmanyam *et al.*, 2009), among others.

A number of theoretical studies of the effect of substitutional doping on the electronic transport of graphene nanoribbons have been carried out by several groups (Martins *et al.*, 2007, 2008; Biel *et al.*, 2009; Zheng *et al.*, 2009; Cruz-Silva, Barnett *et al.*, 2011). One of the earliest studies of such effects was carried out by Martins *et al.* (2007, 2008) who focused on doped narrow GNRs, finding that the introduction of doping atoms that interact with the carbon π states creates a spin anisotropy in the electronic transport around the energy corresponding to the localized state near the dopant. It was proposed that substitutional doping could be used to create graphene-based spin-polarized conductors. Other theoretical works also focused on the effects of boron and nitrogen doping on wider graphene nanoribbons (Biel *et al.*, 2009; Zheng *et al.*, 2009), while Cruz-Silva also examined the effects of substitutional doping with phosphorus on GNRs (Cruz-Silva, Barnett *et al.*, 2011). A surprising effect of doping found in these cases is that, for zigzag GNRs, nitrogen and boron could induce both donor and acceptor states depending on their position within the nanoribbon. As observed in Fig. 40, the energies of the localized states created by the doping atoms change as the position of the doping atoms in the nanoribbon gets closer to the edges, until finally crossing over the Fermi energy and moving to the other side of the energy spectrum. This effect can be explained by the increased exchange interaction due to the localization of the dopant-induced states and the high density of states at the zigzag edge (Cruz-Silva, Barnett *et al.*, 2011).

d. Chemical functionalization

A different pathway for modifying the electronic and transport properties of GNRs is through the use of chemical functionalization, with the idea of tuning the scattering process for functional device development. Modifications of the carbon π network, by doping or chemical interactions, result in changes of the electronic structure near the Fermi energy (Sumpter *et al.*, 2009). Such changes allow tailoring of the electronic transport properties at low voltages (Martins *et al.*, 2008). A variety of experimental techniques, both proposed and realized, have been developed to enable functionalization of graphene, such as hydrogenation (Elias *et al.*, 2009; Soriano *et al.*, 2010), oxidation (Gunlycke *et al.*, 2007; Cantele *et al.*, 2009; Lopez-Bezanilla, Triozon, and Roche, 2009), and chemical attachment of metallic atoms (Gorjizadeh *et al.*, 2008).

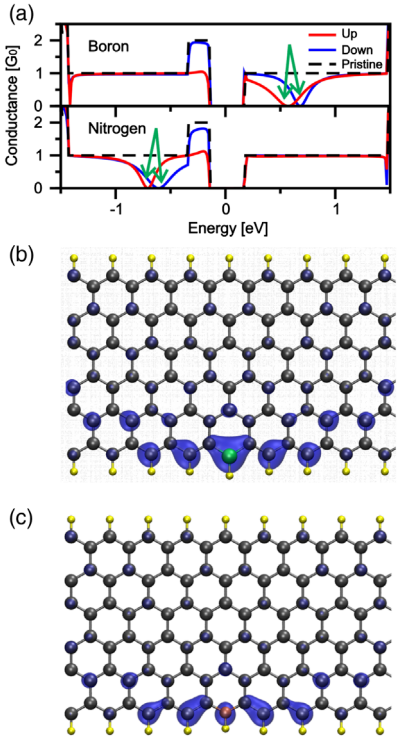

FIG. 40. (a) DFT calculated electronic transport of boron- and nitrogen-doped graphene nanoribbons. Green arrows indicate the energy of the calculated donorlike (boron) and the acceptorlike (nitrogen) states. Local density of states plots for (b) nitrogen and (c) boron localized states at the energies indicated by the arrows in (a). Adapted from Cruz-Silva, Barnett *et al.*, 2011.

Fully hydrogenated graphene (graphane) was proposed theoretically first (Sofo, Chaudhari, and Barber, 2007) and soon after experimentally (Elias *et al.*, 2009). On an sp^2 carbon atom, hydrogen can be bonded only to the free p_z orbital, forcing a change to an sp^3 hybridization on the host atom and forming a σ bond. Since full hydrogenation of graphene results in the rehybridization of all carbon atoms, graphane can be considered as a single diamond layer, and graphane has been found experimentally to be a wide gap semiconductor, like diamond (Elias *et al.*, 2009). Selective hydrogenation can be used to modify the electronic properties of graphene nanoribbons. An example of this is the computational study that investigated the tunneling magnetoresistance of a doubly hydrogenated armchair GNR as a function of the distance between hydrogenated sites (Soriano *et al.*, 2010). Soriano *et al.* (2010) also found that hydrogenation of sites close to the nanoribbon edges is more energetically stable than that occurring at the central atoms. They also found that the near-edge hydrogenation is more effective at creating a tunneling magnetoresistance and proposed that these kinds of hydrogenated nanoribbons have potential for use in spintronic applications (Soriano *et al.*, 2010).

Oxygen, as well as other functional groups that attach to sp^2-based carbon nanostructures, can modify the π-orbital network. It was shown, early on, that by attaching oxygen, hydroxyl (-OH), or imine (-NH) groups at the edges of a

zigzag GNR, it could be possible to indirectly close the energy gap in the antiferromagnetic ground state of zigzag GNRs (Gunlycke *et al.*, 2007). Using localized Wannier functions, Cantele *et al.* (2009) showed that the states induced by oxygen at the Fermi energy are due to lone pair states. Another approach to study the effects of oxidation is based on a decimation method to perform quantum transport calculations on real-length graphene nanoribbons up to 600 nm where it was found that the elastic mean-free path for these nanoribbons quickly decays with an increasing number of hydrogen and hydroxyl functional groups attached to the nanoribbon (Lopez-Bezanilla, Triozon, and Roche, 2009). Other attempts to modify the electronic structure of GNRs are based on substituting the edge carbon atom by third row transition metal atoms (Gorjizadeh *et al.*, 2008; Rigo *et al.*, 2009). Further, Solis-Fernandez *et al.* (2015) showed that graphene nanoribbons can be doped as either *n* or *p* type in a tunable fashion, using appropriately chosen functional molecules. The doping was found to be particularly affected by edges and the scheme has promising potential for the development of large-scale *p*-*n* junctions using conventional methods used for electronic circuits.

e. GNR assemblies

In addition to the properties of individual graphene nanowiggles mentioned previously, graphene and GNRs have been assembled into several new large-scale structures in theoretical calculations. Porous systems like graphene antidot lattices, for instance, have been shown to allow for a controlled manipulation of the electronic properties of graphene (Pedersen *et al.*, 2008; Sandner *et al.*, 2015) as well as of GNR properties (Hatanaka, 2010; Baskin and Kral, 2011). Other proposals exploit the interplay between armchair and zigzag edges in more complex ribbon geometries to demonstrate spin-filter devices and geometry-dependent controlling approaches for the localization of magnetic edge states (Wang *et al.*, 2007; Hancock *et al.*, 2008; Sevinçli, Topsakal, and Ciraci, 2008; Topsakal, Sevincli, and Ciraci, 2008; Ma and Sheng, 2011; Saffarzadeh and Farghadan, 2011).

Theoretical proposals of junctions composed of AGNRs and ZGNRs (Botello-Mendez, Cruz-Silva *et al.*, 2011) and 1D GNR superlattices (Sevinçli, Topsakal, and Ciraci, 2008; Topsakal, Sevincli, and Ciraci, 2008) have been made for new structures that might be suitable to be embedded in new electronic nanodevices. The stacking of multiple GNRs is predicted to have a major influence on both the electronic structure and magnetic states of these multilayer systems due to the interplay between intralayer and interlayer coupling (Kharche *et al.*, 2011). Furthermore, the behavior of the electronic current as a function of temperature and device length is now well understood in terms of *ab initio* calculations (Saha *et al.*, 2010, 2011; Padilha *et al.*, 2011). We note also that calculations show that the stacking of two GNRs bonded by van der Waals forces can be used as a rheostat with the cross-GNR conductance being finely tuned by the relative angle between the two GNRs (Botello-Mendez, Cruz-Silva *et al.*, 2011). In this case, a multiterminal transport formalism must be employed to evaluate the electronic transmission between any two sides of one layer and the corresponding sides of the second layer. For instance, Qi *et al.* (2015) performed transport measurements under a TEM to show experimentally that few-layer GNRs frequently formed bonded bilayers that are remarkably robust. They showed that a sub-10-nm bonded bilayer GNR was about 5 times more conductive than a similar size GNR monolayer thanks in part to the reduced scattering at the annealed edges. Other possible arrangements of nanoribbons into functional devices have been proposed theoretically, such as the all-graphene planar self-switching metal-insulator-semiconductor field-effect diode, where a single device is composed of seamlessly attached nanoribbons of differing widths and, therefore, different electronic properties (Al-Dirini *et al.*, 2014).

VI. QUASI-1D *sp*-sp^2 AND 3D NANOSTRUCTURES WITH MIXED HYBRIDIZATIONS

A. Toward 1D carbon chains

Carbyne is the one-dimensional allotrope of carbon composed of *sp*-hybridized atoms. A search for 1D carbon nanosystems at the one-atom cross-section limit has been performed in recent years. Chainlike systems are particularly interesting since they are predicted to be the stiffest material under tension and an applied strain can be used to modulate their conducting behavior (M. Liu *et al.*, 2013; Artyukhov, Liu, and Yakobson, 2014). Linear carbon chains can feature either cumulene $\cdots C=C=C=C=C\cdots$ or polyyne $\cdots C-C\equiv C-C\equiv C\cdots$ bonding. It is known that the polyyne configuration is less stable than that of cumulene, because the latter has a degenerate pair of half-filled energy bands which can be stabilized into the former as the result of a Peierls distortion (Kastner *et al.*, 1995; Yang and Kertesz, 2008). In fact, it was experimentally confirmed that the polyyne structure is indeed unstable under ambient conditions (Cataldo, 2006), since it has unsaturated bonds that are indeed highly reactive (Kertesz and Yang, 2009).

The empty space available in the core of a carbon nanotube has been shown to provide an ideal environment for stabilizing linear carbon chains (X. Zhao *et al.*, 2003; Fantini *et al.*, 2006; Jinno *et al.*, 2006; Nishide *et al.*, 2006; Andrade, Vasconcelos *et al.*, 2015). In addition, graphene and nanoribbons have been used as a template for preparing chains under an electron beam in a transmission electron microscope and at the same time used as electrodes for contacting the chains (Cretu *et al.*, 2013; Casillas *et al.*, 2014). Graphene has also been used as a substrate for depositing linear carbon chains (Kano *et al.*, 2014).

The transport properties of small length carbon chains have been measured using graphene as electrodes and the transport has been modeled; see Fig. 41 (Cretu *et al.*, 2013). Figures 41(a)–41(e) show the electronic band structures and the conductance of linear carbon chains with both polyyne and cumulene bonding. As illustrated in Fig. 41(e), the presence of strain further opens a band gap and the conductance for strained carbon chains is expected to be low. This result is in agreement with existing experimental data shown in Fig. 41(f). Based on these electronic transmission images, the drop in current shown in Fig. 41(f) is found to be due to the formation of the chain. We note that

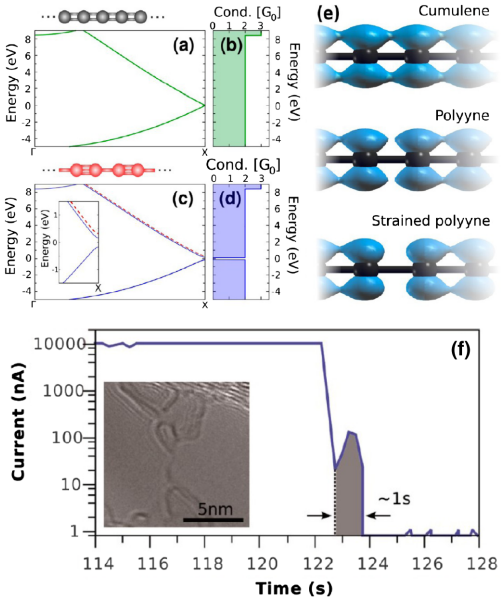

FIG. 41. (a), (c) Calculated electronic band structure and (b), (d) quantum conductance of cumulene and polyyne chains. (e) The electronic densities for cumulene, polyyne, and strained polyyne chains. (f) Time-dependent electrical current measurements made during the formation of a carbon chain. The inset to (f) shows the TEM images of the formed chains, just after the sudden drop is observed in the electrical current. From Cretu *et al.*, 2013.

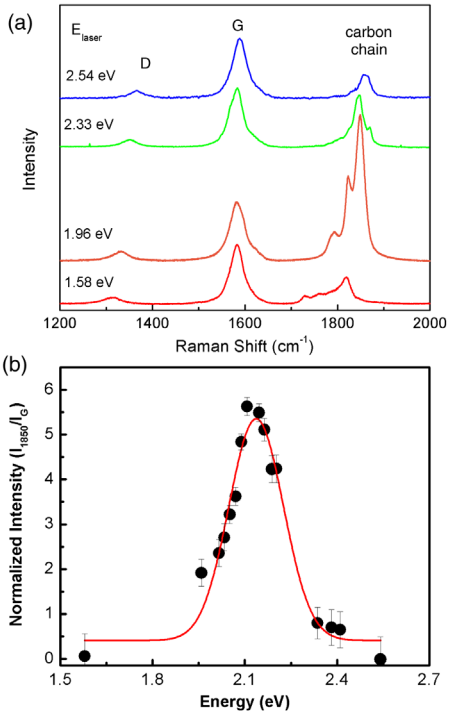

FIG. 42. (a) Resonance Raman spectra of linear carbon chains encapsulated in multiwall carbon nanotubes. The *D*- and *G*-band Raman modes from carbon nanotubes are shown here along with the bands from the chain. (b) Resonance window of the linear carbon chain mode. From Andrade, Vasconcelos *et al.*, 2015 and Andrade, Aguiar *et al.*, 2015.

the current measured for the chains is about 5 orders of magnitude lower than that for the nanoribbons. Recent work from the Banhart group experimentally demonstrated the strain-induced transition from metal to semiconductor in monatomic carbon chains, as observed using the electron microscope. They also highlighted an electrical rectifying behavior that was explained as stemming from processes taking place at the contact with the leads (La Torre *et al.*, 2015).

It is not easy to directly access chains stabilized inside carbon nanotubes. In that context, optical techniques have proven promising for characterizing the chains (Andrade, Aguiar *et al.*, 2015). The synthesis of long carbon chains inside a multiwalled carbon nanotube offers an attractive opportunity for measuring the phonon spectra of these 1D solids by using Raman spectroscopy. In Fig. 42(a), the resonance Raman spectra of a sample with a carbon chain inside a multiwalled carbon nanotube are shown for different laser lines. Besides the standard modes from the sp^2 lattice of the nanotubes, a very strong peak is observed near 1850 cm^{-1}, which is assigned to the carbon chain. The intensities and frequencies of the normal modes in the chain depend on the laser energy. This is due to the presence of chains of different lengths in the sample. The chain length has a strong influence on its electronic band gap and on the carbon-carbon bond distance, which in turn affects the phonon frequency. It was possible to measure the resonance window for the chains as shown in Fig. 42(b). By fitting those points with a Gaussian line profile, a 2.13 eV energy gap was measured, in good agreement with a *GW* many-body calculated value (2.16 eV) (Al-Backri, Zlyomi, and Lambert, 2014).

Moving from single 1D systems, recent work has reported the possibility of one-dimensional sp solid carbon. The existence of such a system is still under some debate and a recent report by Pan *et al.* (2015) fueled this debate with renewed discussions regarding the existence of carbyne. These authors prepared carbyne crystals in a polyynelike configuration, and with a hexagonal crystalline structure and an optical emission in the blue region. Further research is needed. These new crystal forms of sp carbon will certainly stimulate the community to exploit the optical and electronic properties of these materials, which could be tuned by choosing the length of the chains.

B. 3D nanostructured carbon systems

Generally transitions from sp^2 to sp^3 occur in any situations where sharp changes in curvature take place, as seen for instance in 3D nanotube networks (Romo-Herrera *et al.*, 2007), nanotube and graphene hybrids and yarns (Foroughi *et al.*, 2014), nanosponges (Hashim *et al.*, 2012), a carbon kagome lattice (Chen *et al.*, 2014), and *rebar* graphene (Yan *et al.*, 2014), etc., as recently discussed in the literature (Lv, Cruz-Silva, and Terrones, 2014).

Another nanostructured carbon solid is the so-called Schwarzite family of materials. These materials are considered to be the 3D counterparts of fullerenes and they differ from other carbon sp^2 nanostructures by their hyperbolic geometry (i.e., non-Euclidean geometry as in graphene, nanotubes, and nanoribbons) with a negative Gaussian

curvature (Mackay and Terrones, 1991; Terrones and Terrones, 2003). Recent calculations revealed that the electronic band structure of Schwarzites can present 3D massless Dirac fermions (Lherbier, Terrones, and Charlier, 2014), depending on the material density (Owens *et al.*, 2016). This result is to be contrasted with the properties of graphene and metallic carbon nanotubes, which are characterized by 2D and 1D Dirac fermions, respectively. Besides the inherent difficulty to obtain Schwarzites in the laboratory, their predicted properties indicate how their geometry is expected to play a key role in defining the electronic properties of sp^2-like carbons, which opens up the possibility of having 3D massless fermions with new interesting physics to be exploited in the future. A number of periodic porous carbon structures similar to Schwarzites have already been experimentally produced (Kaneda *et al.*, 2002; Zhang, Yu, and Braun, 2011) and recent advances in templated nanocarbons synthesis (Kaneda *et al.*, 2002; Nishihara and Kyotani, 2012) and liquid exfoliation techniques (Nicolosi *et al.*, 2013) indicate the possibility of enhanced control in their fabrication. For example, recent experimental work shows great promise in this direction with the fabrication of a number of Schwarzite-like structures with mesoporous features (Werner, Hoheisel, and Wiesner, 2014).

VII. CONCLUDING REMARKS

Known carbon nanostructures span all possible spatial dimensions from 0D to 3D and exhibit properties intimately related to different manifestations of quantum mechanics in spatially confined structures. The discovery of fullerenes (0D) (Kroto *et al.*, 1985), carbon nanotubes (1D) (Iijima, 1991), and subsequent isolation of graphene (2D) from graphite (Novoselov *et al.*, 2004) has complemented the carbon allotrope family tree, long solely occupied by traditional 3D forms of carbon (graphite and diamond). Discoveries made over the past 30 years have unveiled a number of emerging phenomena and paved the way to the possibility of devising a spectrum of diverse applications using carbon nanostructures as their active materials with ever-increasing complexity and capabilities.

A. Carbon in modern history

Let us now consider the future of research and applications of nanocarbons from a broader historical perspective. Two objectives that have dominated societal goals in the past 70 years are space exploration and the continued implementation of Moore's law. Carbon, and sp^2 carbon, in particular, has played a central role in both areas.

Researchers working in the 1950s and 1960s already recognized that materials based on group IV elements in the periodic table were special. Carbon, silicon, and germanium were all discussed as materials of choice for the emerging semiconductor electronics industry. This interest was stimulated by early efforts to make diodes and other such devices during World War II. At first germanium was studied as a candidate material for electronics, while carbon and silicon were thought to have complicated electronic band structures and were classified along with III-V compound semiconductors as "materials of the future." The space program, however, had an easier choice. The uniqueness of sp^2 carbons as strong, lightweight materials made them an obvious option as model systems for the space program. This launched the modern sp^2 carbon industry as we know it today.

In the 1950s and 1960s, when the modern semiconductor industry was still in its infancy, preference was initially given to germanium, but soon practical considerations by engineers for rapid, large-scale manufacturing dominated the decision to choose silicon for commercial implementation. Semiconductor electronics started growing quickly from the 1950s. Industrial laboratories were set up to attract talented scientists and train new personnel and were the major drivers of scientific progress. The strong and growing international research community showed that scientists and engineers could all cope with designing silicon processing procedures and with manufacturing silicon-based working devices on a commercial scale. It was in this way that the semiconductor electronics revolution started. Thus, silicon was chosen in large-scale manufacturing for semiconductor devices. It remains to this day as the dominant material in the large-scale semiconductor industry.

By the 1970s, nanoscience was already discussed in the literature and at conferences. Both major semiconductor companies and the military started industrial planning for the future. Because of the large cadre of trained scientists, engineers, and technicians entering the workforce internationally, the transition to nanoscience occurred gradually with plans and programs established in many countries involved in the Cold War of the 1970s and 1980s. The year 1990 was in advance declared to be the year of nanoscience in the United States and in some other countries, including Japan. The year of the discovery of carbon nanotubes and the rapid growth of the nanocarbon research community officially started in 1991. Iijima and his team at the NEC Corporation were recognized by many people worldwide for their discovery of carbon nanotubes, first multiwall tubes in 1991 and then single-wall tubes in 1993 (Iijima, 1991; Iijima and Ichihashi, 1993). IBM laboratories came out with commercial nanotubes at the same time. Many others worldwide produced publications and developed expertise on this general topic, going back to the Russian literature of the 1950s and the German literature of the 1960s, but to our knowledge it was not pursued in depth at these early times.

The success in preparing single-layer graphene by Novoselov and Geim in 2004 ushered in a new nanocarbon era, starting with the simple layered two-dimensional material, monolayer graphene (Novoselov *et al.*, 2004). From a historical standpoint, graphene was already prepared and reported in the literature in 1960 by Boehm in Germany but not pursued beyond a few publications (Boehm *et al.*, 1962), and by scientists in the research field in Russia in the 1950s, but this work did not attract much attention from the scientific community at that time.

The last decade has seen the establishment of nanocarbon materials as prototypes for the frenetic development of nanoscience and nanotechnology and, more generally, for the description of a number of newly discovered exotic effects in condensed matter physics. Nanocarbon materials occupy this special place owing to the opportunity they provide to controllably perform many experiments in reduced

dimensions (2D—graphene and 1D—nanoribbons, nanotubes, and nanochains) based on ideal model systems. The physical properties of these structures are now well understood, and the field has reached a point where these basic building blocks can be combined and integrated with other layered materials for rational functional design of materials and devices far beyond past possibilities in quality, performance, control, and functionality.

New categories of carbon nanomaterials have also been identified. Some of them have been theoretically proposed while others have already been prepared and studied in the laboratory. The remarkable development of high-resolution experimental techniques in both the space and time domains along with the increasing capability of modeling have been—and will continue to be—instrumental in revealing novel physical behaviors in the nanoworld. Recent techniques include development of optical methods that operate beyond the diffraction limit (Ebbesen *et al.*, 1998; Gramotnev and Bozhevolnyi, 2010; Hell, 2015) and that have opened up promising new research directions. It is expected that the myriad of properties presently found in nanocarbon materials and in the hybrid systems that they form with other nanoscale systems will contribute to addressing many challenges of condensed matter physics in this decade of 2010–2020. In parallel, the applications of these properties can be expected to lead to the development of new avenues for technological breakthroughs. Nanocarbon materials will be steadily incorporated into everyday consumer products as large-scale production will reduce processing cost to become increasingly competitive in the mainstream electronic marketplace.

B. Beyond graphene

The research activity inspired by the tremendous development of graphene science and extended to other layered materials is now known broadly as the *beyond graphene* science (Bhimanapati *et al.*, 2015; Ferrari *et al.*, 2015). Similar to graphene that is fundamentally different from graphite, each layered material, when thinned down to its few-layer physical limits, exhibits additional properties that are strikingly different from its bulk counterpart. This spectacular effect is the result of strong confinement in two dimensions and yields a plethora of attractive phenomena that can be exploited in applications such as electronics, optoelectronics, electrochemistry, and biomedicine among others.

The beyond graphene new research direction has been developing at a very fast pace worldwide and is certain to have tremendous impact on many subfields within condensed matter physics and to have the potential of once again revolutionizing this field of research as has occurred several times before in the 20th century. These expectations stem from the large number of degrees of freedom offered by the choice of chemical elements and lattice space groups, not only in monoelemental systems (e.g., phosphorene, silicene) but also in binary (e.g., MoS_2, Bi_2Te_3) and tertiary (e.g., $CrSiTe_3$) systems. The choice and combination of chemical elements can yield an increasingly large variety of materials and structures, each having different properties, including anisotropic and more specialized response to external stimuli as well as emerging complex physical phenomena. In addition, thanks to their unique wide range of electron-phonon-coupling conditions that can occur as the chemical composition varies, control of the mean-free path for the carriers of electronic current and the carriers of thermal energy can be independently controlled to some extent, well beyond what can usually be accomplished in more traditional materials governed by the Wiedemann-Franz law.

C. Outlook

Graphene has truly emerged as a model system, owing to the extensive research devoted to it, both experimentally and theoretically, to advance its understanding and utilization. A number of issues have been raised and recent findings have contributed to shape a set of as yet unanswered research questions regarding special opportunities offered by further studies of graphene and other layered materials and other low-dimensional systems. Researchers must shift some of their attention to address these new questions that can now be explored thanks to all the knowledge developed for graphene and related materials. Some of these questions include the following: What new techniques are becoming available that expand knowledge, provide new opportunities, and open new vistas for science and can be more profitably studied in different layered materials? How can we further improve nanocarbon synthesis and fabrication techniques in order to allow for the development of higher quality samples on a larger scale? What are the possibilities to construct novel nanoscale architectures by combining different layered materials with sp^2 nanocarbons, and what new fundamental science can be explored with such new structures? Other questions relate to how the details of materials interactions with their environment govern the physical processes relevant to the measurement of macroscopic properties, such as I-V curves, photoluminescence spectra, etc. Important advances to these fields have indeed occurred through the introduction of few-layered and monolayered nanomaterials since 2010, when the Nobel Prize was awarded for graphene research, and can further shape the future of nanoscience and nanotechnology and related technologies.

The history of science has repeatedly shown the prominent role played by the introduction of new materials and new experimental and theoretical techniques along with serendipity in opening new research fields to advancing science and the subsequent utilization of the new science in applications of use to society. Based on all the advances made thus far in understanding the physical properties of nanocarbons, it is reasonable to foresee a bright future for these unique materials in a variety of fields, especially in condensed matter physics but also in chemistry, materials science, biology, biochemistry, medicine, and technology.

A possible research direction would be to use more of the different varieties of carbon materials that have recently been explored including the so-called Q carbon (Narayan and Bhaumik, 2015). As another example, carbon nanoribbons have been used as electrodes for nanoscale electronic circuits (Vicarelli *et al.*, 2015), but quantitative studies of the role of the edges of the graphene electrodes on the electronic properties of the nanocircuit that are now being studied for device applications still require more detailed fundamental study for establishing standards for the performance measurement of

commercial products involving few-layered active electronic elements (Fiori *et al.*, 2014). The fact that the edge of nanoribbons can provide spin-polarized states can be exploited to manipulate spin current. For instance, spin currents may lead to the possibility of studying spin injection processes in new ways for advancing nanoelectronics. Spin currents also present tremendous potential for advancing the development of noninvasive surface probes for biological systems. It is also expected that the bottom-up development for assembling carbon nanoribbons and doped carbon nanoribbons into a variety of geometries with specially designed edges and widths will play an important role in terms of controlling both charge and spin current, thereby opening up new possibilities for device applications.

ACKNOWLEDGMENTS

We acknowledge Professor Marija Drndić for her critical comments on the manuscript. V. M. is supported by NSF under Grant No. EFRI-2DARE 1542707, and by a travel grant by CAPES through the Science Without Borders program (Project No. A085/2013). A. G. S. F. and E. B. B. acknowledge funding from the Brazilian agencies CNPq, CAPES, and CNPq-MIT Joint Agreement. A. G. S. F. acknowledges CNPq (Grant No. 307317/2010-2 and INCT NanoBioSimes) and Fundacão Cearense de Apoio ao Desenvolvimento Cientifico e Tecnológico (FUNCAP) through PRONEX (Grant No. PR2-0054-00022.01.00/11) and INCT NANOBIOSIMES. M. S. D. acknowledges financial support from NSF Grants No. DMR-1004147 and No. DMR-1507806.

REFERENCES

Ajayan, P. M., and B. I. Yakobson, 2011, Nat. Mater. **10**, 415.
Akturk, A., and N. Goldsman, 2008, J. Appl. Phys. **103**, 053702.
Al-Backri, A., V. Zlyomi, and C. Lambert, 2014, J. Chem. Phys. **140**, 104306.
Al-Dirini, F., F. M. Hossain, A. Nirmalathas, and E. Skafidas, 2014, Sci. Rep. **4**, 3983.
Amorim, R. G., A. Fazzio, A. Antonelli, F. D. Novaes, and A. J. R. da Silva, 2007, Nano Lett. **7**, 2459.
Ando, T., and T. Nakanishi, 1998, J. Phys. Soc. Jpn. **67**, 1704.
Ando, T., T. Nakanishi, and R. Saito, 1998, J. Phys. Soc. Jpn. **67**, 2857.
Andrade, N., T. Vasconcelos, C. Gouvea, B. Archanjo, C. Achete, Y. Kim, M. Endo, C. Fantini, M. Dresselhaus, and A. S. Filho, 2015, Carbon **90**, 172.
Andrade, N. F., A. L. Aguiar, Y. A. Kim, M. Endo, P. T. C. Freire, G. Brunetto, D. S. Galvo, M. S. Dresselhaus, and A. G. Souza Filho, 2015, J. Phys. Chem. C **119**, 10669.
Appenzeller, J., R. Martel, P. Avouris, H. Stahl, and B. Lengeler, 2001, Appl. Phys. Lett. **78**, 3313.
Araujo, P. T., *et al.*, 2008, Phys. Rev. B **77**, 241403.
Araujo, P. T., *et al.*, 2012, Nano Lett. **12**, 4110.
Areshkin, D. A., D. Gunlycke, and C. T. White, 2007, Nano Lett. **7**, 204.
Ariel, V., and A. Natan, 2012, arXiv:1206.6100.
Arnold, M. S., A. A. Green, J. F. Hulvat, S. I. Stupp, and M. C. Hersam, 2006, Nat. Nanotechnol. **1**, 60.
Artyukhov, V. I., M. Liu, and B. I. Yakobson, 2014, Nano Lett. **14**, 4224.
Avouris, P., Z. H. Chen, and V. Perebeinos, 2007, Nat. Nanotechnol. **2**, 605.
Azoubel, S., S. Shemesh, and S. Magdassi, 2012, Nanotechnology **23**, 344003.
Bachtold, A., M. Fuhrer, S. Plyasunov, M. Forero, E. Anderson, A. Zettl, and P. McEuen, 2000, Phys. Rev. Lett. **84**, 6082.
Bachtold, A., P. Hadley, T. Nakanishi, and C. Dekker, 2001, Science **294**, 1317.
Bandaru, P. R., 2007, J. Mater. Sci. **42**, 1809.
Banhart, F., 1999, Rep. Prog. Phys. **62**, 1181.
Banhart, F., J. Kotakoski, and A. V. Krasheninnikov, 2011, ACS Nano **5**, 26.
Banhart, F., J. Li, and A. Krasheninnikov, 2005, Phys. Rev. B **71**, 241408.
Bao, W., F. Miao, Z. Chen, H. Zhang, W. Jang, C. Dames, and C. N. Lau, 2009, Nat. Nanotechnol. **4**, 562.
Barboza, A. P. M., M. H. D. Guimaraes, D. V. P. Massote, L. C. Campos, N. M. B. Neto, L. G. Cancado, R. G. Lacerda, H. Chacham, M. S. C. Mazzoni, and B. R. A. Neves, 2011, Adv. Mater. **23**, 3014.
Baringhaus, J., *et al.*, 2014, Nature (London) **506**, 349.
Barros, E. B., and M. S. Dresselhaus, 2014, Phys. Rev. B **90**, 035443.
Barros, E. B., A. Jorio, G. G. Samsonidze, R. B. Capaz, A. G. Souza Filho, J. Mendes Filho, G. Dresselhaus, and M. S. Dresselhaus, 2006, Phys. Rep. **431**, 261.
Baskin, A., and P. Kral, 2011, Sci. Reports **1**, 36.
Baughman, R. H., *et al.*, 1999, Science **284**, 1340.
Beams, R., L. G. Canado, and L. Novotny, 2015, J. Phys. Condens. Matter **27**, 083002.
Behabtu, N., *et al.*, 2013, Science **339**, 182.
Behnam, A., *et al.*, 2013, ACS Nano **7**, 482.
Bennett, P. B., Z. Pedramrazi, A. Madani, Y. C. Chen, D. G. de Oteyza, C. Chen, F. R. Fischer, M. F. Crommie, and J. Bokor, 2013, Appl. Phys. Lett. **103**, 253114.
Berger, C., P. Poncharal, Y. Yi, and W. de Heer, 2003, J. Nanosci. Nanotechnol. **3**, 171.
Berger, C., Y. Yi, Z. Wang, and W. de Heer, 2002, Appl. Phys. A **74**, 363.
Berger, C., *et al.*, 2006, Science **312**, 1191.
Bernholc, J., D. Brenner, M. Buongiorno Nardelli, V. Meunier, and C. Roland, 2002, Annu. Rev. Mater. Res. **32**, 347.
Bhimanapati, G. R., *et al.*, 2015, ACS Nano **9**, 11509.
Biel, B., X. Blase, F. Triozon, and S. Roche, 2009, Phys. Rev. Lett. **102**, 096803.
Biercuk, M., N. Mason, J. Martin, A. Yacoby, and C. Marcus, 2005, Phys. Rev. Lett. **94**, 026801.
Biercuk, M. J., S. Ilani, C. M. Marcus, and P. L. McEuen, 2008, in *Carbon Nanotubes*, Topics in Applied Physics, Vol. 111 (Springer-Verlag, Berlin), pp. 455–493.
Biswas, C., and Y. H. Lee, 2011, Adv. Funct. Mater. **21**, 3806.
Björk, J., S. Stafström, and F. Hanke, 2011, J. Am. Chem. Soc. **133**, 14884.
Blankenburg, S., J. M. Cai, P. Ruffieux, R. Jaafar, D. Passerone, X. L. Feng, K. Mullen, R. Fasel, and C. A. Pignedoli, 2012, ACS Nano **6**, 2020.
Bockrath, M., D. Cobden, J. Lu, A. Rinzler, R. Smalley, L. Balents, and P. McEuen, 1999, Nature (London) **397**, 598.
Bockrath, M., D. Cobden, P. McEuen, N. Chopra, A. Zettl, A. Thess, and R. Smalley, 1997, Science **275**, 1922.
Boehm, H. P., A. Clauss, G. O. Fischer, and U. Hofmann, 1962, Z. Anorg. Allg. Chem. **316**, 119.
Bolotin, K. I., K. J. Sikes, J. Hone, H. L. Stormer, and P. Kim, 2008, Phys. Rev. Lett. **101**, 096802.

Bolotin, K. I., K. J. Sikes, Z. Jiang, M. Klima, G. Fudenberg, J. Hone, P. Kim, and H. L. Stormer, 2008, Solid State Commun. **146**, 351.

Botello-Mendez, A. R., E. Cruz-Silva, F. Lopez-Urias, B. G. Sumpter, V. Meunier, M. Terrones, and H. Terrones, 2009, ACS Nano **3**, 3606.

Botello-Mendez, A. R., E. Cruz-Silva, J. M. Romo-Herrera, F. Lopez-Urias, M. Terrones, B. G. Sumpter, H. Terrones, J. C. Charlier, and V. Meunier, 2011, Nano Lett. **11**, 3058.

Botello-Mendez, A. R., X. Declerck, M. Terrones, H. Terrones, and J. C. Charlier, 2011, Nanoscale **3**, 2868.

Britnell, L., *et al.*, 2012, Science **335**, 947.

Britnell, L., *et al.*, 2013, Science **340**, 1311.

Bronner, C., S. Stremlau, M. Gille, F. Brauße, A. Haase, S. Hecht, and P. Tegeder, 2013, Angew. Chem., Int. Ed. Engl. **52**, 4422.

Brown, S., A. Jorio, P. Corio, M. Dresselhaus, G. Dresselhaus, R. Saito, and K. Kneipp, 2001, Phys. Rev. B **63**, 155414.

Bullard, Z., E. C. Girao, C. Daniels, B. G. Sumpter, and V. Meunier, 2014, Phys. Rev. B **89**, 245425.

Bullard, Z., and V. Meunier, 2013, Phys. Rev. B **88**, 035422.

Bunch, J., Y. Yaish, M. Brink, K. Bolotin, and P. McEuen, 2005, Nano Lett. **5**, 287.

Buongiorno Nardelli, M., B. I. Yakobson, and J. Bernholc, 1998, Phys. Rev. B **57**, R4277.

Cai, J., *et al.*, 2010, Nature (London) **466**, 470.

Cai, J., *et al.*, 2014, Nat. Nanotechnol. **9**, 896.

Calado, V. E., S.-E. Zhu, S. Goswami, Q. Xu, K. Watanabe, T. Taniguchi, G. C. A. M. Janssen, and L. M. K. Vandersypen, 2014, Appl. Phys. Lett. **104**, 023103.

Cancado, L., *et al.*, 2004, Phys. Rev. Lett. **93**, 047403.

Cantele, G., Y. S. Lee, D. Ninno, and N. Marzari, 2009, Nano Lett. **9**, 3425.

Cao, Q., S. J. Han, G. S. Tulevski, Y. Zhu, D. D. Lu, and W. Haensch, 2013, Nat. Nanotechnol. **8**, 180.

Cao, Q., H. S. Kim, N. Pimparkar, J. P. Kulkarni, C. J. Wang, M. Shim, K. Roy, M. A. Alam, and J. A. Rogers, 2008, Nature (London) **454**, 495.

Carozo, V., C. M. Almeida, E. H. M. Ferreira, L. G. Cancado, C. A. Achete, and A. Jorio, 2011, Nano Lett. **11**, 4527.

Carozo, V., *et al.*, 2013, Phys. Rev. B **88**, 085401.

Carvalho, A. R., J. H. Warnes, and C. H. Lewenkopf, 2014, Phys. Rev. B **89**, 245444.

Casillas, G., A. Mayoral, M. Liu, A. Ponce, V. I. Artyukhov, B. I. Yakobson, and M. Jose-Yacaman, 2014, Carbon **66**, 436.

Castro, E. V., H. Ochoa, M. I. Katsnelson, R. V. Gorbachev, D. C. Elias, K. S. Novoselov, A. K. Geim, and F. Guinea, 2010, Phys. Rev. Lett. **105**, 266601.

Castro Neto, A. H., N. M. R. Peres, K. S. Novoselov, and A. K. Geim, 2009, Rev. Mod. Phys. **81**, 109.

Cataldo, F., 2006, J. Am. Chem. Soc. **128**, 8987.

Chai, Y., A. Hazeghi, K. Takei, H. Y. Chen, P. C. H. Chan, A. Javey, and H. S. P. Wong, 2012, IEEE Trans. Electron Devices **59**, 12.

Charlier, J., T. Ebbesen, and P. Lambin, 1996, Phys. Rev. B **53**, 11108.

Charlier, J.-C., X. Blase, and S. Roche, 2007, Rev. Mod. Phys. **79**, 677.

Cheianov, V. V., and V. I. Fal'ko, 2006, Phys. Rev. B **74**, 041403.

Chen, I.-W. P., Z. Liang, B. Wang, and C. Zhang, 2010, Carbon **48**, 1064.

Chen, J.-H., C. Jang, S. Xiao, M. Ishigami, and M. S. Fuhrer, 2008, Nat. Nanotechnol. **3**, 206.

Chen, Y., Y. Y. Sun, H. Wang, D. West, Y. Xie, J. Zhong, V. Meunier, M. L. Cohen, and S. B. Zhang, 2014, Phys. Rev. Lett. **113**, 085501.

Chen, Y.-C., T. Cao, C. Chen, Z. Pedramrazi, D. Haberer, G. de OteyzaDimas, F. R. Fischer, S. G. Louie, and M. F. Crommie, 2015, Nat. Nanotechnol. **10**, 156.

Chen, Z., J. Appenzeller, J. Knoch, Y. Lin, and P. Avouris, 2005, Nano Lett. **5**, 1497.

Chen, Z., Y.-M. Lin, M. J. Rooks, and P. Avouris, 2007, Physica (Amsterdam) **40E**, 228.

Chen, Z. P., W. C. Ren, L. B. Gao, B. L. Liu, S. F. Pei, and H. M. Cheng, 2011, Nat. Mater. **10**, 424.

Chico, L., V. Crespi, L. Benedict, S. Louie, and M. Cohen, 1996, Phys. Rev. Lett. **76**, 971.

Choi, H. J., J. Ihm, S. G. Louie, and M. L. Cohen, 2000, Phys. Rev. Lett. **84**, 2917.

Chou, S. G., *et al.*, 2005, Phys. Rev. B **72**, 195415.

Costa Girão, E., L. Liang, E. Cruz-Silva, A. G. S. Filho, and V. Meunier, 2011, Phys. Rev. Lett. **107**, 135501.

Cresti, A., N. Nemec, B. Biel, G. Niebler, F. Triozon, G. Cuniberti, and S. Roche, 2008, Nano Res. **1**, 361.

Cresti, A., and S. Roche, 2009, New J. Phys. **11**, 095004.

Cretu, O., A. R. Botello-Mendez, I. Janowska, C. Pham-Huu, J.-C. Charlier, and F. Banhart, 2013, Nano Lett. **13**, 3487.

Cronin, S., A. Swan, M. Unlu, B. Goldberg, M. Dresselhaus, and M. Tinkham, 2004, Phys. Rev. Lett. **93**, 167401.

Cronin, S., A. Swan, M. Unlu, B. Goldberg, M. Dresselhaus, and M. Tinkham, 2005, Phys. Rev. B **72**, 035425.

Cruz-Silva, E., Z. M. Barnett, B. G. Sumpter, and V. Meunier, 2011, Phys. Rev. B **83**, 155445.

Cruz-Silva, E., A. R. Botello-Mendez, Z. M. Barnett, X. Jia, M. S. Dresselhaus, H. Terrones, M. Terrones, B. G. Sumpter, and V. Meunier, 2010, Phys. Rev. Lett. **105**, 045501.

Cruz-Silva, E., F. Lopez-Urias, E. Munoz-Sandoval, B. G. Sumpter, H. Terrones, J.-C. Charlier, V. Meunier, and M. Terrones, 2009, ACS Nano **3**, 1913.

Cruz-Silva, E., F. Lopez-Urias, E. Munoz-Sandoval, B. G. Sumpter, H. Terrones, J.-C. Charlier, V. Meunier, and M. Terrones, 2011, Nanoscale **3**, 1008.

Cui, X., M. Freitag, R. Martel, L. Brus, and P. Avouris, 2003, Nano Lett. **3**, 783.

Damnjanovic, M., I. Milosevic, T. Vukovic, and R. Sredanovic, 1999, Phys. Rev. B **60**, 2728.

Das Sarma, S., S. Adam, E. H. Hwang, and E. Rossi, 2011, Rev. Mod. Phys. **83**, 407.

Dean, C. R., *et al.*, 2010, Nat. Nanotechnol. **5**, 722.

Derycke, V., R. Martel, J. Appenzeller, and P. Avouris, 2001, Nano Lett. **1**, 453.

Dimiev, A., D. V. Kosynkin, A. Sinitskii, A. Slesarev, Z. Z. Sun, and J. M. Tour, 2011, Science **331**, 1168.

Do, J.-W., N. N. Chang, D. Estrada, F. Lian, H. Cha, X. J. Duan, R. T. Haasch, E. Pop, G. S. Girolami, and J. W. Lyding, 2015, ACS Nano **9**, 4806.

Dresselhaus, M., G. Dresselhaus, R. Saito, and A. Jorio, 2005, Phys. Rep. **409**, 47.

Dresselhaus, M., A. Jorio, and R. Saito, 2010, Annu. Rev. Condens. Matter Phys. **1**, 89.

Dresselhaus, M. S., and G. Dresselhaus, 1981, Adv. Phys. **30**, 139.

Dresselhaus, M. S., G. Dresselhaus, K. Sugihara, I. L. Spain, and H. A. Goldberg, 1988, *Graphite Fibers and Filaments* (Springer-Verlag, Berlin).

Du, X., I. Skachko, A. Barker, and E. Y. Andrei, 2008, Nat. Nanotechnol. **3**, 491.

Dubay, O., and G. Kresse, 2003, Phys. Rev. B **67**, 035401.

Dubay, O., G. Kresse, and H. Kuzmany, 2002, Phys. Rev. Lett. **88**, 235506.

Dubois, S. M., A. Lopez-Bezanilla, A. Cresti, F. Triozon, B. Biel, J. Charlier, and S. Roche, 2010, ACS Nano **4**, 1971.

Dubois, S. M. M., Z. Zanolli, X. Declerck, and J. C. Charlier, 2009, Eur. Phys. J. B **72**, 1.

Duque, J. G., H. Chen, A. K. Swan, A. P. Shreve, S. Kilina, S. Tretiak, X. Tu, M. Zheng, and S. K. Doorn, 2011, ACS Nano **5**, 5233.

Durkop, T., S. Getty, E. Cobas, and M. Fuhrer, 2004, Nano Lett. **4**, 35.

Ebbesen, T. W., H. J. Lezec, H. F. Ghaemi, T. Thio, and P. A. Wolff, 1998, Nature (London) **391**, 667.

Ebbesen, T. W., H. J. Lezec, H. Hiura, J. W. Bennett, H. F. Ghaemi, and T. Thio, 1996, Nature (London) **382**, 54.

Eckmann, A., A. Felten, A. Mishchenko, L. Britnell, R. Krupke, K. S. Novoselov, and C. Casiraghi, 2012, Nano Lett. **12**, 3925.

Efetov, D. K., and P. Kim, 2010, Phys. Rev. Lett. **105**, 256805.

Elias, D. C., *et al.*, 2009, Science **323**, 610.

Endo, M., T. Hayashi, H. Muramatsu, Y. Kim, H. Terrones, M. Terrones, and M. Dresselhaus, 2004, Nano Lett. **4**, 1451.

Endo, M., Y. A. Kim, T. Hayashi, H. Muramatsu, M. Terrones, R. Saito, F. Villalpando-Paez, S. G. Chou, and M. S. Dresselhaus, 2006, Small **2**, 1031.

Engelund, M., J. A. Furst, A. P. Jauho, and M. Brandbyge, 2010, Phys. Rev. Lett. **104**, 036807.

Enoki, T., Y. Kobayashi, and K.-I. Fukui, 2007, Int. Rev. Phys. Chem. **26**, 609.

Evaldsson, M., I. V. Zozoulenko, H. Y. Xu, and T. Heinzel, 2008, Phys. Rev. B **78**, 161407.

Ezawa, M., 2007, AIP Conf. Proc. **893**, 1015.

Fantini, C., *et al.*, 2006, Phys. Rev. B **73**, 193408.

Farhat, H., H. Son, G. Samsonidze, S. Reich, M. Dresselhaus, and J. Kong, 2007, Phys. Rev. Lett. **99**, 145506.

Fasolino, A., J. H. Los, and M. I. Katsnelson, 2007, Nat. Mater. **6**, 858.

Ferrari, A. C., *et al.*, 2015, Nanoscale **7**, 4598.

Ferry, D. K., S. M. Goodnick, and J. Bird, 2009, *Transport in Nanostructures* (Cambridge University Press, Cambridge, England), 2nd ed.

Fiori, G., F. Bonaccorso, G. Iannaccone, T. Palacios, D. Neumaier, A. Seabaugh, S. K. Banerjee, and L. Colombo, 2014, Nat. Nanotechnol. **9**, 768.

Fischbein, M., and M. Drndic, 2006, Appl. Phys. Lett. **88**, 063116.

Flores, F., B. Biel, A. Rubio, F. J. Garcia-Vidal, C. Gomez-Navarro, P. de Pablo, and J. Gomez-Herrero, 2008, J. Phys. Condens. Matter **20**, 304211.

Foa Torres, L., S. Roche, and J.-C. Charlier, 2014, *Introduction to Graphene-Based Nanomaterials: From Electronic Structure to Quantum Transport* (Cambridge University Press, Cambridge, England).

Foroughi, J., *et al.*, 2014, Adv. Funct. Mater. **24**, 5859.

Frank, O., G. Tsoukleri, I. Riaz, K. Papagelis, J. Parthenios, A. C. Ferrari, A. K. Geim, K. S. Novoselov, and C. Galiotis, 2011, Nat. Commun. **2**, 255.

Frank, O., J. Vejpravova, V. Holy, L. Kavan, and M. Kalbac, 2014, Carbon **68**, 440.

Franklin, A. D., D. B. Farmer, and W. Haensch, 2014, ACS Nano **8**, 7333.

Franklin, A. D., M. Luisier, S.-J. Han, G. Tulevski, C. M. Breslin, L. Gignac, M. S. Lundstrom, and W. Haensch, 2012, Nano Lett. **12**, 758.

Franklin, A. D., G. S. Tulevski, S.-J. Han, D. Shahrjerdi, Q. Cao, H.-Y. Chen, H. S. P. Wong, and W. Haensch, 2012, ACS Nano **6**, 1109.

Freitag, M., J. C. Tsang, A. Bol, P. Avouris, D. N. Yuan, and J. Liu, 2007, Appl. Phys. Lett. **91**, 031101.

Fuhrer, M., B. Kim, T. Durkop, and T. Brintlinger, 2002, Nano Lett. **2**, 755.

Fuhrer, M. S., 2010, Physics **3**, 106.

Fujita, M., K. Wakabayashi, K. Nakada, and K. Kusakabe, 1996, J. Phys. Soc. Jpn. **65**, 1920.

Gartstein, Y. N., A. A. Zakhidov, and R. H. Baughman, 2003, Phys. Rev. B **68**, 115415.

Geier, M. L., J. J. McMorrow, W. Xu, J. Zhu, C. H. Kim, T. J. Marks, and M. C. Hersam, 2015, Nat. Nanotechnol. **10**, 944.

Geim, A. K., and K. S. Novoselov, 2007, Nat. Mater. **6**, 183.

Ghosh, S., S. M. Bachilo, and R. B. Weisman, 2010, Nat. Nanotechnol. **5**, 443.

Gillen, R., M. Mohr, C. Thomsen, and J. Maultzsch, 2009, Phys. Rev. B **80**, 155418.

Girão, E. C., L. Liang, J. Owens, E. Cruz-Silva, B. G. Sumpter, and V. Meunier, 2013, "Electronic transport in graphitic carbon nanoribbons," in *Graphene Chemistry* (Wiley, New York), pp. 319–346.

Girit, Ç. Ö., *et al.*, 2009, Science **323**, 1705.

Gomez-Navarro, C., P. J. De Pablo, J. Gomez-Herrero, B. Biel, F. J. Garcia-Vidal, A. Rubio, and F. Flores, 2005, Nat. Mater. **4**, 534.

Gorjizadeh, N., A. A. Farajian, K. Esfarjani, and Y. Kawazoe, 2008, Phys. Rev. B **78**, 155427.

Gramich, J., A. Baumgartner, and C. Schonenberger, 2015, Phys. Rev. Lett. **115**, 216801.

Gramotnev, D. K., and S. I. Bozhevolnyi, 2010, Nat. Photonics **4**, 83.

Green, A. A., and M. C. Hersam, 2007, Mater. Today **10**, 59.

Green, A. A., and M. C. Hersam, 2009, Nano Lett. **9**, 4031.

Guan, L., K. Suenaga, T. Okazaki, Z. Shi, Z. Gu, and S. Iijima, 2007, J. Am. Chem. Soc. **129**, 8954.

Gunlycke, D., J. Li, J. W. Mintmire, and C. T. White, 2007, Appl. Phys. Lett. **91**, 112108.

Gunlycke, D., and C. T. White, 2008, Phys. Rev. B **77**, 115116.

Gupta, A. K., Y. Tang, V. H. Crespi, and P. C. Eklund, 2010, Phys. Rev. B **82**, 241406.

Gupta, S., M. Hughes, A. H. Windle, and J. Robertson, 2004, J. Appl. Phys. **95**, 2038.

Haldane, F., 1981, J. Phys. C **14**, 2585.

Han, M., B. Özyilmaz, Y. Zhang, and P. Kim, 2007, Phys. Rev. Lett. **98**, 206805.

Han, P., K. Akagi, F. Federici Canova, H. Mutoh, S. Shiraki, K. Iwaya, P. S. Weiss, N. Asao, and T. Hitosugi, 2014, ACS Nano **8**, 9181.

Hancock, Y., K. Saloriutta, A. Uppstu, A. Harju, and M. J. Puska, 2008, J. Low Temp. Phys. **153**, 393.

Hartman, A. Z., M. Jouzi, R. L. Barnett, and J. M. Xu, 2004, Phys. Rev. Lett. **92**, 236804.

Hashim, D. P., *et al.*, 2012, Sci. Rep. **2**, 363.

Haskins, J., A. Kinaci, C. Sevik, H. Sevincli, G. Cuniberti, and T. Cagin, 2011, ACS Nano **5**, 3779.

Hatanaka, M., 2010, Chem. Phys. Lett. **488**, 187.

Havener, R. W., H. Zhuang, L. Brown, R. G. Hennig, and J. Park, 2012, Nano Lett. **12**, 3162.

Heinze, S., J. Tersoff, R. Martel, V. Derycke, J. Appenzeller, and P. Avouris, 2002, Phys. Rev. Lett. **89**, 106801.

Hell, S. W., 2015, Rev. Mod. Phys. **87**, 1169.

Hernandez, E., V. Meunier, B. Smith, R. Rurali, H. Terrones, M. Buongiorno Nardelli, M. Terrones, D. Luzzi, and J. Charlier, 2003, Nano Lett. **3**, 1037.

Hofmann, P., 2011, *Solid State Physics: An Introduction* (Wiley, New York).

Huang, H., D. Wei, J. Sun, S. L. Wong, Y. P. Feng, A. H. C. Neto, and A. T. S. Wee, 2012, Sci. Rep. **2**, 983.
Huang, J. Y., F. Ding, B. I. Yakobson, P. Lu, L. Qi, and J. Li, 2009a, Proc. Natl. Acad. Sci. U.S.A. **106**, 10103.
Huang, J. Y., F. Ding, B. I. Yakobson, P. Lu, L. Qi, and J. Li, 2009b, Proc. Natl. Acad. Sci. U.S.A. **106**, 10103.
Huang, P. Y., *et al.*, 2011, Nature (London) **469**, 389.
Huang, S., X. Ling, L. Liang, Y. Song, W. Fang, J. Zhang, J. Kong, V. Meunier, and M. S. Dresselhaus, 2015, Nano Lett. **15**, 2892.
Huard, B., J. A. Sulpizio, N. Stander, K. Todd, B. Yang, and D. Goldhaber-Gordon, 2007, Phys. Rev. Lett. **98**, 236803.
Hunt, B., *et al.*, 2013, Science **340**, 1427.
Hwang, E. H., and S. Das Sarma, 2008, Phys. Rev. B **77**, 115449.
Iijima, S., 1991, Nature (London) **354**, 56.
Iijima, S., and T. Ichihashi, 1993, Nature (London) **363**, 603.
Ilani, S., L. A. K. Donev, M. Kindermann, and P. L. McEuen, 2006, Nat. Phys. **2**, 687.
Itkis, M. E., A. Pekker, X. J. Tian, E. Bekyarova, and R. C. Haddon, 2015, Acc. Chem. Res. **48**, 2270.
Jakubka, F., C. Backes, F. Gannott, U. Mundloch, F. Hauke, A. Hirsch, and J. Zaumseil, 2013, ACS Nano **7**, 7428.
Jalilian, R., L. A. Jauregui, G. Lopez, J. F. Tian, C. Roecker, M. M. Yazdanpanah, R. W. Cohn, I. Jovanovic, and Y. P. Chen, 2011, Nanotechnology **22**, 295705.
Jang, I., S. Sinnott, D. Danailov, and P. Keblinski, 2004, Nano Lett. **4**, 109.
Javey, A., J. Guo, M. Paulsson, Q. Wang, D. Mann, M. Lundstrom, and H. Dai, 2004, Phys. Rev. Lett. **92**, 106804.
Javey, A., J. Guo, Q. Wang, M. Lundstrom, and H. Dai, 2003, Nature (London) **424**, 654.
Jia, C. C., B. J. Ma, N. Xin, and X. F. Guo, 2015, Acc. Chem. Res. **48**, 2565.
Jia, X., J. Campos-Delgado, M. Terrones, V. Meunier, and M. S. Dresselhaus, 2011, Nanoscale **3**, 86.
Jia, X., *et al.*, 2009, Science **323**, 1701.
Jiang, J.-W., B.-S. Wang, J.-S. Wang, and H. S. Park, 2015, J. Phys. Condens. Matter **27**, 083001.
Jiao, L. Y., X. R. Wang, G. Diakonov, H. L. Wang, and H. J. Dai, 2010, Nat. Nanotechnol. **5**, 321.
Jinno, M., Y. Ando, S. Bandow, J. Fan, M. Yudasaka, and S. Iijima, 2006, Chem. Phys. Lett. **418**, 109.
Jishi, R., L. Venkataraman, M. Dresselhaus, and G. Dresselhaus, 1993, Chem. Phys. Lett. **209**, 77.
Jorio, A., M. S. Dresselhaus, R. Saito, and G. Dresselhaus, 2011, *Raman Spectroscopy in Graphene Related Systems* (Wiley, Weinheim).
Jorio, A., R. Saito, J. H. Hafner, C. M. Lieber, M. Hunter, T. McClure, G. Dresselhaus, and M. S. Dresselhaus, 2001, Phys. Rev. Lett. **86**, 1118.
Jovanović, S., T. Da Ross, a. Ostric, D. Tošić, J. Prekodravac, Z. Marković, and B. Todorović Marković, 2014, Phys. Scr. **T162**, 014023.
Jung, N., A. C. Crowther, N. Kim, P. Kim, and L. Brus, 2010, ACS Nano **4**, 7005.
Kane, C., *et al.*, 1998, Europhys. Lett. **41**, 683.
Kaneda, M., T. Tsubakiyama, A. Carlsson, Y. Sakamoto, T. Ohsuna, O. Terasaki, S. H. Joo, and R. Ryoo, 2002, J. Phys. Chem. B **106**, 1256.
Kang, J., J.-W. T. Seo, D. Alducin, A. Ponce, M. J. Yacaman, and M. C. Hersam, 2014, Nat. Commun. **5**, 5478.
Kang, J., S. A. Wells, J. D. Wood, J.-H. Lee, X. Liu, C. R. Ryder, J. Zhu, J. R. Guest, C. A. Husko, and M. C. Hersam, 2016, Proc. Natl. Acad. Sci. USA (to be published), doi:10.1073/pnas.1602215113.
Kano, E., M. Takeguchi, J.-i. F., and A. Hashimoto, 2014, Carbon **80**, 382.
Kastner, J., H. Kuzmany, L. Kavan, F. P. Dousek, and J. Kurti, 1995, Macromolecules **28**, 344.
Kasumov, A., R. Deblock, M. Kociak, B. Reulet, H. Bouchiat, I. Khodos, Y. Gorbatov, V. Volkov, C. Journet, and M. Burghard, 1999, Science **284**, 1508.
Katsnelson, M., 2012, *Graphene: Carbon in Two Dimensions* (Cambridge University Press, Cambridge, England).
Katsnelson, M. I., K. S. Novoselov, and A. K. Geim, 2006, Nat. Phys. **2**, 620.
Kertesz, M., and S. Yang, 2009, Phys. Chem. Chem. Phys. **11**, 425.
Kharche, N., Y. Zhou, K. P. O'Brien, S. Kar, and S. K. Nayak, 2011, ACS Nano **5**, 6096.
Kim, K., S. Coh, L. Z. Tan, W. Regan, J. M. Yuk, E. Chatterjee, M. F. Crommie, M. L. Cohen, S. G. Louie, and A. Zettl, 2012, Phys. Rev. Lett. **108**, 246103.
Kimouche, A., M. M. Ervasti, R. Drost, S. Halonen, A. Harju, P. M. Joensuu, J. Sainio, and P. Liljeroth, 2015, Nat. Commun. **6**, 10177.
Koch, M., F. Ample, C. Joachim, and L. Grill, 2012, Nat. Nanotechnol. **7**, 713.
Kong, J., E. Yenilmez, T. Tombler, W. Kim, H. Dai, R. Laughlin, L. Liu, C. Jayanthi, and S. Wu, 2001, Phys. Rev. Lett. **87**, 106801.
Koskinen, P., S. Malola, and H. Häkkinen, 2008, Phys. Rev. Lett. **101**, 115502.
Koskinen, P., S. Malola, and H. Häkkinen, 2009, Phys. Rev. B **80**, 073401.
Kosynkin, D. V., A. L. Higginbotham, A. Sinitskii, J. R. Lomeda, A. Dimiev, B. K. Price, and J. M. Tour, 2009, Nature (London) **458**, 872.
Kouwenhoven, L., and C. Marcus, 1998, Phys. World **11**, 35.
Koziol, K., J. Vilatela, A. Moisala, M. Motta, P. Cunniff, M. Sennett, and A. Windle, 2007, Science **318**, 1892.
Krasheninnikov, A. V., and F. Banhart, 2007, Nat. Mater. **6**, 723.
Kroto, H. W., J. R. Heath, S. C. Obrien, R. F. Curl, and R. E. Smalley, 1985, Nature (London) **318**, 162.
Krupke, R., F. Hennrich, H. von Lohneysen, and M. M. Kappes, 2003, Science **301**, 344.
Lahiri, J., Y. Lin, P. Bozkurt, I. I. Oleynik, and M. Batzill, 2010, Nat. Nanotechnol. **5**, 326.
Lambin, P., and V. Meunier, 1999, Appl. Phys. A **68**, 263.
Landauer, R., 1970, Philos. Mag. **21**, 863.
Larentis, S., J. R. Tolsma, B. Fallahazad, D. C. Dillen, K. Kim, A. H. Macdonald, and E. Tutuc, 2014, Nano Lett. **14**, 2039.
La Torre, A., A. Botello-Mendez, W. Baaziz, J. C. Charlier, and F. Banhart, 2015, Nat. Commun. **6**, 6636.
Lauginie, P., and J. Conard, 1997, J. Phys. Chem. Solids **58**, 1949.
Lee, J., I. Y. Stein, M. E. Devoe, D. J. Lewis, N. Lachman, S. S. Kessler, S. T. Buschhorn, and B. L. Wardle, 2015, Appl. Phys. Lett. **106**, 053110.
Lee, P. A., and T. V. Ramakrishnan, 1985, Rev. Mod. Phys. **57**, 287.
Lekawa-Raus, A., J. Patmore, L. Kurzepa, J. Bulmer, and K. Koziol, 2014, Adv. Funct. Mater. **24**, 3661.
Leonard, F., and J. Tersoff, 2000, Phys. Rev. Lett. **84**, 4693.
Lepro, X., Y. Vega-Cantu, F. J. Rodriguez-Macias, Y. Bando, D. Golberg, and M. Terrones, 2007, Nano Lett. **7**, 2220.
Lherbier, A., B. Biel, Y. M. Niquet, and S. Roche, 2008, Phys. Rev. Lett. **100**, 036803.
Lherbier, A., A. R. Botello-Méndez, and J.-C. Charlier, 2013, Nano Lett. **13**, 1446.
Lherbier, A., S. M. M. Dubois, X. Declerck, S. Roche, Y. M. Niquet, and J. C. Charlier, 2011, Phys. Rev. Lett. **106**, 046803.
Lherbier, A., H. Terrones, and J.-C. Charlier, 2014, Phys. Rev. B **90**, 125434.

Li, G., A. Luican, J. M. B. Lopes dos Santos, A. H. Castro Neto, A. Reina, J. Kong, and E. Y. Andrei, 2010, Nat. Phys. **6**, 109.

Li, L., S. Reich, and J. Robertson, 2005, Phys. Rev. B **72**, 184109.

Li, S., Z. Yu, C. Rutherglen, and P. Burke, 2004, Nano Lett. **4**, 2003.

Li, T. C., and S. P. Lu, 2008, Phys. Rev. B **77**, 085408.

Li, X., X. Wang, L. Zhang, S. Lee, and H. Dai, 2008, Science **319**, 1229.

Li, Y., X. Jiang, Z. Liu, and Z. Liu, 2010, Nano Res. **3**, 545.

Li, Y., Z. Zhou, C. R. Cabrera, and Z. Chen, 2013, Sci. Rep. **3**, 2030.

Li, Y. Y., M. X. Chen, M. Weinert, and L. Li, 2014, Nat. Commun. **5**, 4311.

Liang, L., E. Cruz-Silva, E. C. Girão, and V. Meunier, 2012, Phys. Rev. B **86**, 115438.

Liang, L., E. C. Girão, and V. Meunier, 2013, Phys. Rev. B **88**, 035420.

Liang, L., and V. Meunier, 2015, J. Phys. Chem. C **119**, 775.

Liang, W., M. Bockrath, D. Bozovic, J. Hafner, M. Tinkham, and H. Park, 2001, Nature (London) **411**, 665.

Liang, W., M. Bockrath, and H. Park, 2005, Annu. Rev. Phys. Chem. **56**, 475.

Liang, W. J., M. P. Shores, M. Bockrath, J. R. Long, and H. Park, 2002, Nature (London) **417**, 725.

Lin, J. J., L. B. Liang, X. Ling, S. Q. Zhang, N. N. Mao, N. Zhang, B. G. Sumpter, V. Meunier, L. M. Tong, and J. Zhang, 2015, J. Am. Chem. Soc. **137**, 15511.

Lin, X., and J. Ni, 2011, Phys. Rev. B **84**, 075461.

Lin, Y.-C., *et al.*, 2014, Nano Lett. **14**, 6936.

Linden, S., *et al.*, 2012, Phys. Rev. Lett. **108**, 216801.

Ling, X., L. G. Moura, M. A. Pimenta, and J. Zhang, 2012, J. Phys. Chem. C **116**, 25112.

Ling, X., L. Xie, Y. Fang, H. Xu, H. Zhang, J. Kong, M. S. Dresselhaus, J. Zhang, and Z. Liu, 2010, Nano Lett. **10**, 553.

Ling, X., and J. Zhang, 2010, Small **6**, 2020.

Liu, K., X. Hong, Q. Zhou, C. Jin, J. Li, W. Zhou, J. Liu, E. Wang, A. Zettl, and F. Wang, 2013, Nat. Nanotechnol. **8**, 917.

Liu, M., V. I. Artyukhov, H. Lee, F. Xu, and B. I. Yakobson, 2013, ACS Nano **7**, 10075.

Liu, M. H., P. Rickhaus, P. Makk, E. Tovari, R. Maurand, F. Tkatschenko, M. Weiss, C. Schonenberger, and K. Richter, 2015, Phys. Rev. Lett. **114**, 036601.

Liu, Z., Y.-C. Lin, C.-C. Lu, C.-H. Yeh, P.-W. Chiu, S. Iijima, and K. Suenaga, 2014, Nat. Commun. **5**, 4055.

Liu, Z., K. Suenaga, P. J. F. Harris, and S. Iijima, 2009, Phys. Rev. Lett. **102**, 015501.

Liu, Z., *et al.*, 2013, Nat. Nanotechnol. **8**, 119.

Longhurst, M. J., and N. Quirke, 2006, J. Chem. Phys. **125**, 184705.

Lopez-Bezanilla, A., F. Triozon, and S. Roche, 2009, Nano Lett. **9**, 2537.

Lopez-Bezanilla, A., *et al.*, 2012, J. Phys. Chem. Lett. **3**, 2097.

Lui, C. H., L. M. Malard, S. Kim, G. Lantz, F. E. Laverge, R. Saito, and T. F. Heinz, 2012, Nano Lett. **12**, 5539.

Lui, C. H., Z. Ye, C. Keiser, E. B. Barros, and R. He, 2015, Appl. Phys. Lett. **106**, 041904.

Luican, A., G. Li, A. Reina, J. Kong, R. R. Nair, K. S. Novoselov, A. K. Geim, and E. Y. Andrei, 2011, Phys. Rev. Lett. **106**, 126802.

Lv, R. T., E. Cruz-Silva, and M. Terrones, 2014, ACS Nano **8**, 4061.

Ma, Z., and W. Sheng, 2011, Appl. Phys. Lett. **99**, 083101.

Mackay, A., and H. Terrones, 1991, Nature (London) **352**, 762.

Magda, G. Z., X. Jin, I. Hagymasi, P. Vancso, Z. Osvath, P. Nemes-Incze, C. Hwang, L. P. Biro, and L. Tapaszto, 2014, Nature (London) **514**, 608.

Mahan, G. D., and S. J. Gun, 2004, Phys. Rev. B **70**, 075405.

Malard, L., M. Guimarães, D. Mafra, M. Mazzoni, and A. Jorio, 2009, Phys. Rev. B **79**, 125426.

Malard, L., M. Pimenta, G. Dresselhaus, and M. Dresselhaus, 2009, Phys. Rep. **473**, 51.

Mann, D., A. Javey, J. Kong, Q. Wang, and H. Dai, 2003, Nano Lett. **3**, 1541.

Martel, R., T. Schmidt, H. Shea, T. Hertel, and P. Avouris, 1998, Appl. Phys. Lett. **73**, 2447.

Martins, T. B., A. J. R. da Silva, R. H. Miwa, and A. Fazzio, 2008, Nano Lett. **8**, 2293.

Martins, T. B., R. H. Miwa, A. J. R. da Silva, and A. Fazzio, 2007, Phys. Rev. Lett. **98**, 196803.

Matsuda, Y., W. Q. Deng, and W. A. Goddard, 2010, J. Phys. Chem. C **114**, 17845.

Maultzsch, J., S. Reich, and C. Thomsen, 2002, Phys. Rev. B **65**, 233402.

Maultzsch, J., S. Reich, C. Thomsen, E. Dobardzic, I. Milosevic, and M. Damnjanovic, 2002, Solid State Commun. **121**, 471.

Maultzsch, J., S. Reich, C. Thomsen, H. Requardt, and P. Ordejo, 2004, Phys. Rev. Lett. **92**, 075501.

Mayorov, A. S., *et al.*, 2011, Nano Lett. **11**, 2396.

McEuen, P., M. Bockrath, D. Cobden, Y. Yoon, and S. Louie, 1999, Phys. Rev. Lett. **83**, 5098.

Meng, F., S. Shi, D. Xu, and R. Yang, 2006, Carbon **44**, 1263.

Meric, I., M. Y. Han, A. F. Young, B. Ozyilmaz, P. Kim, and K. L. Shepard, 2008, Nat. Nanotechnol. **3**, 654.

Metenier, K., S. Bonnamy, F. Beguin, C. Journet, P. Bernier, M. de La Chapelle, O. Chauvet, and S. Lefrant, 2002, Carbon **40**, 1765.

Meunier, V., S. V. Kalinin, and B. G. Sumpter, 2007, Phys. Rev. Lett. **98**, 056401.

Meunier, V., and P. Lambin, 2000, Carbon **38**, 1729.

Meyer, J. C., A. K. Geim, M. I. Katsnelson, K. S. Novoselov, T. J. Booth, and S. Roth, 2007, Nature (London) **446**, 60.

Meyer, J. C., C. O. Girit, M. F. Crommie, and A. Zettl, 2008a, Appl. Phys. Lett. **92**, 123110.

Meyer, J. C., C. O. Girit, M. F. Crommie, and A. Zettl, 2008b, Nature (London) **454**, 319.

Mintmire, J., and C. White, 1998, Phys. Rev. Lett. **81**, 2506.

Misewich, J. A., R. Martel, P. Avouris, J. C. Tsang, S. Heinze, and J. Tersoff, 2003, Science **300**, 783.

Mishchenko, A., *et al.*, 2014, Nat. Nanotechnol. **9**, 808.

Mohiuddin, T., *et al.*, 2009, Phys. Rev. B **79**, 205433.

Morozov, S. V., K. S. Novoselov, M. I. Katsnelson, F. Schedin, D. C. Elias, J. A. Jaszczak, and A. K. Geim, 2008, Phys. Rev. Lett. **100**, 016602.

Morpurgo, A., J. Kong, C. Marcus, and H. Dai, 1999, Science **286**, 263.

Moser, J., A. Barreiro, and A. Bachtold, 2007, Appl. Phys. Lett. **91**, 163513.

Mounet, N., and N. Marzari, 2005, Phys. Rev. B **71**, 205214.

Mucciolo, E. R., A. H. C. Neto, and C. H. Lewenkopf, 2009, Phys. Rev. B **79**, 075407.

Munoz-Rojas, F., J. Fernandez-Rossier, and J. J. Palacios, 2009, Phys. Rev. Lett. **102**, 136810.

Muramatsu, H., *et al.*, 2013, RSC Adv. **3**, 26266.

Nakada, K., M. Fujita, G. Dresselhaus, and M. Dresselhaus, 1996, Phys. Rev. B **54**, 17954.

Nakaharai, S., T. Iijima, S. Ogawa, S. Suzuki, S. L. Li, K. Tsukagoshi, S. Sato, and N. Yokoyama, 2013, ACS Nano **7**, 5694.

Nanot, S., E. H. Haroz, J. H. Kim, R. H. Hauge, and J. Kono, 2012, Adv. Mater. **24**, 4977.

Narayan, J., and A. Bhaumik, 2015, APL Mater. **3**, 100702.

Newaz, A. K. M., Y. S. Puzyrev, B. Wang, S. T. Pantelides, and K. I. Bolotin, 2012, Nat. Commun. **3**, 734.
Newson, R. W., J. M. Menard, C. Sames, M. Betz, and H. M. van Driel, 2008, Nano Lett. **8**, 1586.
Ni, Z. H., T. Yu, Y. H. Lu, Y. Y. Wang, Y. P. Feng, and Z. X. Shen, 2008, ACS Nano **2**, 2301.
Nicklow, R., N. Wakabayashi, and H. Smith, 1972, Phys. Rev. B **5**, 4951.
Nicolosi, V., M. Chhowalla, M. G. Kanatzidis, M. S. Strano, and J. N. Coleman, 2013, Science **340**, 1226419.
Nie, A., P. Wang, H. Wang, and S. X. Mao, 2010, Nanotechnology **21**, 245302.
Nishide, D., *et al.*, 2006, Chem. Phys. Lett. **428**, 356.
Nishihara, H., and T. Kyotani, 2012, Adv. Mater. **24**, 4473.
Novoselov, K., A. Geim, S. Morozov, D. Jiang, Y. Zhang, S. Dubonos, I. Grigorieva, and A. Firsov, 2004, Science **306**, 666.
Nygard, J., D. Cobden, and P. Lindelof, 2000, Nature (London) **408**, 342.
Oshima, C., T. Aizawa, R. Souda, Y. Ishizawa, and Y. Sumiyoshi, 1988, Solid State Commun. **65**, 1601.
Owens, J., C. Daniels, A. Nicola, H. Terrones, and V. Meunier, 2016, Carbon **96**, 998.
Owens, J. R., E. Cruz-Silva, and V. Meunier, 2013, Nanotechnology **24**, 235701.
Padilha, J. E., A. Fazzio, and A. J. R. da Silva, 2015, Phys. Rev. Lett. **114**, 066803.
Padilha, J. E., M. P. Lima, A. J. R. da Silva, and A. Fazzio, 2011, Phys. Rev. B **84**, 113412.
Palma, C.-A., and P. Samori, 2011, Nat. Chem. **3**, 431.
Pan, B., J. Xiao, J. Li, P. Liu, C. Wang, and G. Yang, 2015, Sci. Adv. **1**, e1500857.
Pan, M., E. C. Girão, X. Jia, S. Bhaviripudi, Q. Li, J. Kong, V. Meunier, and M. S. Dresselhaus, 2012, Nano Lett. **12**, 1928.
Park, J., *et al.*, 2012, Adv. Mater. **24**, 407.
Park, J. Y., S. Rosenblatt, Y. Yaish, V. Sazonova, H. Üstunel, S. Braig, T. a. Arias, P. W. Brouwer, and P. L. McEuen, 2004, Nano Lett. **4**, 517.
Partoens, B., and F. M. Peeters, 2007, Phys. Rev. B **75**, 193402.
Pastewka, L., P. Koskinen, C. Elsasser, and M. Moseler, 2009, Phys. Rev. B **80**, 155428.
Pedersen, T. G., C. Flindt, J. Pedersen, N. A. Mortensen, A.-P. Jauho, and K. Pedersen, 2008, Phys. Rev. Lett. **100**, 136804.
Pei, T., P. Zhang, Z. Zhang, C. Qiu, S. Liang, Y. Yang, S. Wang, and L.-M. Peng, 2014, Nano Lett. **14**, 3102.
Peimyoo, N., T. Yu, J. Shang, C. Cong, and H. Yang, 2012, Carbon **50**, 201.
Perebeinos, V., and J. Tersoff, 2009, Phys. Rev. B **79**, 241409.
Perebeinos, V., J. Tersoff, and P. Avouris, 2005, Phys. Rev. Lett. **94**, 027402.
Peres, N. M. R., 2010, Rev. Mod. Phys. **82**, 2673.
Piper, N. M., Y. Fu, J. Tao, X. Yang, and A. C. To, 2011, Chem. Phys. Lett. **502**, 231.
Pisana, S., M. Lazzeri, C. Casiraghi, K. S. Novoselov, A. K. Geim, A. C. Ferrari, and F. Mauri, 2007, Nat. Mater. **6**, 198.
Pisani, L., J. Chan, B. Montanari, and N. Harrison, 2007, Phys. Rev. B **75**, 064418.
Piscanec, S., M. Lazzeri, F. Mauri, A. Ferrari, and J. Robertson, 2004, Phys. Rev. Lett. **93**, 185503.
Piscanec, S., M. Lazzeri, J. Robertson, A. C. Ferrari, and F. Mauri, 2007, Phys. Rev. B **75**, 035427.
Plentz, F., H. Ribeiro, A. Jorio, M. Strano, and M. Pimenta, 2005, Phys. Rev. Lett. **95**, 247401.
Ponomarenko, L. A., F. Schedin, M. I. Katsnelson, R. Yang, E. W. Hill, K. S. Novoselov, and A. K. Geim, 2008, Science **320**, 356.
Ponomarenko, L. A., *et al.*, 2011, Nat. Phys. **7**, 958.
Pop, E., 2008, Nanotechnology **19**, 295202.
Pop, E., V. Varshney, and A. K. Roy, 2012, MRS Bull. **37**, 1273.
Popov, V. N., and C. Van Alsenoy, 2014, Phys. Rev. B **90**, 245429.
Postma, H., T. Teepen, Z. Yao, M. Grifoni, and C. Dekker, 2001, Science **293**, 76.
Qi, Z. J., C. Daniels, S. J. Hong, Y. W. Park, V. Meunier, M. Drndić, and A. T. C. Johnson, 2015, ACS Nano **9**, 3510.
Qi, Z. J., J. A. Rodriguez-Manzo, A. R. Botello-Mendez, S. J. Hong, E. A. Stach, Y. W. Park, J.-C. Charlier, M. Drndic, and A. T. C. Johnson, 2014, Nano Lett. **14**, 4238.
Qiu, C., H. Zhou, H. Yang, M. Chen, Y. Guo, and L. Sun, 2011, J. Phys. Chem. C **115**, 10019.
Qiu, C. G., Z. Y. Zhang, D. L. Zhong, J. Si, Y. J. Yang, and L. M. Peng, 2015, ACS Nano **9**, 969.
Qu, L., Y. Liu, J.-B. Baek, and L. Dai, 2010, ACS Nano **4**, 1321.
Rani, P., and V. K. Jindal, 2013, RSC Adv. **3**, 802.
Ranjan, V., G. Puebla-Hellmann, M. Jung, T. Hasler, A. Nunnenkamp, M. Muoth, C. Hierold, A. Wallraff, and C. Schoenenberger, 2015, Nat. Commun. **6**, 7165.
Rao, A., *et al.*, 1997, Science **275**, 187.
Reich, S., J. Maultzsch, C. Thomsen, and P. Ordejón, 2002, Phys. Rev. B **66**, 035412.
Righi, A., S. D. Costa, H. Chacham, C. Fantini, P. Venezuela, C. Magnuson, L. Colombo, W. S. Bacsa, R. S. Ruoff, and M. A. Pimenta, 2011, Phys. Rev. B **84**, 241409.
Rigo, V. A., T. B. Martins, A. J. R. da Silva, A. Fazzio, and R. H. Miwa, 2009, Phys. Rev. B **79**, 075435.
Robertson, A. W., C. S. Allen, Y. A. Wu, K. He, J. Olivier, J. Neethling, A. I. Kirkland, and J. H. Warner, 2012, Nat. Commun. **3**, 1144.
Rodriguez-Nieva, J. F., E. B. Barros, R. Saito, and M. S. Dresselhaus, 2014, Phys. Rev. B **90**, 235410.
Romo-Herrera, J. M., M. Terrones, H. Terrones, S. Dag, and V. Meunier, 2007, Nano Lett. **7**, 570.
Rosenblatt, S., Y. Yaish, J. Park, J. Gore, V. Sazonova, and P. McEuen, 2002, Nano Lett. **2**, 869.
Rueckes, T., K. Kim, E. Joselevich, G. Tseng, C. Cheung, and C. Lieber, 2000, Science **289**, 94.
Saffarzadeh, A., and R. Farghadan, 2011, Appl. Phys. Lett. **98**, 023106.
Saha, K., T. Markussen, K. Thygesen, and B. Nikolić, 2011, Phys. Rev. B **84**, 041412.
Saha, K. K., B. K. Nikolic, V. Meunier, W. Lu, and J. Bernholc, 2010, Phys. Rev. Lett. **105**, 236803.
Saito, R., G. Dresselhaus, and M. S. Dresselhaus, 1998, *Physical Properties of Carbon Nanotubes* (Imperial College Press, London).
Saito, R., M. Fujita, G. Dresselhaus, and M. S. Dresselhaus, 1992, Phys. Rev. B **46**, 1804.
Saito, R., A. Jorio, A. Souza Filho, G. Dresselhaus, M. Dresselhaus, and M. Pimenta, 2001, Phys. Rev. Lett. **88**, 027401.
Sakaguchi, H., Y. Kawagoe, Y. Hirano, T. Iruka, M. Yano, and T. Nakae, 2014, Adv. Mater. **26**, 4134.
Samsonidze, G., E. Barros, R. Saito, J. Jiang, G. Dresselhaus, and M. Dresselhaus, 2007, Phys. Rev. B **75**, 155420.
Samsonidze, G., R. Saito, A. Jorio, A. G. Souza Filho, A. Grüneis, M. Pimenta, G. Dresselhaus, and M. Dresselhaus, 2003, Phys. Rev. Lett. **90**, 027403.
Sanchez-Valencia, J. R., T. Dienel, O. Gröning, I. Shorubalko, A. Mueller, M. Jansen, K. Amsharov, P. Ruffieux, and R. Fasel, 2014, Nature (London) **512**, 61.

Sandner, A., T. Preis, C. Schell, P. Giudici, K. Watanabe, T. Taniguchi, D. Weiss, and J. Eroms, 2015, Nano Lett. **15**, 8402.
Sapmaz, S., P. Jarillo-Herrero, Y. M. Blanter, C. Dekker, and H. S. J. Van Der Zant, 2006, Phys. Rev. Lett. **96**, 026801.
Sarker, B. K., S. Shekhar, and S. I. Khondaker, 2011, ACS Nano **5**, 6297.
Sasaki, K., R. Saito, G. Dresselhaus, M. S. Dresselhaus, H. Farhat, and J. Kong, 2008, Phys. Rev. B **77**, 245441.
Sato, K., R. Saito, C. Cong, T. Yu, and M. S. Dresselhaus, 2012, Phys. Rev. B **86**, 125414.
Savinskii, S. S., and V. A. Petrovskii, 2002, Phys. Solid State **44**, 1802.
Schoelz, J. K., P. Xu, V. Meunier, P. Kumar, M. Neek-Amal, P. M. Thibado, and F. M. Peeters, 2015, Phys. Rev. B **91**, 045413.
Schwierz, F., 2010, Nat. Nanotechnol. **5**, 487.
Sevinçli, H., M. Topsakal, and S. Ciraci, 2008, Phys. Rev. B **78**, 245402.
Shenoy, V. B., C. D. Reddy, A. Ramasubramaniam, and Y. W. Zhang, 2008, Phys. Rev. Lett. **101**, 245501.
Shim, M., A. Javey, N. Kam, and H. Dai, 2001, J. Am. Chem. Soc. **123**, 11512.
Shiotari, A., T. Kumagai, and M. Wolf, 2014, J. Phys. Chem. C **118**, 11806.
Siebentritt, S., R. Pues, K.-H. Rieder, and A. M. Shikin, 1997, Phys. Rev. B **55**, 7927.
Simonis, P., C. Goffaux, P. Thiry, L. Biro, P. Lambin, and V. Meunier, 2002, Surf. Sci. **511**, 319.
Smith, B., and D. Luzzi, 2001, J. Appl. Phys. **90**, 3509.
Smith, J. T., A. D. Franklin, D. B. Farmer, and C. D. Dimitrakopoulos, 2013, ACS Nano **7**, 3661.
Sofo, J. O., A. S. Chaudhari, and G. D. Barber, 2007, Phys. Rev. B **75**, 153401.
Solis-Fernandez, P., M. A. Bissett, M. Tsuji, and H. Ago, 2015, Nanoscale **7**, 3572.
Son, Y.-W., M. L. Cohen, and S. G. Louie, 2006a, Phys. Rev. Lett. **97**, 216803.
Son, Y.-W., M. L. Cohen, and S. G. Louie, 2006b, Nature (London) **444**, 347.
Song, B., G. F. Schneider, Q. Xu, G. Pandraud, C. Dekker, and H. Zandbergen, 2011, Nano Lett. **11**, 2247.
Soriano, D., F. Munoz-Rojas, J. Fernandez-Rossier, and J. J. Palacios, 2010, Phys. Rev. B **81**, 165409.
Souza Filho, A., N. Kobayashi, J. Jiang, A. Grüneis, R. Saito, S. Cronin, J. Mendes Filho, G. Samsonidze, G. Dresselhaus, and M. Dresselhaus, 2005, Phys. Rev. Lett. **95**, 217403.
Stampfer, C., J. Guettinger, S. Hellmueller, F. Molitor, K. Ensslin, and T. Ihn, 2009, Phys. Rev. Lett. **102**, 056403.
Stampfer, C., J. Guettinger, F. Molitor, D. Graf, T. Ihn, and K. Ensslin, 2008, Appl. Phys. Lett. **92**, 012102.
Steiner, M., *et al.*, 2012, Appl. Phys. Lett. **101**, 053123.
Stone, A., and D. Wales, 1986, Chem. Phys. Lett. **128**, 501.
Subrahmanyam, K. S., L. S. Panchakarla, A. Govindaraj, and C. N. R. Rao, 2009, J. Phys. Chem. C **113**, 4257.
Sumpter, B. G., J. Huang, V. Meunier, J. M. Romo-Herrera, E. Cruz-Silva, H. Terrones, and M. Terrones, 2009, Int. J. Quantum Chem. **109**, 97.
Sun, D. M., M. Y. Timmermans, Y. Tian, A. G. Nasibulin, E. I. Kauppinen, S. Kishimoto, T. Mizutani, and Y. Ohno, 2011, Nat. Nanotechnol. **6**, 156.
Sun, G., J. Krti, M. Kertesz, and R. H. Baughman, 2003, J. Phys. Chem. B **107**, 6924.
Suzuura, H., and T. Ando, 2002, Phys. Rev. B **65**, 235412.
Tan, P. H., *et al.*, 2012, Nat. Mater. **11**, 294.
Tans, S., and C. Dekker, 2000, Nature (London) **404**, 834.
Tans, S., M. Devoret, H. Dai, A. Thess, R. Smalley, L. Geerligs, and C. Dekker, 1997, Nature (London) **386**, 474.
Tans, S., A. Verschueren, and C. Dekker, 1998, Nature (London) **393**, 49.
Tao, C., *et al.*, 2011, Nat. Phys. **7**, 616.
Tapaszto, L., G. Dobrik, P. Lambin, and L. P. Biro, 2008, Nat. Nanotechnol. **3**, 397.
Terrones, H., and A. Mackay, 1992, Carbon **30**, 1251.
Terrones, H., and M. Terrones, 2003, New J. Phys. **5**, 126.
Terrones, M., F. Banhart, N. Grobert, J. Charlier, H. Terrones, and P. Ajayan, 2002, Phys. Rev. Lett. **89**, 075505.
Terrones, M., H. Terrones, F. Banhart, J. Charlier, and P. Ajayan, 2000, Science **288**, 1226.
Terrones, M., *et al.*, 2002, Appl. Phys. A **74**, 355.
Thomsen, C., and S. Reich, 2000, Phys. Rev. Lett. **85**, 5214.
Thomsen, C., and S. Reich, 2007, *Light Scattering in Solids IX: Novel Materials and Techniques*, edited by M. Cardona and R. Merlin, Topics in Applied Physics (Springer-Verlag, Berlin), Vol. 108, pp. 115–235.
Tombros, N., C. Jozsa, M. Popinciuc, H. T. Jonkman, and B. J. van Wees, 2007, Nature (London) **448**, 571.
Topsakal, M., H. Sevincli, and S. Ciraci, 2008, Appl. Phys. Lett. **92**, 173118.
Tsen, A. W., L. Brown, M. P. Levendorf, F. Ghahari, P. Y. Huang, R. W. Havener, C. S. Ruiz-Vargas, D. A. Muller, P. Kim, and J. Park, 2012, Science **336**, 1143.
Tulevski, G. S., A. D. Franklin, D. Frank, J. M. Lobez, Q. Cao, H. Park, A. Afzali, S. J. Han, J. B. Hannon, and W. Haensch, 2014, ACS Nano **8**, 8730.
Vandescuren, M., P. Hermet, V. Meunier, L. Henrard, and P. Lambin, 2008, Phys. Rev. B **78**, 195401.
Varghese, S. H., R. Nair, B. G. Nair, T. Hanajiri, T. Maekawa, Y. Yoshida, and D. S. Kumar, 2010, Curr. Nanosci. **6**, 331.
Vazquez de Parga, A. L., F. Calleja, B. Borca, M. C. G. Passeggi, Jr., J. J. Hinarejos, F. Guinea, and R. Miranda, 2008, Phys. Rev. Lett. **100**, 056807.
Venezuela, P., M. Lazzeri, and F. Mauri, 2011, Phys. Rev. B **84**, 035433.
Verissimo-Alves, M., B. Koiller, H. Chacham, and R. B. Capaz, 2003, Phys. Rev. B **67**, 161401.
Vicarelli, L., S. J. Heerema, C. Dekker, and H. W. Zandbergen, 2015, ACS Nano **9**, 3428.
Vieira, B. G., E. B. Barros, D. G. Vercosa, G. Samsonidze, A. G. Souza Filho, and M. S. Dresselhaus, 2014, Phys. Rev. Applied **2**, 014006.
Vo, T. H., M. Shekhirev, D. A. Kunkel, M. D. Morton, E. Berglund, L. Kong, P. M. Wilson, P. A. Dowben, A. Enders, and A. Sinitskii, 2014a, Nat. Commun. **5**, 3189.
Vo, T. H., M. Shekhirev, D. A. Kunkel, F. Orange, M. J.-F. Guinel, A. Enders, and A. Sinitskii, 2014b, Chem. Commun. (Cambridge) **50**, 4172.
Vogel, F. L., and A. Herold, 1977, Mater. Sci. Eng. **31**, 261.
Wakabayashi, K., M. Fujita, H. Ajiki, and M. Sigrist, 1999, Phys. Rev. B **59**, 8271.
Wallace, P. R., 1947, Phys. Rev. **71**, 622.
Wang, C., J. C. Chien, K. Takei, T. Takahashi, J. Nah, A. M. Niknejad, and A. Javey, 2012, Nano Lett. **12**, 1527.
Wang, H., *et al.*, 2014, Proc. Natl. Acad. Sci. U.S.A. **111**, 4776.
Wang, L., Y. Gao, B. Wen, Z. Han, T. Taniguchi, K. Watanabe, M. Koshino, J. Hone, and C. R. Dean, 2015, Science **350**, 1231.

Wang, M., J. Wang, Q. Chen, and L. Peng, 2005, Adv. Funct. Mater. **15**, 1825.
Wang, X., X. Li, L. Zhang, Y. Yoon, P. K. Weber, H. Wang, J. Guo, and H. Dai, 2009, Science **324**, 768.
Wang, X. R., Y. J. Ouyang, L. Y. Jiao, H. L. Wang, L. M. Xie, J. Wu, J. Guo, and H. J. Dai, 2011, Nat. Nanotechnol. **6**, 563.
Wang, Y., *et al.*, 2013, Appl. Phys. Lett. **103**, 123101.
Wang, Z. F., S. Jin, and F. Liu, 2013, Phys. Rev. Lett. **111**, 096803.
Wang, Z. F., Q. W. Shi, Q. Li, X. Wang, J. G. Hou, H. Zheng, Y. Yao, and J. Chen, 2007, Appl. Phys. Lett. **91**, 053109.
Warner, J. H., M. H. Ruemmeli, A. Bachmatiuk, and B. Buechner, 2010, Nanotechnology **21**, 325702.
Warner, J. H., M. H. Ruemmeli, L. Ge, T. Gemming, B. Montanari, N. M. Harrison, B. Buechner, and G. A. D. Briggs, 2009, Nat. Nanotechnol. **4**, 500.
Warner, J. H., M. H. Ruemmeli, T. Gemming, B. Buechner, and G. A. D. Briggs, 2009, Nano Lett. **9**, 102.
Warner, J. H., F. Schaeffel, M. H. Ruemmeli, and B. Buechner, 2009, Chem. Mater. **21**, 2418.
Wassmann, T., A. P. Seitsonen, A. M. Saitta, M. Lazzeri, and F. Mauri, 2008, Phys. Rev. Lett. **101**, 096402.
Werner, J. G., T. N. Hoheisel, and U. Wiesner, 2014, ACS Nano **8**, 731.
White, C., J. Li, D. Gunlycke, and J. Mintmire, 2007, Nano Lett. **7**, 825.
White, C. T., D. H. Robertson, and J. W. Mintmire, 1993, Phys. Rev. B **47**, 5485.
White, C. T., and T. N. Todorov, 1998, Nature (London) **393**, 240.
Wirtz, L., and A. Rubio, 2004, Solid State Commun. **131**, 141.
Woodside, M., and P. McEuen, 2002, Science **296**, 1098.
Xia, F., V. Perebeinos, Y.-m. Lin, Y. Wu, and P. Avouris, 2011, Nat. Nanotechnol. **6**, 179.
Xie, L., X. Ling, Y. Fang, J. Zhang, and Z. Liu, 2009, J. Am. Chem. Soc. **131**, 9890.
Xie, L., H. Wang, C. Jin, X. Wang, L. Jiao, K. Suenaga, and H. Dai, 2011, J. Am. Chem. Soc. **133**, 10394.
Xu, H., Y. Chen, W. Xu, H. Zhang, J. Kong, M. S. Dresselhaus, and J. Zhang, 2011, Small **7**, 2945.
Xu, H., L. Xie, H. Zhang, and J. Zhang, 2011, ACS Nano **5**, 5338.
Yaish, Y., J.-Y. Park, S. Rosenblatt, V. Sazonova, P. Brink, and M. McEuen, 2004, Phys. Rev. Lett. **92**, 046401.
Yamada, M., Y. Yamakita, and K. Ohno, 2008, Phys. Rev. B **77**, 054302.
Yan, J.-A., W. Ruan, and M. Chou, 2008, Phys. Rev. B **77**, 125401.
Yan, Z., *et al.*, 2014, ACS Nano **8**, 5061.
Yanagisawa, H., T. Tanaka, Y. Ishida, M. Matsue, E. Rokuta, S. Otani, and C. Oshima, 2005, Surf. Interface Anal. **37**, 133.
Yang, L., and J. Han, 2000, Phys. Rev. Lett. **85**, 154.
Yang, S., and M. Kertesz, 2008, J. Phys. Chem. A **112**, 146.
Yang, X., F. Qiao, X. Zhu, P. Zhang, D. Chen, and A. C. To, 2013, J. Phys. Chem. Solids **74**, 436.
Yang, Y., G. Fedorov, S. E. Shafranjuk, T. M. Klapwijk, B. K. Cooper, R. M. Lewis, C. J. Lobb, and P. Barbara, 2015, Nano Lett. **15**, 7859.
Yankowitz, M., J. Xue, D. Cormode, J. D. Sanchez-Yamagishi, K. Watanabe, T. Taniguchi, P. Jarillo-Herrero, P. Jacquod, and B. J. LeRoy, 2012, Nat. Phys. **8**, 382.
Yano, T., T. Ichimura, S. Kuwahara, F. H'Dhili, K. Uetsuki, Y. Okuno, P. Verma, and S. Kawata, 2013, Nat. Commun. **4**, 2592.
Yao, Z., C. Kane, and C. Dekker, 2000, Phys. Rev. Lett. **84**, 2941.
Yao, Z., H. Postma, L. Balents, and C. Dekker, 1999, Nature (London) **402**, 273.
Yazyev, O. V., 2008, Nano Lett. **8**, 1011.
Yazyev, O. V., 2010, Rep. Prog. Phys. **73**, 056501.
Yazyev, O. V., and Y. P. Chen, 2014, Nat. Nanotechnol. **9**, 755.
Yazyev, O. V., and S. G. Louie, 2010, Nat. Mater. **9**, 806.
Ye, L. H., B. G. Liu, D. S. Wang, and R. Han, 2004, Phys. Rev. B **69**, 235409.
Yu, J., R. K. Kalia, and P. Vashishta, 1995, Europhys. Lett. **32**, 43.
Yu, S., W. Zheng, C. Wang, and Q. Jiang, 2010, ACS Nano **4**, 7619.
Yu, W. J., L. Liao, S. H. Chae, Y. H. Lee, and X. F. Duan, 2011, Nano Lett. **11**, 4759.
Zeng, C. F., E. B. Song, M. S. Wang, S. Lee, C. M. Torres, J. S. Tang, B. H. Weiller, and K. L. Wang, 2013, Nano Lett. **13**, 2370.
Zhang, H., X. Yu, and P. V. Braun, 2011, Nat. Nanotechnol. **6**, 277.
Zhang, M., K. R. Atkinson, and R. H. Baughman, 2004, Science **306**, 1358.
Zhang, Y., Y. Tan, H. Stormer, and P. Kim, 2005, Nature (London) **438**, 201.
Zhao, S., Y. Miyata, H. Shinohara, and R. Kitaura, 2014, Carbon **71**, 159.
Zhao, X., Y. Ando, Y. Liu, M. Jinno, and T. Suzuki, 2003, Phys. Rev. Lett. **90**, 187401.
Zhao, Y., Y. Lin, and B. Yakobson, 2003, Phys. Rev. B **68**, 233403.
Zhao, Y., R. Smalley, and B. Yakobson, 2002, Phys. Rev. B **66**, 195409.
Zhao, Y., B. Yakobson, and R. Smalley, 2002, Phys. Rev. Lett. **88**, 185501.
Zheng, X. H., I. Rungger, Z. Zeng, and S. Sanvito, 2009, Phys. Rev. B **80**, 235426.
Zhou, X., J. Park, S. Huang, J. Liu, and P. McEuen, 2005, Phys. Rev. Lett. **95**, 146805.
Zhu, J., J. Kang, J. Kang, D. Jariwala, J. D. Wood, J.-W. T. Seo, K.-S. Chen, T. J. Marks, and M. C. Hersam, 2015, Nano Lett. **15**, 7029.